

# Optical Modeling of Black Chrome Solar Selective Coatings

*When printing a copy of any digitized SAND  
Report, you are required to update the  
markings to current standards.*

James N. Sweet, Richard B. Pettit

Prepared by  
Sandia National Laboratories  
Albuquerque, New Mexico 87185 and Livermore, California 94550  
for the United States Department of Energy  
under Contract DE-AC04-76DP00789



Issued by Sandia National Laboratories, operated for the United States Department of Energy by Sandia Corporation.

**NOTICE:** This report was prepared as an account of work sponsored by an agency of the United States Government. Neither the United States Government nor any agency thereof, nor any of their employees, nor any of their contractors, subcontractors, or their employees, makes any warranty, express or implied, or assumes any legal liability or responsibility for the accuracy, completeness, or usefulness of any information, apparatus, product, or process disclosed, or represents that its use would not infringe privately owned rights. Reference herein to any specific commercial product, process, or service by trade name, trademark, manufacturer, or otherwise, does not necessarily constitute or imply its endorsement, recommendation, or favoring by the United States Government, any agency thereof or any of their contractors or subcontractors. The views and opinions expressed herein do not necessarily state or reflect those of the United States Government, any agency thereof or any of their contractors or subcontractors.

Printed in the United States of America  
Available from  
National Technical Information Service  
U.S. Department of Commerce  
5285 Port Royal Road  
Springfield, VA 22161

NTIS price codes  
Printed copy: A06  
Microfiche copy: A01

## OPTICAL MODELING OF BLACK CHROME SOLAR SELECTIVE COATINGS

J. N. Sweet and R. B. Pettit  
Thermophysical Properties Division

### Abstract

The spectral reflectance of an electroplated black chrome solar selective coating depends on both plating process variables and on the subsequent time-temperature history experienced by the coating. The details of the plating process determine the nature of the coating microstructure and morphology while subsequent thermal aging in air results in oxidation of metallic chrome in the coating. Various investigations of coating microstructure are reviewed and the results of these studies are used to develop a tentative picture of the microstructure of black chrome films plated from the Harshaw Chromonyx bath. In this model, the black chrome film is composed of roughly spherical particles  $\sim 0.2 \mu\text{m}$  in diameter which may tend to cluster together. These particles in turn are composed of small ( $\leq 0.02 \mu\text{m}$ ) crystallites of metallic chrome and various oxides of chrome. The film void volume fraction appears to be  $\geq 0.6$  and results from both voids between the particles and voids within the particles. Even though the exact distribution of metallic chromium, void, and oxides within the particles has not been determined, the microstructural picture has been idealized to facilitate calculations of the spectral reflectance for films deposited onto nickel substrates and for freestanding or stripped films. In the idealized model, the metallic chromium is assumed to be in the form of spherical crystallites with concentric shells of  $\text{Cr}_2\text{O}_3$  and the crystallite volume fraction is assumed to increase with depth into the film. Various experimental data are utilized to define film thickness, average volume fraction of  $\text{Cr} + \text{Cr}_2\text{O}_3$ , and volume ratio of  $\text{Cr}$  to  $\text{Cr} + \text{Cr}_2\text{O}_3$ . Both the Maxwell-Garnett (MG) and the Bruggeman effective

medium theories for the dielectric constant of a composite media are reviewed. The extension of the MG theory to high inclusion volume fractions is discussed and it is demonstrated that the dielectric constant for a cubic array of cubic inclusions is very similar to the MG dielectric constant at all volume fractions. Various forms of the MG theory and the Bruggeman theory are then utilized in reflectance calculations for both regular and stripped films. The results indicate that the MG formalism provides the best overall description of the optical response of black chrome films. The predicted dependence of solar averaged absorptance on coating oxide content is similar to that observed experimentally. Both model and experiment show that the solar absorptance initially decreases slowly as the amount of  $\text{Cr}_2\text{O}_3$  increases, however a rapid decrease occurs when the  $\text{Cr}_2\text{O}_3$  content passes  $\approx 70$  vol %. This work has led to the conclusion that coating degradation is caused primarily by oxidation of the metallic chrome crystallites at elevated temperatures.

Table of Contents

	<u>Page</u>
I. Introduction . . . . .	3
II. History of Black Cr Development for Solar Applications . . . . .	5
III. Summary of Experimental Results	
A. Introduction . . . . .	9
B. Film Composition . . . . .	9
C. Film Structure . . . . .	11
D. Reflectance Properties . . . . .	13
E. Thermal Aging Characteristics . . . . .	14
IV. Theory of Composite Medium Optical Response	
A. Maxwell-Garnett Effective Medium Theory . . . . .	17
B. Extension of the Maxwell-Garnett Theory to High Fill Factors . . . . .	26
C. Optical Properties . . . . .	37
D. Comparison of Model Dielectric Constant Dependence on Volume Fraction . . . . .	39
E. Effect of Particle Eccentricity . . . . .	44
F. Reflectance Calculations . . . . .	47
V. Comparison - Theory vs Experiment	
A. Experimental Reflectance Measurements . . . . .	51
B. Coating Structural Model . . . . .	52
C. Calculated Results . . . . .	62
1. Verification of Computer Code . . . . .	62
2. Reflectance of Black Cr Films on Ni-MG Model . . . . .	63
3. Effect of Variation of Model Parameters . . . . .	66
4. Effect of Using Alternate Dielectric Functions . . . . .	74
D. Results of Experiments and Calculations with Stripped Films . . . . .	79
VI. Discussion and Conclusions . . . . .	87
Appendix A - Dielectric Constant of an MG Medium with Randomly Oriented Ellipsoidal Inclusions . . . . .	93
Appendix B - Cube Polarization Calculations . . . . .	99
Acknowledgements . . . . .	110
References . . . . .	111



## I. Introduction

Black chrome (Cr) electroplated films are now widely used for making solar selective coatings on the receiver tubes in concentrating systems. At temperatures  $T \lesssim 250^\circ\text{C}$ , little difficulty has been experienced with this coating over periods of several years. For operating temperatures in excess of  $300^\circ\text{C}$ , moderate to severe coating degradation has been observed. This degradation is accompanied by a decrease in the solar absorptance  $\alpha_s$  and, in severe cases, the coating becomes brownish or nonblack to the eye. As a result of the observed coating degradation, additional process development work has been conducted in an attempt to determine the values of important plating variables which optimize coating survivability.<sup>1,2</sup> In addition, efforts have been directed toward determination of the coating microstructure and development of an optical model which can explain coating degradation in terms of chemical or structural changes in the black Cr. The purpose of this paper is to describe these studies and to show how the resultant microstructural model can explain the changes in  $\alpha_s$  and the coating emittance  $\epsilon$  in terms of oxidation of Cr crystallites in the coating. A preliminary version of some of the major results of this study has been previously presented.<sup>3</sup>

Selective solar absorbers have long been known to be desirable for making concentrating systems work efficiently. This is particularly true for systems which work at moderate concentration ratios,  $C \lesssim 50$ , and relatively high temperatures,  $T \gtrsim 300^\circ\text{C}$ . The general improvements in efficiency when operating in this concentration ratio and temperature range have been discussed by Seraphin.<sup>4</sup> In a specific test of a parabolic trough concentrator operating at  $316^\circ\text{C}$ , Treadwell reports an improvement in overall efficiency by a factor of 2 or more when a receiver tube coated with Pyromark paint ( $\alpha_s = 0.98$ ,  $\epsilon \approx 0.90$ ) was replaced with a black Cr plated tube ( $\alpha_s \approx 0.97$ ,  $\epsilon = 0.28$ ).<sup>5</sup> The actual improvement in efficiency when a selective coating replaces a nonselective coating on a receiver

depends on the details of the receiver construction but it appears that the use of selective absorbers in line focus systems will be indispensable.<sup>4</sup> Since solar systems are designed for long life operation (~10-20 yrs), the stability of the selective coating must be good at normal operating temperatures. A stable coating is defined as one in which  $\alpha_s$  and  $\epsilon$  change by at most a few percent over the operating life of the concentrator. Loss of focus accidents can also result in very high transient receiver temperatures before the concentrator can be driven off focus. As a result of these considerations there is great interest in developing a high performance selective coating with good thermal stability properties. Black Cr exhibits good optical performance but its stability has frequently been inadequate for some applications. However, no replacement coating is presently available for production applications, although some have been tested in the laboratory.<sup>4,6,7</sup> Until a new and more stable coating is actually available for production purposes, there will be a need to continue developing and improving the black Cr process in order to increase thermal stability. In addition, there is some hope that protective coatings can be developed which might help to reduce black Cr degradation at high temperatures.<sup>8</sup>

In this report we discuss the nature of the present understanding of plated black Cr coatings. Sec. II contains a review of the history of black Cr studies and development programs in the U. S. and France. In Sec. III experimental studies of coating microstructure are reviewed and the results of recent experiments in this area are discussed. The development of a theoretical optical model of a black Cr coating is described in Sec. IV and the theoretical results are compared with experiment in Sec. V. The results of this analysis are discussed in Sec. VI where it is shown that Cr oxidation appears to be the prime cause of coating degradation. The conclusions of this study are then set forth with some recommendations for future activity in the black Cr area.

## II. History of Black Cr Development for Solar Applications

The first mention of black Cr as a prospective solar selective absorber was made by Tabor in 1959.<sup>9</sup> It was considered as a possible replacement for Ni black in space applications where high stability was required. Tabor reports that he was unable to get reliable optical data from his electrodeposited black Cr coatings because the surface was rough. It was not until 1974 that any detailed study of the optical properties of black Cr coatings was made. At that time, McDonald<sup>10</sup> reported results on the spectral reflectance of a coating plated from a proprietary bath developed by the Harshaw Co.<sup>11</sup> McDonald measured a solar absorptance of 0.87 and a 120°C emittance of 0.09 for a coating deposited on a bright nickel plated steel substrate. Approximately a year later Pettit and Sowell<sup>12</sup> reported more extensive results on black Cr films plated from the Harshaw bath. They found that, on a rough Nusat Ni substrate, coatings with a solar averaged absorptance  $\alpha_s \approx 0.95$  and 300°C emittance  $\epsilon(300^\circ\text{C}) \lesssim 0.25$  could be formed. Limited thermal stability tests were made but it was reported that heating for 70 h in air at 400 C reduced  $\alpha_s$  by  $\approx 10\%$ . More extensive thermal aging studies were conducted by Masterson and Seraphin<sup>13</sup> on black Cr coatings plated at Sandia and the Honeywell Corp. They observed the now familiar result that the absorptance "edge" in the reflectance vs wavelength characteristic shifted to shorter wavelengths after heating coatings at 500°C for  $\sim 2$  h. This shift results in a decreased solar absorptance and also a decrease in emittance. After prolonged heating at temperatures of 550 and 600°C the absorptance edge moved back out to longer wavelengths, possibly indicating that a change in the degradation mechanism had occurred.

In view of the fact that line focus parabolic concentrators were expected to operate at temperatures  $T \lesssim 330^\circ\text{C}$  with occasional excursions to much higher temperatures under loss of flow conditions,<sup>14</sup> additional studies of black Cr thermal

stability were undertaken. Initial results of these studies indicated that coating stability appeared to be variable, with some coatings exhibiting an unchanged  $\alpha_g$  after 25-50 h at 350 C while others showed a decrease of 6-10% in  $\alpha_g$  after the same exposure.<sup>15</sup> The coatings were examined using Auger sputter profiling techniques, but no significant differences were observed between stable and unstable coatings at that time. Both types of coatings exhibited evidence of considerable oxidation after exposure at 300 or 350°C.

Continuing studies on the effect of plating variables on coating stability indicated that, for the Harshaw Chromonyx bath, the trivalent Cr concentration appeared to be the major factor in determining thermal stability.<sup>16</sup> By reducing the Cr<sup>3+</sup> concentration from its standard value of 16 g/l to 8 g/l, the coating stability appeared to be greatly improved. For the stable coatings  $\alpha_g$  was reported to be unchanged after aging at 350°C for over 1800 h. In this investigation, the unstable coatings exhibited significantly greater oxide formation than the stable coatings after thermal aging. The effect of plating variable variation on the optical properties and stability of plated black Cr has been the subject of several recent studies.<sup>2,17,18</sup>

There have been several different variations of the black Cr plating process discussed in the literature. The current procedure for plating parabolic trough receiver tubes using the Harshaw Chromonyx bath has been described in detail by Pettit and Sowell.<sup>1</sup> An alternate bath, designated as a tetrachromate bath, has been developed by Sivaswamy, Gowri, and Stenui<sup>19</sup> and coatings plated from this bath have been evaluated by Cathro.<sup>20</sup> These coatings exhibited spectral reflectance and emittance characteristics close to those reported for the Harshaw coatings.<sup>12</sup> Cathro's coatings were stable (showed no change in absorptance or emittance) after a month of vacuum aging at 300°C. No higher temperature testing was reported. Driver, Jones, Riddiford and Simpson have

reported some data on optical properties of black Cr films plated on Cu substrates.<sup>21</sup> They used an unspecified plating process, designated as the "Chrome-Black" process, and reported optical properties which again were qualitatively similar to those found for films plated from the Harshaw bath. Spitz, Van Danh, and Aubert have reported results on films plated from two baths which they designated A and B.<sup>22</sup> Bath A was the tetrachromate bath recommended by Sivaswamy, et al.<sup>19</sup> which must be cooled during plating while bath B was another formulation which could be plated at ambient temperatures. The dependence of  $\alpha_s$  and  $\epsilon$  on annealing time for the coatings produced by Spitz, et al. after air annealing at 250, 300 and 350°C was very similar to that reported by Pettit for coatings plated from a Harshaw bath.<sup>15</sup> From these results, it appears that all plated black Cr coatings behave in a qualitatively similar fashion, at least from an optical viewpoint.

In spite of the similarity in optical properties, the microstructure of these coatings appears to be highly dependent on the details of the plating process and the amount of thermal aging experienced. Since coating microstructure will be discussed in detail in the next section, only the major results and differences between various coatings will be described here. Coatings plated using the Harshaw process are composed of agglomerated particles, roughly spherical in shape, with a mean diameter dependent on the plating process, typically in the range  $\sim 0.05$ - $0.2 \mu\text{m}$ . These agglomerated particles appear to be composed of a mixture of fine metallic Cr crystallites and oxides of Cr. The coatings appear to be highly porous, as determined from film thickness and areal density measurements. It is estimated that the film void volume fraction is  $\sim 0.6$ . Coating thicknesses are typically in the range  $0.1$ - $0.5 \mu\text{m}$ . In contrast to these results, films plated using bath B of Ref. 22 are composed of needle like agglomerates oriented predominately normal to the substrate surface.<sup>25</sup> The needles are reported to

be 0.15-0.35  $\mu\text{m}$  long and  $\sim$ 0.05-0.08  $\mu\text{m}$  in diameter. After annealing at 350°C for 24 hr, the needles became more spherical in shape. In the case of Harshaw bath plated films, the spherical particles retain their shape and size after aging.<sup>23</sup> It appears that the Harshaw bath and a tetrachromate type bath produce black Cr films with similar optical properties but very different microstructural characteristics. The structure of coatings produced from other baths has not been discussed in the literature.

Since the black Cr film structure is highly dependent on the plating process, it is also reasonable to conclude that the thermal aging characteristics of a coating will be very dependent on the type of plating process utilized. In addition, for a given process, the aging characteristics can be expected to depend on the details of that process. An example of this is the previously mentioned identification of the dependence of thermal aging on the bath  $\text{Cr}^{3+}$  concentration for the Harshaw process. Generally, it has been found that thermal aging causes a conversion of the metallic Cr crystallites in the film to oxides of Cr, principally  $\text{Cr}_2\text{O}_3$ . The kinetics of this oxidation process depend on the coating structure, as will be discussed in the following section. This oxidation may be preceded or accompanied by other changes in the film, such as water evolution or possibly a shift in coating thickness.<sup>26</sup>

### III. Summary of Experimental Results

#### A. Introduction

In this section, experimental results regarding the composition and structure of the black chrome coating are summarized. The results represent a compilation of published data obtained from a variety of investigators. Also included is a description of the optical properties of the coating as a function of several plating variables. Finally changes in the coating after thermally heating in both vacuum and air are discussed.

As previously mentioned, there are a variety of electroplating chromium baths that can produce a solar selective deposit.<sup>1,19,21,22</sup> However most of the published research deals with the composition and structure of coatings obtained from the Harshaw Chromonyx bath.<sup>11</sup> In addition, this coating is widely used in the U.S. solar industry for both flat plate and concentrating solar collectors. Therefore the properties of this coating will be emphasized in this section. However, significant differences with other black chrome coatings will also be pointed out.

#### B. Film Composition

The majority of investigators have shown that the black chrome coatings consists primarily of metallic chromium together with chromium oxide in the form  $\text{Cr}_2\text{O}_3$ .<sup>23,24,26-29</sup> The identification of chromium atoms and oxygen atoms has been well established from Auger electron spectroscopy studies, while x-ray photoelectron spectroscopy (XPS) has confirmed that the oxygen is present as  $\text{Cr}_2\text{O}_3$ . This same overall composition has been observed for coatings deposited onto polished bulk nickel, electroplated nickel,<sup>23</sup> 302 stainless steel,<sup>28</sup> copper<sup>24</sup> and gold.<sup>26</sup>

Recent experimental results presented by Zajac, et al.<sup>26</sup> have led them to postulate that a significant amount of the oxygen in the coating is present in the form  $\text{Cr}(\text{OH})_3$ . Other investigators have seen the presence of a hydroxide,

but only on the surface of the coating.<sup>28</sup> In addition, infrared absorption bands associated with a hydroxide species have not been observed.<sup>24,29</sup> Thus the presence or role of a hydroxide in this coating needs further investigation.

By ion sputtering through the coating to the substrate, a compositional depth profile can be obtained. Unfortunately the profiling does not represent the film composition at a plane within the coating which is parallel to the substrate. This results because the coating contains a large fraction of voids in addition to having a rough surface texture (these points will be discussed later). For example, in sputtering through a black chrome coating deposited onto a polished nickel substrate,<sup>30</sup> the sputtering time (ion dose) required to pass through the nickel/film interface is approximately equal to 40% of the sputtering time required to reach the substrate. Nevertheless, most investigators find that the oxygen content within the film decreases as the substrate is approached, while the chromium content increases. The surface composition of the coating is entirely  $\text{Cr}_2\text{O}_3$ , which would be expected since upon exposure to the atmosphere, metallic chromium forms a thin  $\text{Cr}_2\text{O}_3$  film approximately 15-20 Å.<sup>31</sup> By assuming that the film is composed of only metallic chromium and  $\text{Cr}_2\text{O}_3$ , integration of the sputter profiles leads to a measure of the relative amount of each constituent. Holloway, et al.<sup>28</sup> determined that the relative volume fraction of  $\text{Cr}_2\text{O}_3$  to ( $\text{Cr} + \text{Cr}_2\text{O}_3$ ) was in the range  $\approx 0.30-0.44$ , while Zajac, et al.<sup>26</sup> calculated a value of 0.49 for this fraction. Assuming that the coating is composed of spherical particles with a mean diameter of 750 Å (see next section), a 40 vol %  $\text{Cr}_2\text{O}_3$  shell surrounding a central core of metallic chromium would have a thickness of 120 Å. At a 30 vol % value for  $\text{Cr}_2\text{O}_3$ , the shell thickness is reduced to 80 Å, a value which is still considerably higher than the thickness of the natural oxide that forms on bulk metallic chromium. Thus it appears that some of the oxide is probably located within the particles.

Compositional results reported by Spitz, et al.<sup>22</sup> also note that their coating is largely chromium and oxygen. From x-ray diffraction analysis, they also identified CrH<sub>2</sub> but could not identify this phase from electron diffraction on thinned samples. Additional studies<sup>25</sup> of this film also identified CrO<sub>2</sub>, CrO, Cr<sub>3</sub>O<sub>4</sub> and CrO<sub>3</sub>, although the Cr<sub>2</sub>O<sub>3</sub> was the major oxide constituent. The CrO<sub>3</sub> was present only at the outer surface (~200 Å) of the coating.

### C. Film Structure

Structural information on the coating is obtained primarily from scanning electron microscopy (SEM) and transmission electron microscopy (TEM). While samples for SEM studies can be studied directly, all investigators have been unsuccessful in mechanically stripping the black chrome coating from nickel substrates for TEM observations. Therefore two approaches have been utilized: (1) The black chrome coating is electroplated onto a thin nickel foil. After plating, the foil is ion sputtered from the back side until a small hole is produced. The black chrome film exposed around the edges of the hole can be examined in the electron microscope.<sup>22,24</sup> Changes in the coating (such as annealing, ion damage, etc.) caused by the ion sputtering must be considered. (2) Alternatively, the black chrome film is electrodeposited onto a substrate, such as iron or copper, which can be chemically etched away.<sup>23,26</sup> Iron is preferred since the black chrome coating deposited on this substrate does not have high mechanical stresses and is therefore easier to remove in large sections.

SEM observations show the coating to be a particulate deposit with approximately spherical particles with a diameter in the range 500-1000 Å.<sup>23,24,27</sup> Micrographs taken at various stages during the electrodeposition indicate that the particle size remains relatively constant within the film.<sup>23</sup> However, Ignatiev, et al.<sup>27</sup> report that upon sputtering away the first ~300 Å of a 1000 Å thick film, larger elliptical particles are observed. An indication of elliptically

shaped particles has not been reported from TEM studies.<sup>23,24</sup> The SEM studies also indicate that the film has a high volume fraction of voids. The resulting uneven surface texture makes the determination of a film thickness difficult. Lampert<sup>24</sup> reports a film thickness of mechanically polished samples of 0.7-1.0  $\mu\text{m}$  while Zajac, et al.<sup>26</sup> measured a thickness of  $\sim 0.26 \mu\text{m}$  for a similar film. Recent measurements in this laboratory resulted in a film thickness in the range 0.4-0.7  $\mu\text{m}$ .

Electron diffraction analyses of as-deposited film indicate the presence of both metallic chrome and  $\text{Cr}_2\text{O}_3$ . Chrome crystallite diameters are typically in the range 100-1000 $\text{\AA}$ . Lambert<sup>24</sup> has determined a mean chromium crystallite size of  $\sim 150 \text{\AA}$ . Since this size is much less than the average particle diameter observed in SEM studies, each particle must contain many metallic chromium crystallites.

Diffuse diffraction rings, corresponding approximately to crystalline  $\text{Cr}_2\text{O}_3$ , are also observed.<sup>23,24</sup> Thus the chromium oxide in the film exists either as an amorphous material or as extremely small grains ( $\lesssim 10 \text{\AA}$ ). The distribution of the oxide within each particle has not been established. Thus the oxide could be in the form of a thin coating on the chrome crystallites and/or in an amorphous state between the crystallites.

The areal density of the deposit has been measured<sup>3,26</sup> as  $\sim 5.8 \times 10^{-5} \text{ g/cm}^2$ . Using a film thickness of 0.26  $\mu\text{m}$ <sup>26</sup> and a film composition of 70 vol % chromium metal and 30 vol %  $\text{Cr}_2\text{O}_3$ , leads to an average volume packing fraction of only 33%. Because this parameter is important for optical modeling of the film, more data concerning its value should be obtained.

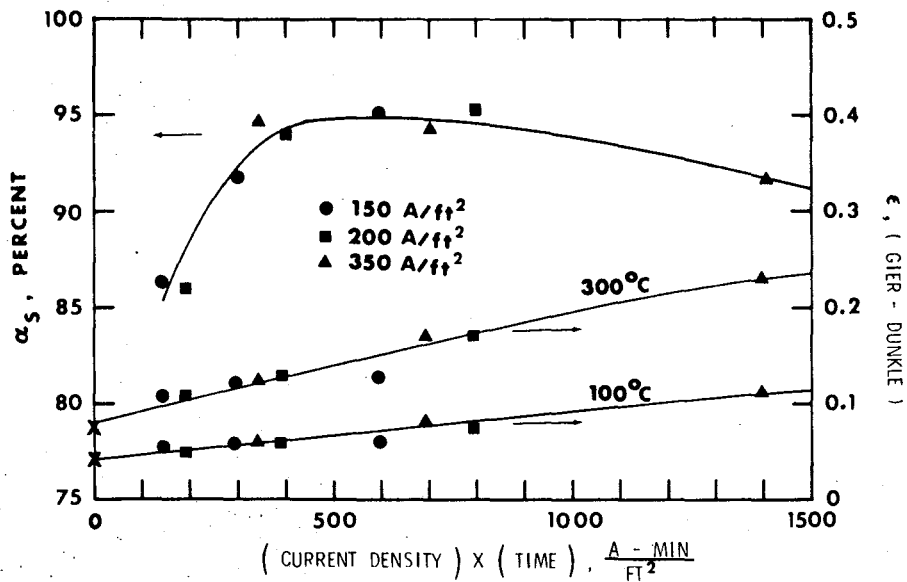
Again, the structure of black chrome films produced by Spitz, et al<sup>22,25</sup> are very different from the Harshaw Chromonyx coating discussed above. Their films consist of a needle-like morphology, with the needles orientated normal

to the substrate. The needles are from 1500-3000 Å long and 500-800 Å in diameter. The film thickness was approximately 0.32 μm. The metallic chromium in the film is also in the form of small crystallites, with diameters from 40-70 Å.

#### D. Reflectance Properties

The near-normal hemispherical reflectance properties were first measured by McDonald in 1975.<sup>10</sup> From the short wavelengths to approximately 1.2 μm, the hemispherical reflectance is relatively constant at a value of ~0.04 reflectance units (1.00 reflectance units = 100% reflectance). Beyond 1.2 μm the reflectance gradually increases until at 5-8 μm it reaches a value of ~0.80 reflectance units. The change from low to high reflectance value in this region will be referred to as the "transition" region or reflectance edge. From 5-8 μm to 25 μm, the reflectance is roughly constant and closely matches the hemispherical reflectance properties of the substrate material.<sup>24</sup> Thus the coating is highly absorbing over the solar spectral region (0.3-1.5 μm), and becomes partially transparent to radiation above ~5 μm. These reflectance characteristics have been obtained for almost all types of black chrome coatings and for a variety of substrates, including nickel, copper, stainless steel, etc.

At a constant plating current density, increasing the plating time causes the transition region to shift to longer wavelengths.<sup>24</sup> The resulting effect on the solar absorptance and the 100°C and 300°C emittance properties are shown in Figure III-1.<sup>32</sup> Note that the solar absorptance rapidly increases to a maximum value of ~0.95 as the plating time increases, while both the 100°C and 300°C emittances increase almost linearly over the range shown. Results obtained for different plating current densities are identical if the same current density/time product is obtained. Thus a coating plated at 300 mA/cm<sup>2</sup> for 2 minutes has the same optical properties as a coating plated at 150 mA/cm<sup>2</sup> for 4 minutes.



III-1 The solar absorptance and emittance properties of black chrome coatings as a function of plating time for three current densities.

The surface roughness of the substrate has only a minor effect on the reflectance properties. Pettit and Sowell<sup>12</sup> have shown that depositing the coating on a rough (or dull) nickel substrate enhances the solar absorptance value slightly (~4-5%) compared to the same coating deposited on a smooth (or bright) nickel substrate. In addition the solar absorptance for the coating deposited on the rough nickel substrate remains higher as a function of incident angle.

#### E. Thermal Aging Characteristics

Considerable effort has been aimed at determining the thermal aging characteristics of deposited coatings, with the goal of determining the degradation mechanism(s) and improving the high temperature resistance of the coating. Sowell and Pettit<sup>2,15</sup> have shown that for the Harshaw coating, the thermal

stability is a strong function of the plating bath composition. Small changes, particularly in the trivalent chromium concentration, can improve the thermal stability dramatically. It is suspected that the stability of coatings obtained from other plating baths may also be sensitive to their composition. Because of this effect, it is not possible to compare degradation rates obtained by different investigators. However, several characteristic changes in the coatings which occur upon heating have been seen by several investigators. These characteristics are summarized below.

Most researchers have found little change in the solar absorptance after heating to temperatures below 250°C in air, although some of the metallic chromium has oxidized.<sup>15,26,33</sup> Above 300°C in air, the solar absorptance can decrease 6-10% after only tens of hours.<sup>15</sup> During this heating, the emittance decreases slightly, but not enough to compensate for the larger decreases in  $\alpha_s$ . Analysis of the coatings shows a continued oxidation of the metallic chromium to Cr<sub>2</sub>O<sub>3</sub>.<sup>15</sup> However the surface morphology remains unchanged during these heat treatments, although the coating thickness may increase by no more than 10-20%. TEM studies show that the metallic chromium crystallite size does not change but that the diffuse diffraction rings from the amorphous or small grain Cr<sub>2</sub>O<sub>3</sub> become crystalline in nature.<sup>23,33</sup> The average Cr<sub>2</sub>O<sub>3</sub> grain size is in the range ~400 Å. Thus the primary change in the coating after heating between 250-400°C appears to be an oxidation of the metallic chromium in the film to crystalline Cr<sub>2</sub>O<sub>3</sub>.

Zajac, et al.<sup>26,30</sup> have extensively studied the compositional changes in coatings deposited on nickel substrates after heating in vacuum (pressure < 5 x 10<sup>-8</sup> torr) for short times to temperatures as high as 550°C. At ~150°C, water and hydrogen are driven from the coating. Heating to 350°C for 12 hours causes very little change in the coating optical properties. After 450°C for 12 hrs the solar absorptance decreases substantially, while the oxygen to chromium

ratio decreases as a function of depth into the film. In addition there is some indication of nickel diffusion into the black chrome coating. Heating to 550°C for 12 hrs results in considerable diffusion of nickel into the coating while the optical response has a metallic like behavior (increased reflectance at short wavelengths). Some agglomeration of the particles was also noted.

#### IV. Theory of Composite Medium Optical Response

##### A. Maxwell-Garnett Effective Medium Theory

From examination of the experimental data discussed in the preceding section it has become apparent that black Cr is a composite medium composed of Cr metal, various Cr oxides, and possibly other compounds such as water. This material is not very dense as the data discussed in Sec. III shows. The void volume fraction of black Cr films is typically  $\sim 0.6$ . In order to calculate the spectral reflectance of a black Cr film, a model for the complex dielectric constant of the film is required. It may be expected that this dielectric constant will depend on the dielectric constants of the constituent materials in the film, the volume fractions of the constituents, and the size and shape of the constituent "particles" in the film. The general theory of dielectric constants and conductivities of inhomogeneous media has been reviewed recently by Landauer<sup>34</sup> and the application of this theory to the spectral selectivity of composite materials has been discussed in detail by Sievers.<sup>6</sup> Since both of these review articles contain extensive references to the primary literature on the subject, we shall cite only those references which are germane to our specific discussions of calculations for black Cr films.

Since there are two major theories used to calculate inhomogeneous media dielectric constants and many parameters which enter into each theory, the number of possible calculations is very large. Indeed, it may well be possible to fit either theory to a given body of data by adroit choice of the parameters. This contention is supported by the existence of a rather large number of papers which have compared calculated to experimental results for black Cr films under a variety of conditions.<sup>25,26,35-40</sup> Despite the existence of this work, there does not appear to be a unifying theme or a general model which explains in a qualitative or semiquantitative way all observed black Cr phenomena. It is the

purpose of this section to review some of the major theories of the dielectric response of composite media and to indicate the influence of microstructure on dielectric properties. The results of this section are used in Sec. V to develop a model from which the coating optical reflectance can be calculated.

One of the major theories used to calculate composite medium dielectric constants is called the Maxwell-Garnett (MG) theory.<sup>41</sup> J. C. M. Garnett set forth this theory for the response of composite media to optical frequency electric fields, but as discussed by Landauer,<sup>34</sup> the MG dielectric function had previously been derived by others for static fields and is equivalent to the well known Clausius-Mossotti relation. The major assumption used in deriving the MG dielectric constant  $\epsilon_{MG}$  is that the composite medium is composed of isolated inclusions of one or more materials in a continuous host or matrix material. By isolated, it is meant that the perturbation fields produced in the matrix by the presence of an inclusion do not extend to other inclusions. In other words, the electric field which polarizes the included particles is the field in the matrix far from any of the particles. A functional form for  $\epsilon_{MG}$  can be calculated for the case in which the inclusions are ellipsoidal particles with a specified distribution of eccentricities and orientations. This is possible because the field is constant in both magnitude and direction inside an ellipsoidal body which is polarized by a uniform electric field.

The other major theory of dielectric functions for composite media is the Bruggeman symmetrical effective medium theory.<sup>42,43</sup> In this theory, the matrix and the imbedded particles are treated on an equal footing; i.e., they are both considered to be in particulate form and more or less symmetrical to each other. The field which polarizes a "particle" in the medium is considered to be the effective or average field which exists in the medium far from the "particle" in question. Another way of stating this is to say that the field in the medium is

composed of an average or effective field plus a field which varies rapidly in space with a variation distance on the order of a typical particle linear dimension. The net polarization produced by this varying field is assumed to be small or negligible as compared to the polarization produced by the average field. Again, in the case for which the particles of inclusion and matrix are ellipsoidal in shape with known distributions of eccentricities and orientations, an exact equation can be derived for the effective dielectric constant  $\epsilon_B$ . However, unlike the Maxwell-Garnett case in which the equation for  $\epsilon_{MG}$  is linear in  $\epsilon_{MG}$ , the equation for  $\epsilon_B$  is a polynomial equation with an order determined by the number of different types of particles in the medium. Hence solution of the equation for  $\epsilon_B$  in cases where particles with many different shapes and orientations are present is a formidable task.

The ideas discussed above may be illustrated more clearly by considering a derivation of the two effective dielectric constants similar to that first proposed by Bragg and Pippard<sup>44</sup> and later by Genzel and Martin.<sup>45</sup> The model system under consideration is shown in Fig. IV-1(a). An incident plane polarized electromagnetic wave with an electric field strength  $E_0 = |\vec{E}_0|$  and a propagation vector of magnitude  $k_0$  is incident normally on a slab of composite material. The dashed path in Fig. IV-1(a) is used to establish the continuity of the x-component of the electric field across the material boundary. Performing a surface integral of the Maxwell "curl E" equation over the surface bounded by the dashed line yields the result,

$$\left| -E_0 \Delta \ell + \int_{\Delta \ell} E_x(x, 0, 0^+) dx \right| = \frac{\omega B_0}{c} \Delta \ell \Delta z \quad (IV-1)$$

In Eq. (IV-1),  $c$  = speed of light,  $\omega$  = angular frequency of the wave,  $E_x(x, 0, 0^+)$  is the  $x$  component of the electric field evaluated just inside the composite medium. Since  $\omega = 2\pi c/\lambda_0$ , where  $\lambda_0$  = free space wavelength, and  $B_0 = E_0$  outside the medium, Eq. (IV-1) reduces to,

$$\left| -E_0 + \frac{1}{\Delta l} \int_{\Delta l} E_x(x, 0, 0^+) dx \right| = 2\pi \frac{\Delta z}{\lambda_0} \quad (\text{IV-2})$$

If the wavelength is sufficiently long such that  $\lambda_0 \gg \Delta z$ , then the right hand side of Eq. (IV-2) is negligible and we find the usual assumed result that the external field  $E_0$  is equal to the average field in the medium, i.e.,

$$E_0 = \frac{1}{\Delta l} \int_{\Delta l} E_x(x, 0, 0^+) dx \quad (\text{IV-3})$$

In effective medium theory, the average field  $\bar{E}$  inside the medium, as given by the right hand side of Eq. (IV-3), is assumed to be related to the average polarization  $\bar{P}$  via the relation,

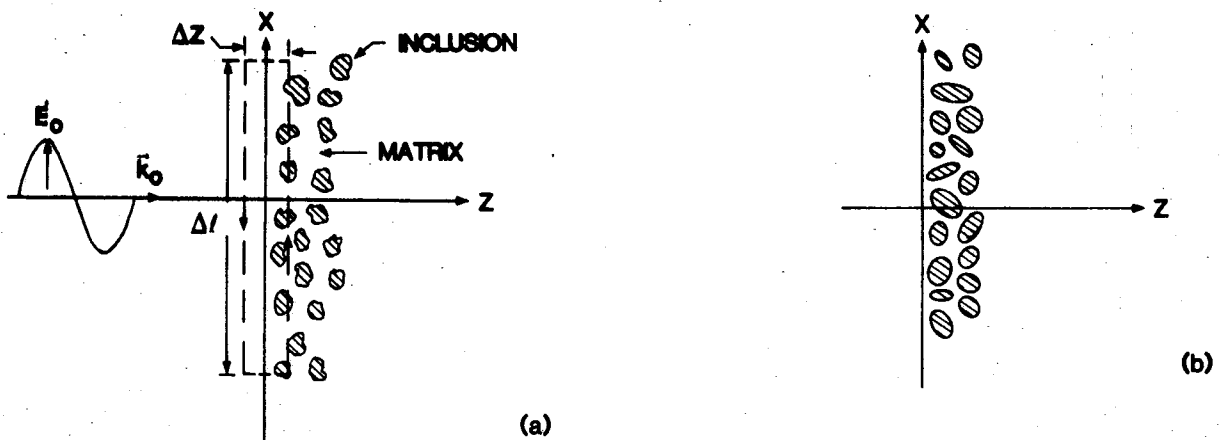
$$4\pi\bar{P} = (\bar{\epsilon} - 1)\bar{E} \quad , \quad (\text{IV-4})$$

where  $\bar{\epsilon}$  is the average or effective dielectric constant of the medium.

Actual composite films such as black Cr frequently have surface roughness variations on a scale  $\gtrsim 0.1 \mu\text{m}$ . Since we are interested in wavelengths down to a minimum,  $\lambda_0 \approx 0.2 \mu\text{m}$ , the condition  $\lambda_0 \gg \Delta z$  is not always satisfied for real systems if  $\Delta z$  is required to be larger than the RMS surface roughness. However, at these short wavelengths it will be seen that the Cr particles in the film are very strongly absorbing, leading to a very small reflectance for  $\lambda_0 \lesssim 1 \mu\text{m}$ . Thus, although the approximations in the theory are somewhat suspect at

short wavelengths, in actual practice this does not appear to be a serious limitation.

To derive the MG effective dielectric constant  $\epsilon_{MG}$ , the actual "model" system shown in Fig. IV-1(a) is replaced by an idealized system as shown in IV-1(b). In the idealized system, the isolated inclusions are replaced by ellipsoidal particles and it is assumed that they are sufficiently isolated that the field in the matrix material is essentially constant at a value  $E_m$ .



- IV-1 (a) An incident electromagnetic wave with field strength  $E_0$  and propagation vector  $\vec{k}_0 = (2\pi/\lambda_0) z$  impinges on a composite medium in the half-space  $z > 0$ . The composite medium is composed of a continuous matrix phase and isolated inclusions. The dashed line indicates the path of integration for deriving Eq. (IV-2).
- (b) An idealization of the composite structure in (a). The irregularly shaped inclusions are replaced by ellipsoidal particles.

If  $i$  is an index which is summed over all orientations and eccentricities of idealized inclusions and  $f_i$  is the volume fraction of inclusions of type  $i$ , then

$$\bar{E}_x = \sum_i f_i E_{in(i)}^x + (1 - f) E_m \quad (IV-5)$$

In Eq. (IV-5),  $f$  is the total volume fraction of inclusions,  $f = \sum_i f_i$  and  $E_{in(i)}^x$  is the  $x$  component of the constant field inside an ellipsoidal inclusion. If the ellipsoidal inclusions have a scalar dielectric constant  $\epsilon_c$  and are aligned with a principal axis along the  $x$  direction in a homogeneous medium with dielectric constant  $\epsilon_m$ , then the internal field strength is given by the relation,<sup>44</sup>

$$E_{in(i)} = \frac{\epsilon_m E_m}{L_i \epsilon_c + (1 - L_i) \epsilon_m} \quad (IV-6)$$

where  $L_i$  = depolarizing factor for a particle of the  $i$ th type. The average polarization,  $\bar{P}$ , may be written as,

$$\begin{aligned} \bar{P} &= \left\{ \sum_i f_i P_i + (1 - f) P_m \right\} \\ &= (1/4\pi) \left[ \sum_i f_i (\epsilon_c - 1) E_{in(i)} + (1 - f) (\epsilon_m - 1) E_m \right] \end{aligned} \quad (IV-7)$$

Equating  $4\pi$  times Eq. (IV-7) to  $(\bar{\epsilon} - 1)\bar{E}$  in Eq. (IV-4), with  $\bar{E} = \sum_i f_i E_{in(i)} + (1 - f)E_m$ , yields the fundamental relation of MG theory (with  $\bar{\epsilon} = \epsilon_{MG}$ ),

$$\begin{aligned} (\epsilon_{MG} - 1) \left[ \sum_i f_i E_{in(i)} + (1 - f) E_m \right] &= \sum_j f_j (\epsilon_c - 1) E_{in(j)} \\ &+ (1 - f) (\epsilon_m - 1) E_m \end{aligned} \quad (IV-8)$$

$E_{in(i)}$  from Eq. (IV-6) is then substituted into Eq. (IV-8) yielding a common factor  $E_m$  which can be cancelled from each term. The resultant equation can be easily solved for  $\epsilon_{MG}$  and the solution can be cast in the form,

$$\epsilon_{MG} = \epsilon_m \left\{ \frac{1 + \sum_i f_i (1 - L_i) \alpha_i}{1 - \sum_i f_i L_i \alpha_i} \right\}, \quad (IV-9)$$

where the polarizability factors,  $\alpha_i$  are defined by

$$\alpha_i = \frac{\epsilon_c - \epsilon_m}{\epsilon_m + L_i(\epsilon_c - \epsilon_m)} \quad (\text{IV-10})$$

In order to compare the result given in Eq. (IV-9) with other forms which have been presented in the literature, we consider some special cases which can be derived from Eq. (IV-9). For a single type of inclusion, with all particles aligned with the same principal axis in the x direction, Eq. (IV-9) becomes

$$\epsilon_{MG} = \epsilon_m \left[ \frac{1 + f(1 - L)\alpha}{1 - fL\alpha} \right] \quad (\text{IV-11})$$

Frequently, the included particles are assumed to be prolate spheroids or ellipsoids of revolution in which two principal axes are equal and the third axis is longer. If a, b, and c are the principal axes for a prolate spheroid,  $a = b$  and  $a < c$ . Then the depolarizing factors are given by,<sup>46</sup>

$$L_c = \frac{1}{(r^2 - 1)} \left\{ \frac{r}{(r^2 - 1)^{1/2}} \ln[r + (r^2 - 1)^{1/2}] - 1 \right\} \quad (\text{IV-12})$$

$$L_a = L_b = (1 - L_c)/2$$

$$r = c/a$$

As  $c/a \rightarrow \infty$  (cigar shaped particles),

$$L_a = L_b \rightarrow 1/2 \quad (\text{IV-13})$$

$$L_c \rightarrow (1/r^2) [\ln(2r) - 1]$$

In some situations, oblate spheroids are postulated. In this case, two principal axes are again equal but the third axis is shorter than the equal axes. For this case the depolarizing factors are given by,

$$L_c = \frac{r^2}{(r^2 - 1)} \left\{ 1 - \left( \frac{1}{r^2 - 1} \right)^{1/2} \sin^{-1} \left[ \frac{(r - 1)^{1/2}}{r} \right] \right\} \quad (\text{IV-14})$$

$$L_a = L_b = (1 - L_c)/2$$

$$\text{As } r \rightarrow \infty \quad L_c \rightarrow 1 \quad (\text{IV-15})$$

$$L_a = L_b \rightarrow \pi/4r$$

For spherical particles,  $L = 1/3$  for all axes. In all cases,  $L_a + L_b + L_c = 1$ .

In a recent analysis of the spectral reflectance of a black Cr type selective absorber, Granqvist and Hunderi<sup>38</sup> used a slight modification of Eq. (IV-11). If this equation is rewritten in the form,

$$\epsilon_{MG} = \epsilon_m \left\{ \frac{1 + (2/3)f\alpha[(3/2)(1 - L)]}{1 - \frac{f\alpha}{3}[3L]} \right\}, \quad (\text{IV-16})$$

the Granqvist and Hunderi (GH) form is obtained by setting the quantities in square brackets equal to unity, with the result that the depolarizing factor appears only in the quantity  $\alpha$  as given by Eq. (IV-10). The difference in the two formulations results from differences in the derivations, as discussed by Cohen, Cody, Coult, and Abeles<sup>47</sup> and by Landauer.<sup>34</sup> Both formulations yield identical results for spherical inclusions with  $L = 1/3$  but differ appreciably in the case of needle shaped particles oriented parallel to the incident electric field ( $L \rightarrow 0$ ) or plate shaped particles with the small axis parallel to the field ( $L \rightarrow 1$ ).

Another case of frequent interest is one in which the inclusions are assumed to be randomly distributed, both in orientation and in eccentricity. A theoretical model of this sort has been outlined by O'Neill and Ignatiev.<sup>48</sup> To derive their result, we first assume that the ellipsoids are distributed with their principal

axes randomly oriented along the x, y and z directions and that the eccentricities ( $r = c/a$ ) are distributed according to a distribution function  $\rho(r)$  such that  $\rho(r)dr =$  the fraction of inclusions with eccentricities between  $r$  and  $(r + dr)$ . Then,  $f_1$  in Eq. (IV-9) is replaced by the expression,

$$f_1 \rightarrow \rho(r)dr \frac{f}{3}, \quad (\text{IV-17})$$

and the summation in Eq. (IV-9) becomes an integration over  $r$  and summation over the principal axes, i.e.,

$$\epsilon_{MG} = \epsilon_m \left\{ \frac{1 + \frac{f}{3} \int_0^{\infty} dr \left\{ \rho(r) \sum_{j=1}^3 [1 - L_j(r)] \alpha_j(r) \right\}}{1 - \frac{f}{3} \int_0^{\infty} dr \left\{ \rho(r) \sum_{j=1}^3 L_j(r) \alpha_j(r) \right\}} \right\} \quad (\text{IV-18})$$

In Eq. (IV-18) the  $j$  index runs over the ellipsoid axes  $a$ ,  $b$  and  $c$  and the  $L_j$  functions are given by Eqs. (IV-12) or Eqs. (IV-14) for prolate or oblate ellipsoids respectively. O'Neill and Ignatiev assume that only prolate ellipsoids are present ( $1 \leq r \leq \infty$ ) and that they are distributed log-normally in  $r$ . They use the mean and standard deviation of the distribution as fitting parameters in addition to other parameters.

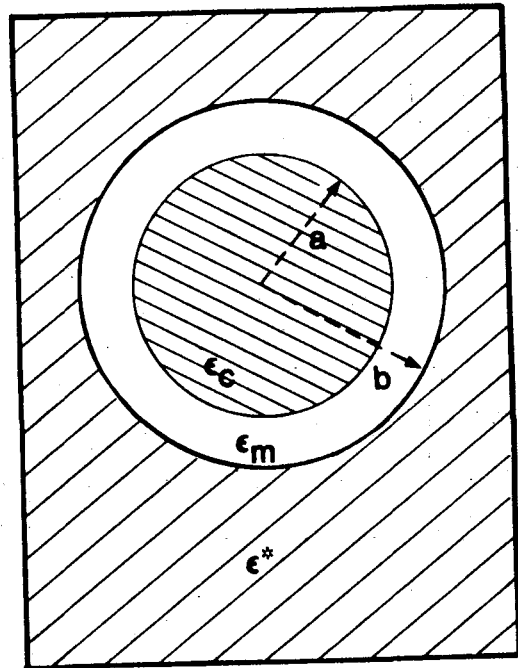
It is frequently assumed that Eq. (IV-18) applies to the case in which the ellipsoidal inclusions have completely random orientations and are not necessarily directed along the space  $x$ ,  $y$  and  $z$  axes. This can be shown to be true for the special case in which ellipsoids of a given type (given  $a$ ,  $b$ ,  $c$ ) have their major axis, say  $c$ , distributed uniformly with respect to solid angle. This is shown in Appendix A. The result for the dielectric constant is identical to Eq. (IV-18).

## B. Extension of the Maxwell-Garnett Theory to High Fill Factors

The Maxwell-Garnett theory, as derived above, obviously breaks down when the distance between inclusions become small. The basic result, Eq. (IV-9), was derived by assuming that the field inside an inclusion is given by Eq. (IV-6), the field which would exist inside an isolated particle. To gain a qualitative understanding of the potential limits of validity of the MG theory, we consider a simple cubic lattice of spheres, with the lattice constant =  $L$  and the sphere diameter =  $r_p$ . The volume fraction  $f$  is then given by  $f = 4\pi r_p^3 / 3L^3$ . When the spheres are just touching,  $L = 2r_p$  and  $f = \pi/6 = 0.524$ . When the spheres are separated by more than a sphere diameter, the effects of sphere-sphere interactions (multipole effects) are small and the spheres can be considered essentially isolated. In this case,  $L = 4r_p$  and  $f = \pi/48 = 0.065$ . Thus, for  $f \geq 0.1$ , the approximations used to derive the MG dielectric constant are not valid.

An alternate derivation of the MG dielectric constant, Eq. (IV-11), from electromagnetic scattering theory increases the upper bound of  $f$  for which the theory is applicable. In this type of derivation, a calculation is made of the scattering from a random unit cell embedded in the effective medium. The effective dielectric constant is found by imposing the requirement that this cell not contribute to the scattering of an incident plane electromagnetic wave.<sup>49, 50</sup> A random unit cell is considered to be composed of a spherical inclusion of radius  $a$  and dielectric constant  $\epsilon_c$  with a concentric shell of medium with dielectric constant  $\epsilon_m$  and outer radius  $b$ . The radii  $a$  and  $b$  are chosen such that the volume fraction of inclusions in the medium is given by  $f = (a/b)^3$ . Fig. IV-2 shows a cell of this type embedded in a homogeneous effective medium with dielectric constant  $\epsilon^*$ . Smith<sup>49</sup> and Niklasson, Granqvist, and Hunderi<sup>50</sup> show that the imposition of the requirement that this unit cell not contribute to scattering

IV-2 A random unit cell in a composite with an effective dielectric constant  $\epsilon^*$ . This cell is considered to be made up of a core of radius  $a$  with dielectric constant  $\epsilon_c$  and a shell of thickness  $t = b - a$  and dielectric constant  $\epsilon_m$ .



of an incident electromagnetic wave to lowest order in an expansion parameter leads directly to the result,  $\epsilon^* = \epsilon_{MG}$ . The expansion parameter is  $k^*b$ , where  $k^*$  is the effective medium propagation vector,  $2\pi/\lambda^*$ , with  $\lambda^*$  = wavelength in the medium. From consideration of higher order terms in the scattering amplitudes, Smith<sup>49</sup> shows that the maximum volume fraction can be extended to  $f_{max} \lesssim 0.5$  for particle sizes typical of those found in black Cr films.

An alternate approach to deriving an expression for the effective dielectric constant of a medium with isolated inclusions is to find the dielectric response of a medium composed of a uniform periodic array of inclusions. Dielectric constants found this way would presumably be more accurate for  $f \gtrsim 0.5$  than the MG expression, Eq. (IV-9). McPhedran and McKenzie<sup>51</sup> have performed an electrostatic calculation for the dielectric constant of a simple cubic (SC) lattice of spherical inclusions, and McKenzie, McPhedran, and Derrick<sup>52</sup> have extended this calculation

to body centered cubic (BCC) and face centered cubic (FCC) spherical arrays. These calculations were performed by finding an approximate solution to Laplace's equation for the potential inside a unit cell of the lattice. The solution was expressed in terms of an infinite series expansion in spherical harmonics,  $Y_{\ell m}(\theta_i, \phi_i)$ , where  $\theta_i$  and  $\phi_i$  are the polar angles of the radius vector extending from the center of the  $i$ th cell to a field point in a "central" cell where the periodic potential is being calculated. The solution was calculated in terms of two expansion parameters,  $M_\theta = \ell_{\max}$  and  $M_\phi < \ell_{\max}$  representing a truncation of the series expansion. For the special case,  $M_\theta = 4$  and  $M_\phi = 0$ , an explicit formula can be written for the dielectric constant  $\epsilon_{MM}$  of the spherical arrays. The expression is given by,

$$\epsilon_{MM} = 1 - 3f/D(f) \quad , \quad (IV-19)$$

where  $f$  = volume fraction of spherical inclusions and the function  $D(f)$  is defined by,

$$D(f) = T_1^{-1} + f - b_1 T_5 f^{14/3} - c_1 T_7 f^6 - a_1 f^{10/3} g(f), \quad (IV-20)$$

$$\text{where } g(f) = \frac{1 - c_2 T_5 f^{11/3} + c_3 T_5^2 f^{22/3}}{T_3^{-1} + b_2 f^{7/3} - c_4 T_5 f^6}$$

The quantities  $T_n$  are defined by

$$T_n = (1 - \epsilon_c/\epsilon_m)/[\epsilon_c/\epsilon_m + (n + 1)/n]$$

and the constants  $a_n$ ,  $b_n$  and  $c_n$  are defined in Table IV-1 for the three types of lattices.

Table IV-1. Parameters Characterizing  $\epsilon_{MM}$ , Eq. (IV-20) for SC, BCC, and FCC Lattices of Spherical Inclusions

Quantity	SC	BCC	FCC
$a_1$	1.3045	0.057467	0.0047058
$b_1$	0.01479	0.166117	0.130683
$b_2$	0.4054	1.35858	1.20500
$c_1$	0.1259	0.000950738	0.00603255
$c_2$	0.5289	0.733934	5.73021
$c_3$	0.06993	0.134665	8.20884
$c_4$	6.1673	0.0465862	0.295595
$f_{\max}$	$\pi/6 \approx 0.524$	$\sqrt{3}\pi/8 \approx 0.680$	$\sqrt{2}\pi/6 \approx 0.740$
$f_c$	0.592	0.730	0.828

The quantity  $f_{\max}$  in Table IV-1 is the volume fraction at which the spherical inclusions touch each other. The quantity  $f_c$  is the volume fraction at which the approximation, Eq. (IV-19), diverges for the case  $\epsilon_c \rightarrow \infty$ ,  $\epsilon_m = 1$ . As  $M_\theta$  and  $M_\phi$  are increased, the numerical calculations of McKenzie, et al.<sup>52</sup> show that  $f_c \rightarrow f_{\max}$  for this special case.

Another periodic structure for which calculations can be made is that of an array of cubes. This structure has the advantage that all volume fractions  $0 < f < 1$  are accessible. However, an exact calculation of the potential of this structure when polarized by a uniform electric field has not, to our knowledge, been made. The induced dipole moment of an isolated dielectric cube subjected to a uniform field has been calculated by Fuchs<sup>53</sup> using an integral equation technique. We have verified the accuracy of Fuch's calculation and have also performed the calculation using an alternate integral equation derived by Van Bladel.<sup>54</sup> In both cases we obtained essentially identical results for both real and complex dielectric constants. This calculation was done because the results reported by Van Bladel for real dielectric constants (Fig. 3.18 of Ref. 54) differ from those computed from Fuchs' result. We feel that the results in Ref. 54 are in error. The calculations are discussed in Appendix B.

Fuchs shows that, for a cube subjected to a uniform field along one of the cube axes, the average dipole moment per unit volume and unit electric field or average susceptibility is given by,

$$\bar{\chi} = \sum_{m=1}^6 \frac{c_m}{\chi^{-1}(\epsilon_C) + 4\pi n_m} \quad (\text{IV-21})$$

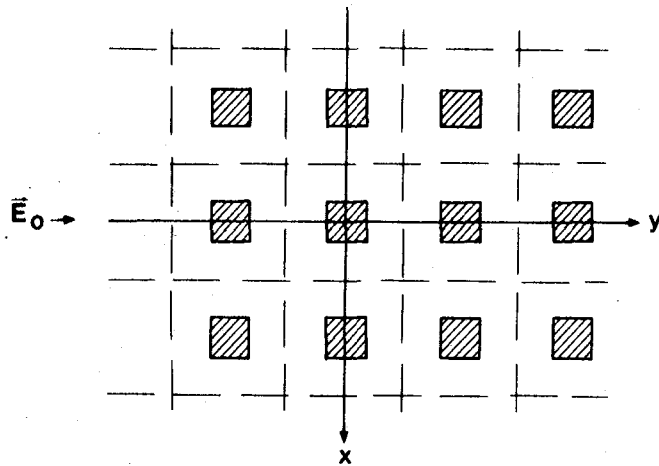
where  $\epsilon_C$  = dielectric constant of the cube material and  $\chi^{-1}(\epsilon_C) = 4\pi / (\epsilon_C - 1)$ . The constants  $c_m$  and  $n_m$  for  $m = 1$  to  $6$  are given by Fuchs. He shows that a Maxwell-Garnett composite medium with cubic inclusions has a dielectric constant,

$$\epsilon_F = \epsilon_m \left[ \frac{4\pi f \epsilon_C \bar{\chi} + (\epsilon_C - \epsilon_m)(1-f)}{4\pi f \epsilon_m \bar{\chi} + (\epsilon_C - \epsilon_m)(1-f)} \right] \quad (\text{IV-22})$$

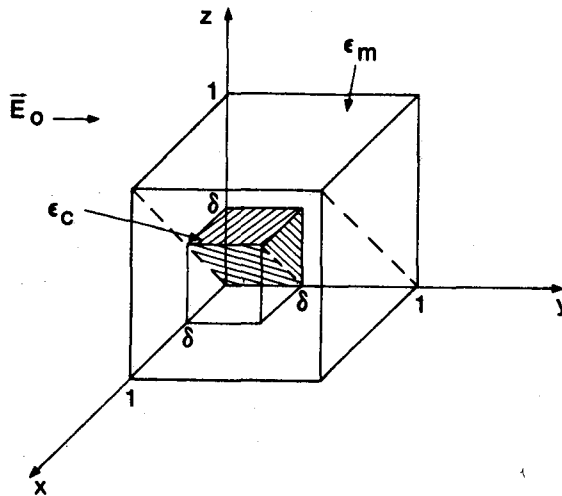
This reduces to Eq. (IV-11) with  $L = 1/3$  when  $4\pi\bar{\chi}$  goes to the spherical particle result,  $4\pi\bar{\chi} \rightarrow [(\epsilon_C/\epsilon_m - 1)^{-1} + 1/3]^{-1}$ .

A cubic array of cubes subject to a uniform field  $\vec{E}_0$  applied in the  $y$  direction is shown in Fig. IV-3. The unit cells of the structure are indicated by the dashed lines. One eighth of a unit cell is shown in Fig. IV-4. Due to the symmetry of the problem, the potential has to be calculated only for  $1/16$  of a unit cell, as indicated by the dashed lines. By symmetry, the planes defined by  $y = 0$  and  $y = 1$  in Fig. IV-3 are equipotential surfaces and the planes defined by  $z = 1$ ,  $x = 0$ , and  $z = x$  are surfaces for which the normal derivative of the potential vanishes. The average dielectric constant of this structure is found by computing the average electric displacement  $\bar{D}$  produced by applying a unit potential between the planes  $y = 0$  and  $y = 1$ .

In analogy with calculations of the electrical or thermal conductivity of distributed structures, the effective dielectric constant may be found by breaking



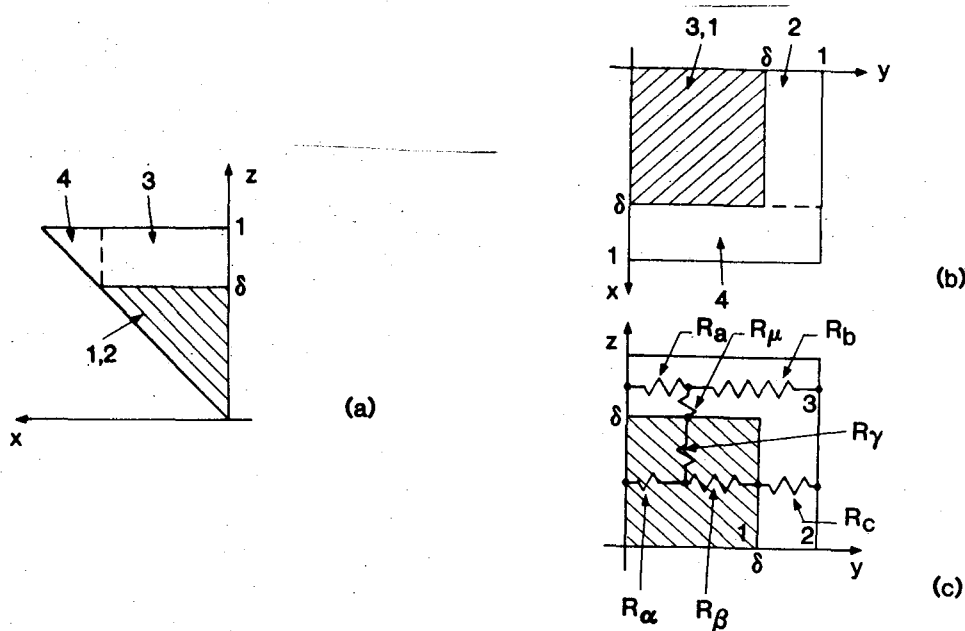
IV-3 Top view of an array of dielectric cubes subject to a uniform applied external field  $\vec{E}_0$ . The dashed lines indicate unit cells in the medium.



IV-4 One eighth of a unit cell from Fig. IV-3. Only one-half of this portion of the cell needs to be analyzed. The shaded region indicates the inclusion boundaries on the reduced 1/16 cell used for analyses.

the structure up into a number of elements and then assigning each element a "resistance" defined by the element geometry.<sup>55</sup> The total resistance of the structure is then found either numerically or analytically if the number of elements is sufficiently small. Variations in results reported in the literature are usually a result of differences in the ways various authors break a given structure up into finite elements.

Projections of the structure shown in Fig. IV-4 on the x-z, x-y, and y-z planes are shown in Fig. IV-5 where the various elements we have used are labeled. The resistor network shown in Fig. IV-5(c) is combined with a parallel resistor,  $R_x$  representing the resistance of region 4 in Fig. IV-5(a). The total resultant network is shown in Fig. IV-6. The various resistors are assigned the values,



IV-5 Projections of the 1/16 unit cell in Fig. IV-4(a) projection on the x-z plane, (b) projection on the x-y plane, (c) projection on the z-y plane showing assignment of resistors to various parts of the structure. Resistor  $R_4$ , assigned to the upper triangular shaped region in (a) is not shown.

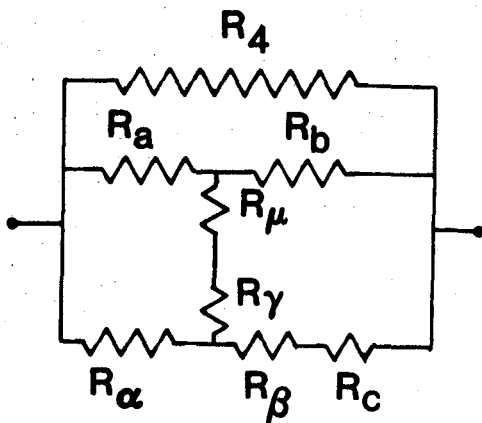
$$\begin{aligned}
 R_4 &= 1/[(1 - \delta^2)/2] & R_c &= (1 - \delta)/(\delta^2/2) & (IV-23) \\
 R_a &= 1/[2(1 - \delta)] & R_\alpha &= R_\beta = p/\delta \\
 R_b &= (1 - \delta/2)/[\delta(1 - \delta)] & R_\gamma &= p/2\delta \\
 & & R_\mu &= (1 - \delta)/(2\delta^2)
 \end{aligned}$$

In Eq. (IV-23),  $p = (\epsilon_c/\epsilon_m)^{-1}$  and  $\delta =$  half length of a cubic inclusion. The effective dielectric constant of the structure is found by finding the equivalent conductance of the network in Fig. IV-6.

If the shunt resistors  $R_\mu$  and  $R_\gamma$  are assumed not to be present, then the result found is identical to that reported by son Frey<sup>56</sup> for an equivalent thermal conductivity calculation,

$$\epsilon_{SF}(\delta) = \epsilon_m \left\{ \frac{1 - \delta + \delta^3 + (\delta - \delta^3)\epsilon_m/\epsilon_c}{1 - \delta + \delta\epsilon_m/\epsilon_c} \right\} \quad (IV-24)$$

The volume fraction is related to  $\delta$  by  $f = \delta^3$  or  $\delta = f^{1/3}$ . The result of our calculation with the shunt resistors included is,



IV-6 Equivalent circuit used to calculate the effective dielectric constant  $\epsilon^*$  of Eq. (IV-25). The "resistor" values are given in Eq. (IV-23).

$$\epsilon^*(\delta) = \epsilon_m[(1 - \delta)^2 + 2A/B] \quad (IV-25)$$

$$A = \delta(1 - \delta)[p\delta/2 + (1 - \delta)][\delta^2/2 + (1 - \delta/2)\delta + 2(1 - \delta^2) + 2p\delta(1 - \delta)] \\ + \delta^2[\delta/2 + p(1 - \delta)][p\delta(1 - \delta) + \delta(1 - \delta/2) + 2(1 - \delta)^2]$$

$$B = \frac{p\delta^2}{2} [p\delta(1 - \delta) + 2(1 - \delta)^2 + \delta(1 - \delta/2)] \\ + \delta(1 - \delta/2)[p\delta + 2(1 - \delta)][\delta/2 + p(1 - \delta)] \\ + (1 - \delta)(p\delta + 1 - \delta)^2 ,$$

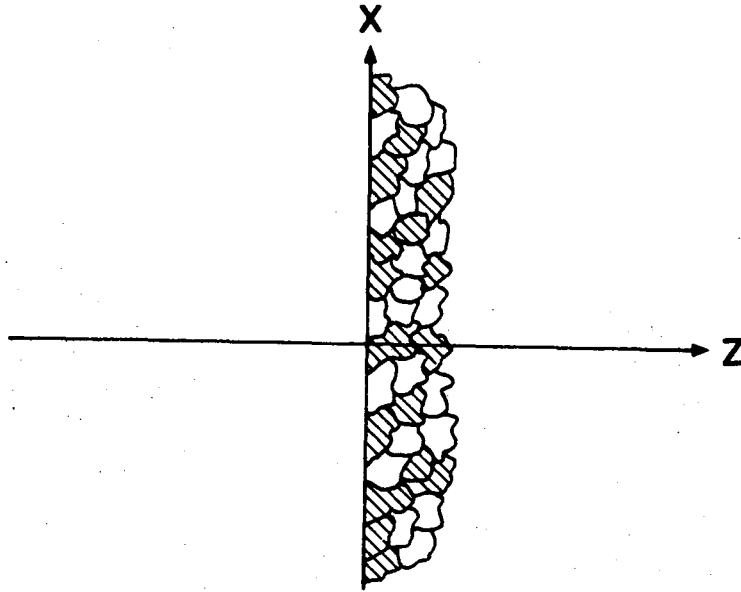
with  $p = \epsilon_m/\epsilon_c$  and  $\delta = f^{1/3}$ .

Consideration of the physics of the problem indicates that Eq. (IV-25) is likely to be most valid at high volume fractions when the shunt flux in the z direction is relatively small. At small volume fractions there will be a large z directed flux and the Fuchs expression, Eq. (IV-22), should be more accurate, since full consideration of shunt flux was automatically taken into account in the isolated cube polarization calculations.

The Bruggeman dielectric constant can be derived easily from a model of the composite similar to that shown in Fig. IV-1(a). In Fig. IV-7 a composite is shown in which both the matrix and the inclusions are in a particulate or symmetrical form. The most significant field polarizing a "particle" of either matrix or inclusion is assumed to be the mean field in the composite,  $E_B$ . Then, the average field is obtained by summing the internal particulate fields over all regions, i.e.,

$$\bar{E} = E_B = \sum_j f_j E_{in}(j) \quad , \quad (IV-26)$$

where the index j runs over particles of both types (matrix and inclusion) and over all orientations and eccentricities. Implicit in this procedure is the replacement of the actual particulate medium by a set of approximating ellipsoids,



IV-7 A Bruggeman composite medium in the half-space  $z > 0$ . The inclusions (shaded regions) and matrix (clear regions) are assumed to be topologically equivalent and randomly distributed.

similar to the replacement in the Maxwell-Garnett case. In this case, however, the replacement is not as physically meaningful because the whole composite space cannot be filled with ellipsoids in contact. Using Eq. (IV-6) for the internal field expression, with the polarizing field  $E_m$  replaced by  $E_B$ , and  $\epsilon_m$  replaced by  $\epsilon_B$ . Eq. (IV-26) yields,

$$E_B = \sum_j \frac{\epsilon_B E_B f_j}{L_j \epsilon_j + (1 - L_j) \epsilon_B}, \quad \text{or} \quad (\text{IV-27})$$

$$\sum_j \frac{f_j}{L_j \frac{\epsilon_j}{\epsilon_B} + (1 - L_j)} = 1 \quad (\text{IV-28})$$

Eq. (IV-28) is the fundamental relation of the generalized Bruggeman theory. In Eqs. (IV-27) and (IV-28),  $\epsilon_j = \epsilon_c$  for inclusion particles and  $\epsilon_j = \epsilon_m$  for matrix particles. Since Eq. (IV-28) is not linear in  $\epsilon_B$ , it has been utilized only in certain special and highly restricted cases where it can be explicitly solved.

For the special case of one type of inclusion and one type of matrix particle, Eq. (IV-28) reduces to a second order equation in  $\epsilon_B$  which is soluble in closed form. If it is assumed that the inclusions are ellipsoidal with a depolarizing factor  $L$  and the matrix particles are spherical, then Eq. (IV-28) becomes,

$$[(S - 1) + f(3 - S)]\epsilon_B^2 - \gamma\epsilon_B - \epsilon_m\epsilon_c = 0 \quad (IV-29)$$

where  $S = 1/L$  and  $\gamma$  is given by,

$$\gamma = \epsilon_m[S(1 - f) - 1] + \epsilon_c[3f - 1] \quad (IV-30)$$

In the even more restricted case in which the inclusions are spherical with  $L = 1/3$ , the solution to Eq. (IV-28) is given by<sup>34</sup>

$$\epsilon_B = \frac{1}{4} [\gamma + (\gamma^2 + 8\epsilon_m\epsilon_c)^{1/2}] \quad (IV-31)$$

where

$$\gamma = [3(1 - f) - 1] \epsilon_m + (3f - 1) \epsilon_c$$

A situation of interest in black Cr calculations is that of an assembly of coated spheres in a medium of dielectric constant  $\epsilon_m$ . An isolated coated sphere in a uniform field behaves in a manner analogous to that of a single material sphere. If the coated sphere has a core with dielectric constant  $\epsilon_c$  and radius  $r_c$  and a shell with dielectric constant  $\epsilon_s$  and thickness  $t_s$ , then the dielectric constant characterizing the coated sphere is,<sup>57</sup>

$$\epsilon_{cs} = \epsilon_s \left[ \frac{2\epsilon_s + \epsilon_c + 2\Omega(\epsilon_c - \epsilon_s)}{2\epsilon_s + \epsilon_c - \Omega(\epsilon_c - \epsilon_s)} \right] \quad (IV-32)$$

The quantity  $\Omega$  is the ratio of core volume to total particle volume and is given by,  $\Omega = [r_c / (r_c + t_s)]^3$ . Eq. (IV-32) may be easily verified by solving Laplace's equation in spherical coordinates for an isolated coated sphere subject to a uniform external field. The resultant perturbation field is equivalent to that produced by a uniform sphere of radius  $= r_c + t_s$ , with a dielectric constant given by Eq. (IV-32). Lamb, Wood and Ashcroft have pointed out that Eq. (IV-32) is equivalent to the MG spherical particle result, Eq. (IV-11) with  $\Omega = f$ ,  $L = 1/3$ , and  $\epsilon_s = \epsilon_m$ .<sup>57</sup> In calculations on black Cr coatings, Eq. (IV-32) will be used for  $\epsilon_{CS}$ , with  $\epsilon_c = \epsilon_{Cr}$  and  $\epsilon_s = \epsilon_{Cr_2O_3}$ , while  $\epsilon_m$  will be assumed to be unity.

### C. Optical Properties

In order to perform reflectance calculations, values are required for the complex index of refraction of the materials in the reflecting system. This index of refraction is defined by the relation  $\tilde{n} = n + jk$ , where  $n$  and  $k$  are the real and imaginary parts of the index respectively and  $j = \sqrt{-1}$ . The index of refraction  $\tilde{n}$  and the complex dielectric constant  $\epsilon = \epsilon_1 + j\epsilon_2$  are related by the formula,

$$\tilde{n} = \epsilon^{1/2} \quad . \quad (IV-33)$$

Eq. (IV-33) may be used to express  $\epsilon_1$  and  $\epsilon_2$  in terms of  $n$  and  $k$  to yield,

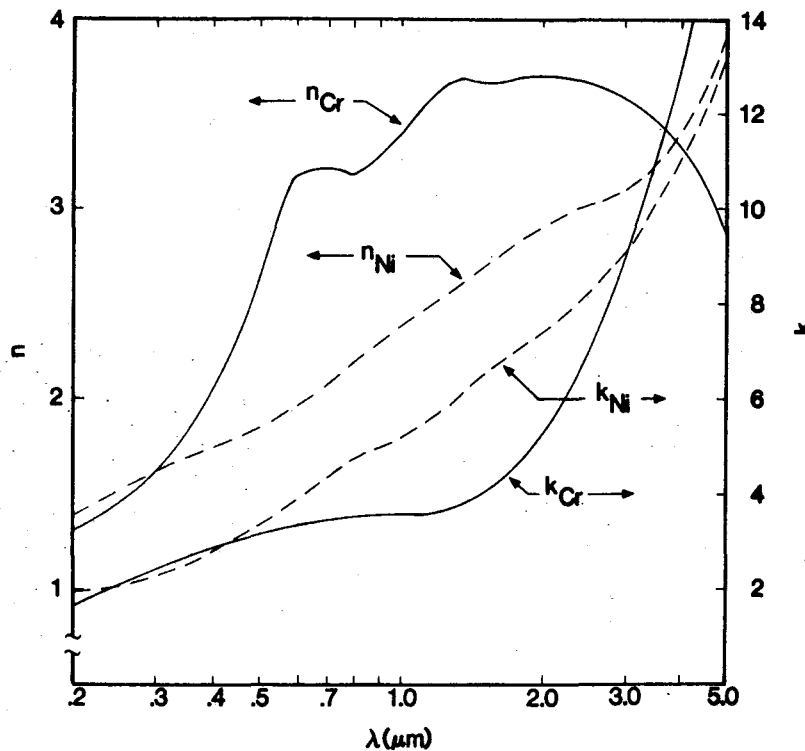
$$\begin{aligned} \epsilon_1 &= n^2 - k^2 \\ \epsilon_2 &= 2nk \end{aligned} \quad (IV-34)$$

Alternatively,  $n$  and  $k$  may be expressed in terms of  $\epsilon_1$  and  $\epsilon_2$  via the relations,

$$n^2 = \left| \epsilon_1 \right| \left\{ \frac{\epsilon_1/|\epsilon_1| + \left[ 1 + (\epsilon_2/\epsilon_1)^2 \right]^{1/2}}{2} \right\} \quad (\text{IV-35})$$

$$k^2 = \left| \epsilon_1 \right| \left\{ \frac{\left[ 1 + (\epsilon_2/\epsilon_1)^2 \right]^{1/2} - \epsilon_1/|\epsilon_1|}{2} \right\}$$

The  $n$  and  $k$  values used for Cr and Ni in the wavelength interval  $0.2 \mu\text{m} < \lambda < 5.0 \mu\text{m}$  are shown in Fig. IV-8. For Cr, the  $n$  and  $k$  values reported by Johnson and Christy<sup>58</sup> were used for  $\lambda < 2 \mu\text{m}$  and those reported by Barker and Ditzemberger<sup>60</sup> were used for  $\lambda > 2 \mu\text{m}$ . Although both references report the same general dependence of  $n$  and  $k$  on  $\lambda$  in the region  $1 \mu\text{m} \lesssim \lambda \lesssim 2 \mu\text{m}$ , they do not agree exactly on the magnitude of  $n$  and  $k$ . Consequently the  $n$  and  $k$  values shown in Fig. IV-8 were derived by smoothly joining the Johnson and Christy short wavelength data with the Barker and Ditzemberger long wavelength data.



IV-8 Real,  $n$ , and imaginary,  $k$ , parts of the complex index of refraction for Cr and Ni as derived from Refs. 58-60.

The real and imaginary parts of the complex index of refraction for Ni were similarly obtained by interpolating between short wavelength data reported by Johnson and Christy<sup>58</sup> and longer wavelength data reported by Siddiqui and Treherne.<sup>60</sup> In this case, the two sets of data joined quite well.

The optical dielectric constant for  $\text{Cr}_2\text{O}_3$  has been derived from reflectance measurements on single crystals by Renneke and Lynch<sup>61</sup> and by Lucovsky, Sladek, and Allen.<sup>62</sup> In Ref. 61,  $\epsilon_1$  is reported to be 6.1 or 6.2 for the incident electric field vector parallel or perpendicular to the crystal C axis respectively, while Ref. 62 gives  $\epsilon_1 = 5.7$  or 6.0 for these two cases.  $\epsilon_2$  is estimated to be very small at optical frequencies,  $\epsilon_2 \lesssim 5 \times 10^{-3}$ . Frank and Mombert<sup>63</sup> report an index of refraction  $n = 2.4$  for a reactively evaporated  $\text{Cr}_2\text{O}_3$  film, corresponding to  $\epsilon_1 = 5.8$ . Frequently, the oxide in black Cr films is assumed to be in an amorphous phase and the oxide index of refraction is used as an adjustable parameter in matching theory to experiment.<sup>7,26</sup> We have taken the point of view that since the oxide grows in crystalline form around the Cr crystallites in the coating during aging, the values  $n_{\text{Cr}_2\text{O}_3} = 2.5$  and  $k_{\text{Cr}_2\text{O}_3} = 0$  are appropriate for use in these calculations.

#### D. Comparison of Model Dielectric Constant Dependence on Volume Fraction

One of the goals of this investigation was to decide which of the model dielectric constants for inhomogeneous media yielded the best agreement between calculated and experimental spectral reflectance curves for black Cr films. Niklasson and Grandqvist<sup>64</sup> have examined and reviewed the subject of bounds on the values of the effective medium dielectric constant and have demonstrated, for a system of spherical Co particles in an  $\text{Al}_2\text{O}_3$  dielectric matrix, that a number of different theoretical formulations can lead to large variations in

the calculated spectral reflectance. They concluded that microstructural information is essential in determining the correct effective medium theory to utilize.

It would appear from the microstructural studies described in Sec. III that black Cr films are composed of fine metallic Cr particles, possibly with oxide coatings distributed in a matrix and that there is not topological equivalence between the particles and the matrix. Hence the MG theory might be felt to be more applicable a-priori. This is the point of view expressed by Smith<sup>65</sup> and by Sievers.<sup>66</sup> There is, however, some uncertainty about the precise nature of the black Cr microstructure, especially the character of the matrix. This will be discussed more fully in Sec. V-B. In this section, the fundamental dependence of the various effective medium dielectric constants on inclusion volume fraction,  $f$ , will be discussed. The inclusions will be taken to be Cr particles and the matrix air with  $\epsilon_m = 1$ .

For simplicity in the following analysis, the inclusions will be assumed to be spherical with  $L_i = 1/3$  for all  $i$ . The solar spectrum covers the wavelength region,  $0.2 \mu\text{m} < \lambda < 2 \mu\text{m}$  and hence it is of interest to examine the behavior of the various dielectric constants in this interval. For illustrative purposes, we shall display some calculated results for  $\lambda = 1 \mu\text{m}$ . For this wavelength, Fig. IV-8 and Eqs. IV-34 can be used to find the real and imaginary parts of  $\epsilon_{\text{Cr}}$ :  $\epsilon_{\text{Cr}_1}(1 \mu\text{m}) = -1.05$  and  $\epsilon_{\text{Cr}_2}(1 \mu\text{m}) = 24.44$ . For spherical particles, the MG result, Eq. (IV-11) becomes,

$$\epsilon_{\text{MG}} = \frac{(\epsilon_{\text{Cr}} + 2) + 2f(\epsilon_{\text{Cr}} - 1)}{(\epsilon_{\text{Cr}} + 2) - f(\epsilon_{\text{Cr}} - 1)} \quad (\text{IV-36})$$

As  $f \rightarrow 0$ ,  $\epsilon_{\text{MG}} \rightarrow 1$  and as  $f \rightarrow 1$ ,  $\epsilon_{\text{MG}} \rightarrow \epsilon_{\text{Cr}}$ , as it must. As  $f$  varies from 0 to 1,  $\epsilon_{\text{MG}}$  varies smoothly between 1 and  $\epsilon_{\text{Cr}}$ . However, for  $\lambda \gtrsim 0.2 \mu\text{m}$ ,  $|\epsilon_{\text{Cr}}| \gg 1$ ,

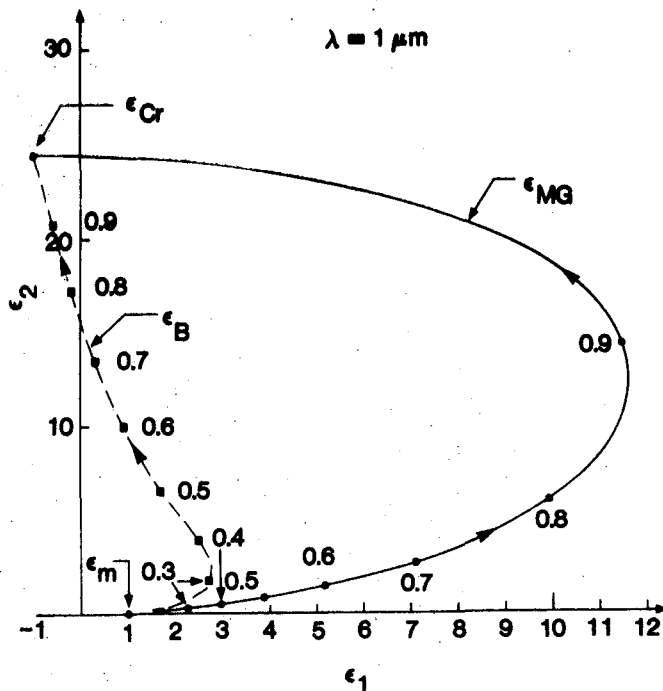
and hence the common term  $\epsilon_{Cr} + 2$  in the numerator and denominator of Eq. (IV-36) will tend to keep  $|\epsilon_{MG}|$  close to unity until  $f$  becomes quite large. In contrast to this type of behavior,  $\epsilon_B$  assumes characteristics of  $\epsilon_{Cr}$  at much lower  $f$  values than does  $\epsilon_{MG}$ . The expression for  $\epsilon_B$  in Eq. (IV-31), with  $\epsilon_m = 1$ , can be written as,

$$\epsilon_B = \frac{\gamma}{4} \left[ 1 + (1 + 8\epsilon_{Cr}/\gamma^2)^{1/2} \right] \quad (IV-37)$$

$$\gamma = 2 - 3f + (3f - 1)\epsilon_{Cr}$$

From Eq. (IV-37) it can be seen that  $\epsilon_B$  is essentially linear in  $\epsilon_{Cr}$  with a coefficient of  $3f - 1$ .

Plots of  $\epsilon_{MG}$  and  $\epsilon_B$  in the complex  $\epsilon$  plane ( $\epsilon = \epsilon_1 + j\epsilon_2$ ) are shown in Fig. IV-9, for spherical Cr inclusions in an air matrix and  $\lambda = 1 \mu\text{m}$ . Each trajectory is labeled with the inclusion volume fraction as a parameter, with

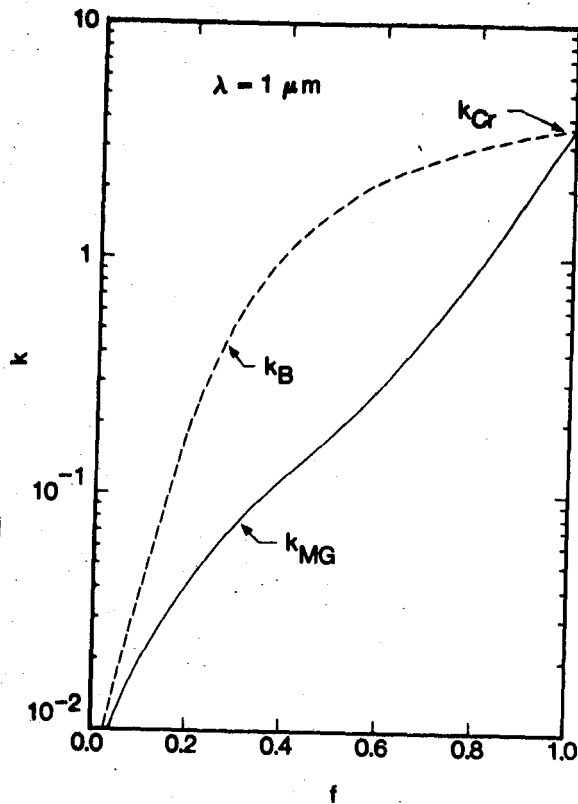


IV-9 Trajectories of  $\epsilon_{MG}$  and  $\epsilon_B$  at  $\lambda = 1 \mu\text{m}$  in the complex  $\epsilon$  plane for Cr spherical inclusions in an air matrix. The labeled points on the trajectories represent volume fractions of Cr associated with those points.

the arrows on the trajectories pointing in the direction of increasing  $f$ . It can be seen that  $\epsilon_{MG}$  retains the characteristics of the medium until fairly high  $f$  values are attained, while  $\epsilon_B$  develops a large imaginary component at relatively low volume fractions. The imaginary component  $k$  of the complex index of refraction, as calculated from the second of Eqs. (IV-35) is shown in Fig. IV-10 for  $\lambda = 1 \mu\text{m}$ . It is evident that  $k_B$  increases much more rapidly with increasing  $f$  than does  $k_{MG}$ . Substantial differences between  $k_{MG}$  and  $k_B$  occur for  $0.05 \lesssim f \lesssim 0.90$ . Since  $k$  is responsible for producing absorption in films, the Bruggeman theory will lead to higher predicted absorptances than the MG theory at a given wavelength.

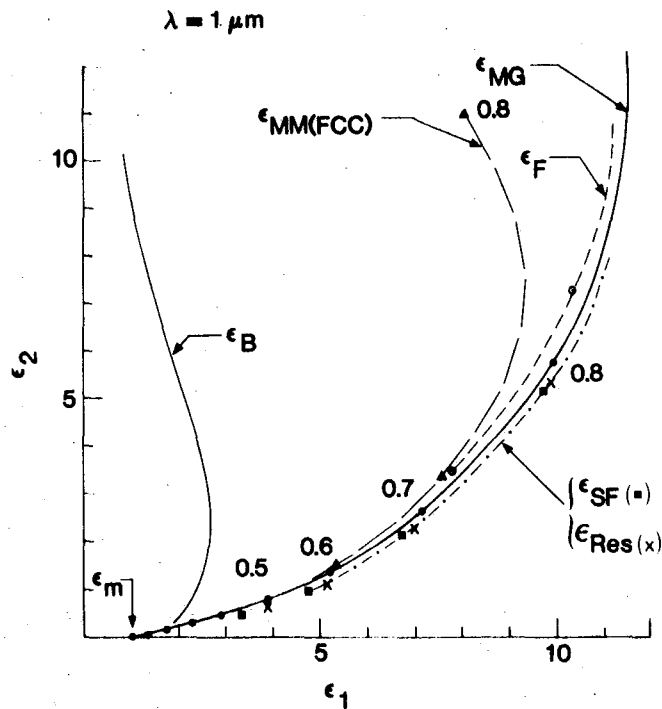
The substantial deviation of  $\epsilon_B$  from  $\epsilon_{MG}$  shown in Fig. IV-9 for  $f \gtrsim 0.2$  is an example of what is called a "percolation" phenomena.<sup>34</sup> Percolation refers to the sudden onset of electrical conduction at a critical value of  $f$  in a composite consisting of conducting inclusions in an insulating matrix. In the dielectric mixture case, this is equivalent to a situation in which  $|\epsilon_c/\epsilon_m| \rightarrow \infty$ . It has long been known that the Bruggeman theory has a "percolation threshold" at  $f \approx 0.33$ , while the MG theory predicts a finite conductivity for any non-zero value of  $f$ .<sup>34</sup> For Cr particles in a vacuum matrix,  $|\epsilon_c/\epsilon_m| = 24.5$  and so  $\epsilon_B$  display characteristics of percolation behavior near  $f \sim 0.3$ . However, as shown in Fig. IV-10, there is no sudden onset of percolation, as would be indicated by a sudden increase of  $k_B$  relative to  $k_{MG}$ , for this system.

A comparison of the volume fraction dependence of several of the model dielectric constants discussed above is shown in Fig. IV-11. In this figure, the results are plotted for a MG medium with spherical inclusions ( $\epsilon_{MG}$ , solid line, solid circles), a face centered cubic array of spheres calculated from Eqs. (IV-19) and (IV-20) ( $\epsilon_{MM}(\text{FCC})$ , large dashed line, triangles), the son Frey dielectric constant from Eq. (IV-24) ( $\epsilon_{SF}$ , dot-dash line, solid squares), the



IV-10 The imaginary part,  $k$ , of the complex index of refraction for a material with Cr spherical inclusions in an air matrix at  $\lambda = 1 \mu\text{m}$ .

"resistor model" dielectric constant from Eq. (IV-25) ( $\epsilon_{Res}$ , dot-dash line, X symbols), and the dielectric constant found from Eq. (IV-22) for an MG effective medium with cubic inclusions ( $\epsilon_F$ , short dash line, open circles). The plotting symbols on the curves represent the points at which the adjacent  $f$  values are assumed. It is evident that the son Frey and resistor model predict essentially identical results and that these results are close to those for an MG medium with spherical or cubic inclusions. The McPhedran and McKenzie dielectric constant for an FCC array of spheres remains very close to  $\epsilon_{MG}$  until  $f \gtrsim 0.7$ . As shown in Table IV-1, the limit of validity for an FCC array is  $f < 0.74$ .



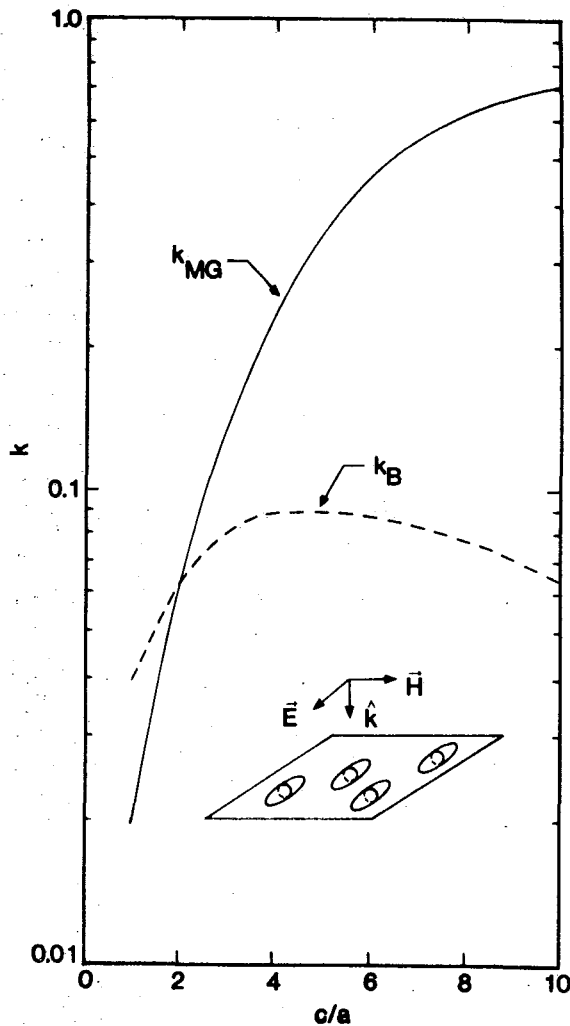
IV-11 Comparison of the trajectories of several model dielectric constants.  $\epsilon_B$  and  $\epsilon_{MG}$  are the same as in Fig. IV-9.  $\epsilon_{Res}$  is from Eq. (IV-25).  $\epsilon_{SF}$  is from Eq. (IV-24).  $\epsilon_{MM(FCC)}$  is the face-centered cubic version of  $\epsilon_{MM}$ , Eqs. (IV-19) and (IV-20) and Table IV-1.  $\epsilon_F$  is from Eq. (IV-21) and Ref. 53.

From the above analysis, based on electrostatic calculations, it can be seen that a composite medium with a periodic array of inclusions can have an effective dielectric constant similar to  $\epsilon_{MG}$ , even at very high volume fractions. We speculate that a nonperiodic or random array of roughly spherical (or cubic) inclusions can also have a dielectric constant dependence on volume fraction similar to that of  $\epsilon_{MG}$ .

#### E. Effect of Particle Eccentricity

The presence of highly eccentric absorbing inclusions with the long axis in the plane of the film will increase absorption at a given wavelength because

these particles are more easily polarized than are spherical particles. The result has been demonstrated explicitly by Van de Hulst who shows that the absorption cross section of an isolated inclusion is proportional to the imaginary part of the polarizability, Eq. (IV-10), in the limit where the wavelength is much larger than the inclusion length.<sup>67</sup> Eq. (IV-10) shows that the polarizability,  $\alpha$ , increases as the depolarizing factor  $L$  decreases, and Eq. (IV-13) shows that  $L$  decreases approximately as  $r^{-2}$  as the eccentricity  $r$  increases. This effect has been discussed by Granqvist and Hunderi<sup>39</sup> who show that the absorptance at a given wavelength does in fact increase as the particle eccentricity increases in the plane of the film. This increased absorptance effect can be illustrated by using Eq. (IV-11) for  $\epsilon_{MG}$  and considering a film consisting of chrome prolate spheroids in a medium with  $\epsilon_m = 1$ . The  $c$  axis of the particles is aligned along the direction of the incident electric field. Fig. IV-12 shows the imaginary part of the refractive index,  $k_{MG}$  and  $k_B$  vs the chrome particle  $c/a$  ratio at  $\lambda = 1 \mu\text{m}$  and  $f = 0.1$ . The inset to Fig. IV-12 shows the assumed geometry, with prolate ellipsoidal particles having their  $c$  axes aligned with the incident  $\vec{E}$  vector.  $k_{MG}$  increases very rapidly with increasing  $c/a$ , indicating rapidly increasing absorption with increasing eccentricity. The variation of the complex MG dielectric constant with particle eccentricity is shown in Fig. IV-13. The solid lines are the trajectories of  $\epsilon_{MG}$  with increasing  $f$  for  $r = 1, 2, 4$  and  $6$ . The dashed lines represent trajectories of increasing  $r$  for constant  $f$  and the dot-dash line represents  $\epsilon_B$  for  $r = 1$ . From this figure it is evident that as the eccentricity increases,  $\epsilon_{MG}$  acquires more of the characteristics of  $\epsilon_B$ . In the limit  $c/a \rightarrow \infty$  or  $L \rightarrow 0$ , Eq. (IV-11) may be used to show that,

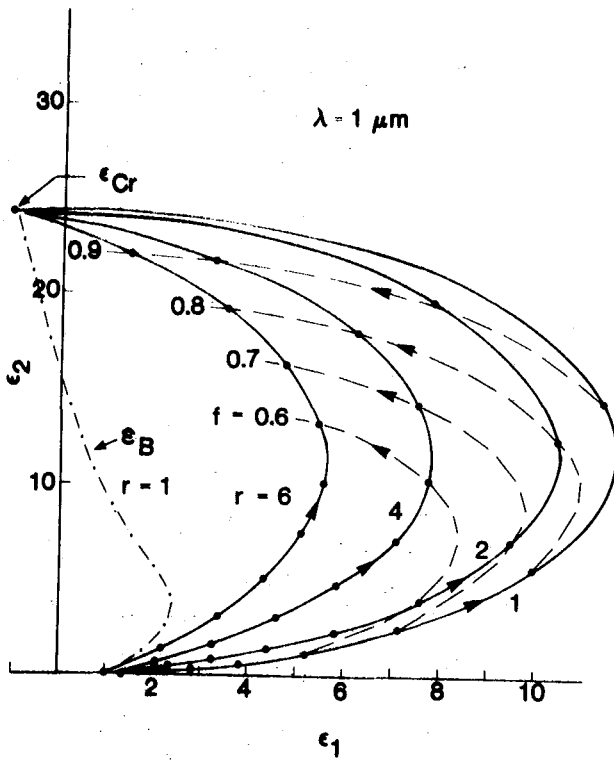


IV-12 Imaginary part of the complex index of refraction vs particle eccentricity for prolate ellipsoidal Cr inclusions in an air matrix at  $f = 0.1$  and  $\lambda = 1 \mu\text{m}$ . The inset shows the assumed geometry with the ellipsoid  $c$  axes aligned along the incident  $\vec{E}$  field direction  $c =$  length of the semi-major axis and  $a =$  length of the semi-minor axis.

$$\epsilon_{MG} \rightarrow f\epsilon_{Cr} + (1 - f)\epsilon_m \quad (IV-38)$$

Thus for a system of highly eccentric oriented particles,  $\epsilon_{MG}$  approaches the volume averaged dielectric constant.

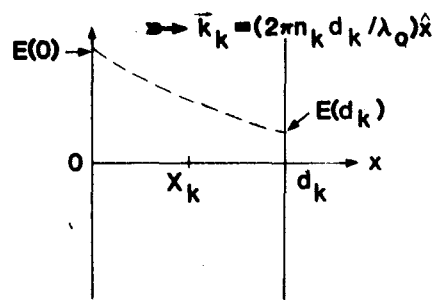
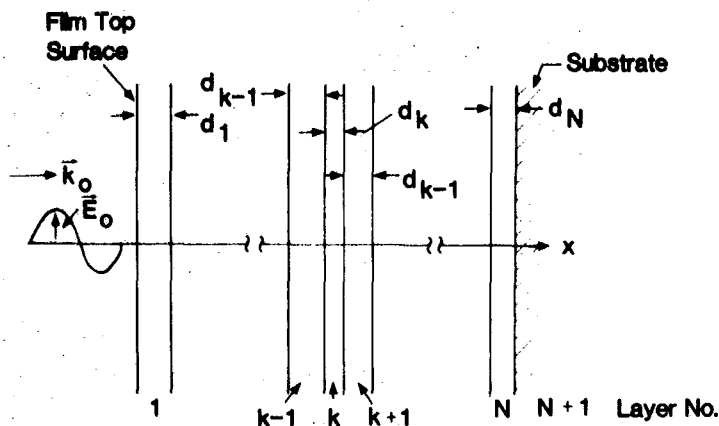
In contrast to the  $\epsilon_{MG}$  behavior,  $\epsilon_B \rightarrow \epsilon_m$  as  $L \rightarrow 0$  and  $k_B$  consequently decreases as shown in Fig. IV-12. Eqs. (IV-29) and (IV-30) may be used to show that, for  $f < 1$ ,  $\epsilon_B \rightarrow \epsilon_m$  independent of the value of  $\epsilon_c$  as  $L \rightarrow 0$  ( $S \rightarrow \infty$ ). This occurs because  $\epsilon_c$  occurs only in the denominator of one of the terms in Eq. (IV-28) and it is multiplied by  $L$ . Hence in the Bruggeman theory absorption is increased somewhat as highly eccentric metal particles become more spherical and in the MG theory high absorption is produced by the high eccentricity included particles.



IV-13 Trajectories of  $\epsilon_{MG}$  in the complex  $\epsilon$  plane at  $\lambda = 1 \mu m$  as a function of  $f$  and  $r = c/a$ . The solid lines show the variation of  $\epsilon_{MG}$  with  $f$  at constant  $r$  and the dashed lines show the variation of  $\epsilon_{MG}$  with  $r$  at constant  $f$ . For comparison,  $\epsilon_B$  is shown by the dot-dash trajectory. It can be seen that  $\epsilon_{MG}$  becomes more like  $\epsilon_B$  as  $r$  increases.

#### F. Reflectance Calculations

The calculation of reflectance for a system of uniform layers and normally incident radiation can be performed in a straightforward way by the Rouard's method as described in detail by Heavens<sup>68</sup> and summarized by Chang and Hall.<sup>35</sup> In this technique, the model system illustrated in Fig. IV-14 is considered. This system consists of  $N$  layers of material, indexed by the letter  $k$ , each with a uniform dielectric constant  $\tilde{n}_k = n_k + jk_k$  and a thickness  $d_k$  as shown. The substrate is a uniform semiinfinite material with an index of refraction  $\tilde{n}_{N+1}$ . The reflectance of the  $N$  layer stack is found by first calculating the reflectance for a system composed of the substrate and the  $N$ th layer and then back calculating the reflectance



- IV-14 (a) Model film structure used in optical reflectance calculations. The film consists of  $N$  layers on semi-infinite substrate. Layer  $k$  has a thickness  $d_k$ . A plane electromagnetic wave with an electric field  $\vec{E}_0$  and propagation vector  $\vec{k}_0 = (2\pi/\lambda_0)\hat{x}$  is incident from the left.
- (b) Variation of the electric field strength within layer  $k$ .  $E(d_k)$  is related to  $E(0)$  by Eq. (IV-31).

of system composed of the  $(N - 1)$ st layer and joint  $N$ th layer-substrate system. The reflectance coefficient for the  $N$ th layer-substrate interface is given by,<sup>35</sup>

$$\tilde{R}_{N+1} = (\tilde{n}_N - \tilde{n}_{N+1}) / (\tilde{n}_N + \tilde{n}_{N+1}) \quad (\text{IV-38})$$

$\tilde{R}_{N+1}$  is the ratio of the reflected to incident electric field strength at the interface between layers  $N$  and  $N + 1$ . The complex reflectance or Fresnel coefficient for the  $N$ th layer may now be found from the relation,

$$\tilde{F}_N = \frac{\tilde{R}_N + \tilde{R}_{N+1} \exp(-2j\delta_N)}{1 + \tilde{R}_N \tilde{R}_{N+1} \exp(-2j\delta_N)} \quad (\text{IV-39})$$

where  $\delta_N = 2\pi d_N \tilde{n}_N / \lambda_0$  and  $\tilde{R}_N$  is found from Eq. (IV-38) by replacing  $N$  by  $N - 1$ .

The Fresnel coefficient for the general  $k$ th layer is,

$$\tilde{F}_k = \frac{\tilde{R}_k + \tilde{F}_{k+1} \exp(-2j\delta_k)}{1 + \tilde{R}_k \tilde{F}_{k+1} \exp(-2j\delta_k)} \quad (\text{IV-40})$$

The calculation of the  $\tilde{F}_k$  proceeds via the scheme  $\tilde{F}_N \rightarrow \tilde{F}_{N-1} \rightarrow \dots \tilde{F}_k \rightarrow \dots \tilde{F}_1$ , and the stack reflectance  $R$  is given by,

$$R = \tilde{F}_1 \cdot \tilde{F}_1^* \quad , \quad (\text{IV-41})$$

where  $\tilde{F}_1^*$  is the complex conjugate of  $\tilde{F}_1$ .

A model stack is illustrated in Fig. IV-14(a). For a wave with a free space wavelength  $\lambda_0$  traveling to the right in the  $k$ th layer, the ratio of the electric field strength at the right boundary to that at the left boundary is, as shown in Fig. IV-14(b),

$$E(d_k)/E(0) = \exp[2\pi j \tilde{n}_k d_k / \lambda_0] \quad (\text{IV-42})$$

$$= \exp[2\pi j n_k d_k / \lambda_0] \exp[-2\pi k_k d_k / \lambda_0]$$

Eq. (IV-42) shows that the traveling wave is attenuated by a factor  $\exp[-2\pi k_k d_k / \lambda_0]$  in crossing the  $k$ th layer and hence a large value of  $k_k$  leads to large absorptance in the  $k$ th layer.

For calculations with graded layer black Cr films, the film is broken up into a large number of layers, typically ~75-100, each with its own Cr particle volume fraction,  $f_{Cr}(x_k)$ , where  $x_k$  is the centerline coordinate of the  $k$ th layer. Two model functions have been utilized for reflectance calculations, a general power law function given by

$$f_{Cr}(x) = f_{Cr-\min} + (n + 1)(\bar{f}_{Cr} - f_{Cr-\min}) \left(\frac{x}{L}\right)^n \quad , \quad (\text{IV-43})$$

and a sinusoidal or sigmoid function given by,

$$f_{Cr}(x) = f_{Cr-\min} + \frac{\pi}{2} (\bar{f}_{Cr} - f_{Cr-\min}) \sin\left(\frac{\pi x}{2L}\right) \quad (\text{IV-44})$$

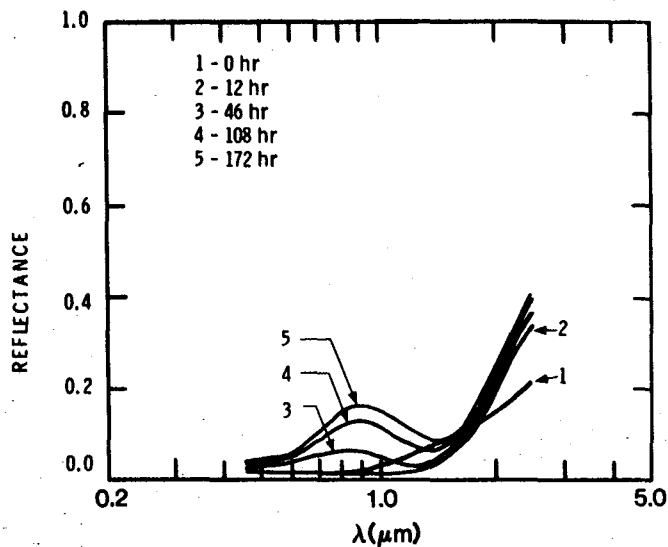
In Eqs. (IV-43) and (IV-44),  $f_{Cr}$  is the average chrome volume fraction,  $f_{Cr-min}$  is the Cr volume fraction at the film top surface, and  $L$  = film thickness. Most of the calculations were done with the power law profile, Eq. (IV-43) and  $f_{Cr-min} = 0$ , as the sigmoid distribution, Eq. (IV-44) did not typically yield good agreement with experimental data. When Eq. (IV-43) is used, the maximum value of  $n$  is restricted for a given  $\bar{f}_{Cr}$  by the requirement  $f_{Cr}(L) < 1$ , yielding,  $n + 1 < 1/\bar{f}_{Cr}$ . Typically,  $\bar{f}_{Cr} \lesssim 0.2$  and thus  $n \lesssim 4$ .

## V. Comparison - Theory vs Experiment

### A. Experimental Reflectance Measurements

The major objective of the modeling research has been to develop a physical model of a black Cr coating which can explain the observed spectral reflectance data. Two distinct types of experimental measurements have been made. In the principal series of experiments, the spectral hemispherical reflectance,  $R(\lambda)$ , has been measured over the wavelength interval,  $0.45 \mu\text{m} < \lambda < 2.5 \mu\text{m}$ , for black Cr films plated on smooth and rough Ni substrates. These measurements have also been made after the coatings have been thermally aged in air at various temperatures. In another experiment, a black Cr film was plated onto a steel substrate and was subsequently removed from the substrate by chemically etching the steel.<sup>23</sup> The stripped black Cr film was then placed, with the original substrate side down, onto a glass substrate. The original substrate side was grayish in color, indicating the presence of a high metal volume fraction on that side. The spectral reflectance of both sides of this stripped film was then measured.

The measured spectral reflectances of two black Cr films plated onto nickel from different baths and aged for various times at 450°C are shown in Figs. V-1 and V-2. The variation seen in  $R(\lambda)$  characteristics for these films is typical of that which is observed in practice and is probably a result of variation in coating microstructure produced by variations in plating process variables or in plating bath chemical concentrations. The coating in Fig. V-1 develops a "bump" or an interference peak at  $\lambda \approx 0.9 \mu\text{m}$  as thermal aging progresses and the position of the rapid reflectance rise or reflectance "edge" shifts to shorter wavelengths. It can be seen that a significant change in the nature of the  $R(\lambda)$  curve has occurred in the first 12h of aging, with the edge becoming significantly steeper. This is felt to be a result of the evolution of volatile materials trapped in the coating during the plating process. Zajac, Smith and Ignatiev<sup>26</sup> have reported the desorption of  $\text{H}_2$ ,  $\text{H}_2\text{O}$ ,  $\text{CO}$  and  $\text{CO}_2$  in coatings heated above 300°C.

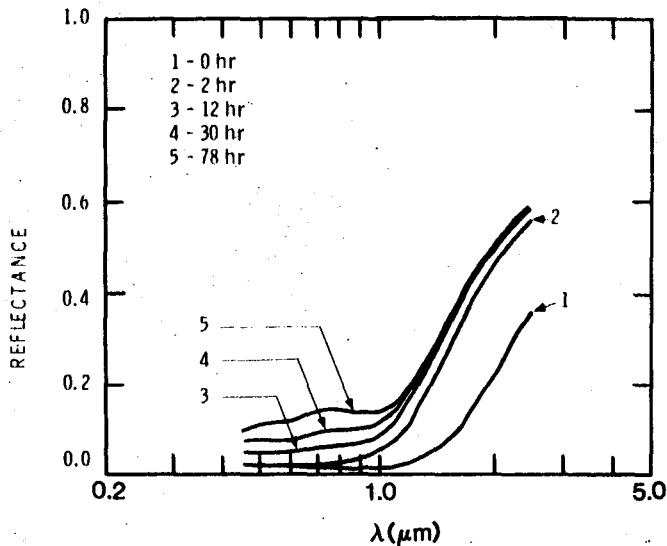


V-1 Experimental spectral reflectance  $R(\lambda)$  of a black Cr film aged in air at 450 C for various times as shown. This film develops an "interference" bump at  $\lambda \approx 0.9 \mu\text{m}$  as aging progresses.

The  $R(\lambda)$  characteristics shown in Fig. V-2 do not indicate the formation of a significant interference peak. Instead, the reflectance at short wavelengths appears to increase approximately uniformly as aging progresses. The thermal stability of the two coatings is also quite different. The solar averaged absorptance,  $\alpha_s$ , for the coating in Fig. V-1 changed from  $\alpha_s = 0.97$  to  $\alpha_s = 0.94$  after 46 h of aging while, for the coating in Fig. V-2, the initial  $\alpha_s = 0.96$  was reduced to  $\alpha_s = 0.85$  after only 30 h.

### B. Coating Structural Model

A structural model of a black Cr coating is required in order to calculate theoretical  $R(\lambda)$  characteristics using the procedure described in Sec. IV-E. The model is derived from the results of various microstructural investigations,

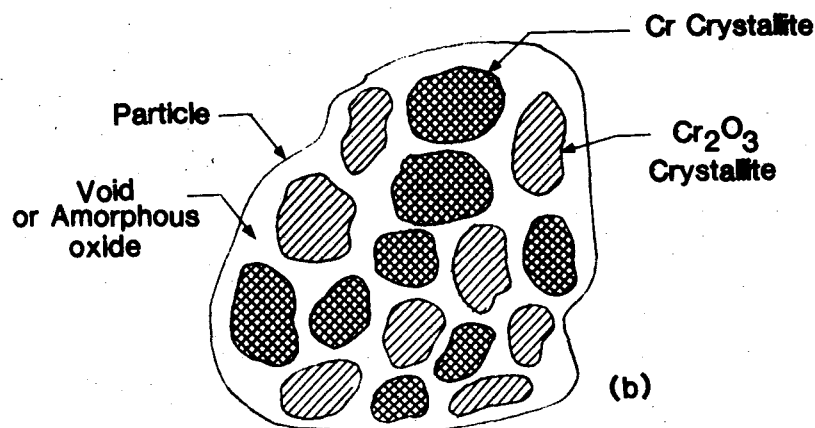
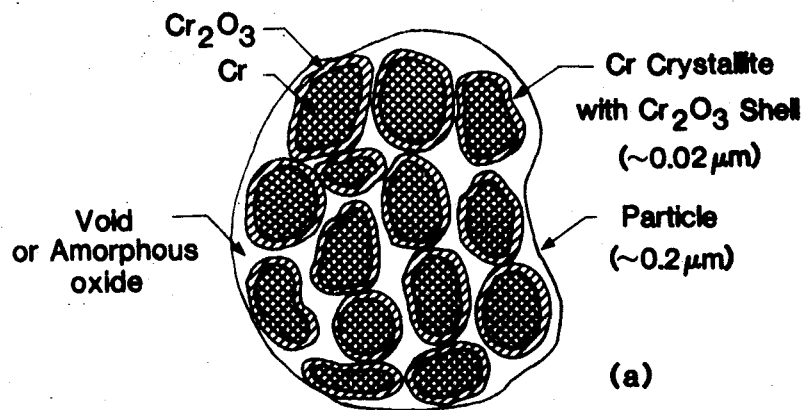


V-2 Experimental spectral reflectance  $R(\lambda)$  of a second black Cr film aged in air at 450 C. In this case the short wavelength reflectance increases as aging progresses but an "interference" bump does not develop.

as discussed in Sec. III-C, and from other measurements such as film areal density and thickness. The SEM and TEM studies discussed in Sec. III-B,C indicate that black Cr films are highly porous and contain a mixture of various Cr oxides and Cr metal in the form of small metallic crystallites. The detailed nature of the oxides is still unknown, but after a coating has been thermally aged for a relatively short time, the principal oxide observed by selected area electron diffraction is  $\text{Cr}_2\text{O}_3$ . For modeling purposes, we have elected to represent a black Cr coating as a mixture of Cr metal, crystalline  $\text{Cr}_2\text{O}_3$ , and void volume. The Cr metal and  $\text{Cr}_2\text{O}_3$  are assumed to be present at their bulk densities.

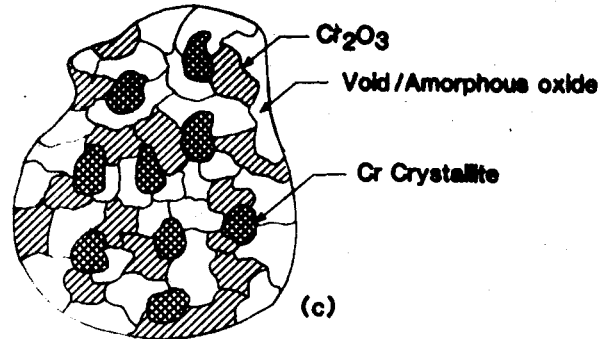
The major constituents of a black Cr film, as seen in SEM studies, are roughly spherical particles  $\sim 0.2 \mu\text{m}$  in diameter. Inside these particles are the Cr crystallites,  $\text{Cr}_2\text{O}_3$ , and probably additional void volume. This additional void volume may include non-dense amorphous Cr oxides of various types. For the purposes of this discussion, the term void represents a material with a real dielectric constant,  $\epsilon_m \approx 1$ . The nature of the distribution of the Cr and  $\text{Cr}_2\text{O}_3$  inside these particles is still not resolved. The Cr may be in the form of distinct

crystallites, each surrounded by a shell of  $\text{Cr}_2\text{O}_3$  as indicated schematically in Fig. V-3(a). Another possible model is that of an assembly of Cr and  $\text{Cr}_2\text{O}_3$  crystallite particles, as shown in Fig. V-3(b). Still another possibility is that of a distribution of Cr crystallites in a Bruggeman type matrix of  $\text{Cr}_2\text{O}_3$  and void, as shown in Fig. V-3(c). Still other hypothetical structures may be developed from combinations of these basic structures.



V-3:

- (a) Model structure for a black Cr "particle." In this structure, the particle is composed of a number of Cr crystallites, each surrounded by a shell of  $\text{Cr}_2\text{O}_3$ . The space between the crystallites might consist of a non-dense, amorphous oxide.
- (b) Alternate model structure consisting of crystallites of Cr and  $\text{Cr}_2\text{O}_3$  in a non-dense matrix.



V-3 (c) Distribution of Cr crystallites in a Bruggeman matrix of  $\text{Cr}_2\text{O}_3$  and void.

In modeling a coated sphere film (Fig. V-3(a)), the core dielectric constant,  $\epsilon_{\text{Cr}}$ , is replaced by the coated particle dielectric constant,  $\epsilon_{\text{CS}}$ , as given by Eq. (IV-32). In all our calculations, we have assumed that only spherical coated particles are present, so that the depolarizing factors  $L_i = 1/3$  for all  $i$ . Both Bruggeman and Maxwell-Garnett mixtures of void and coated particles have been used to calculate model  $R(\lambda)$  results. For coatings with both Cr and  $\text{Cr}_2\text{O}_3$  particles (Fig. V-3(b)), the MG dielectric constant, Eq. (IV-9), has been utilized with  $f_1 = f_{\text{Cr}}$  and  $f_2 = f_{\text{Cr}_2\text{O}_3}$ . For coatings of the type shown in Fig. V-3(c), Eq. (IV-31) was used to calculate the medium dielectric constant with  $\epsilon_{\text{C}} = \epsilon_{\text{Cr}_2\text{O}_3}$ ,  $\epsilon_{\text{m}} = 1$ , and  $f = f_{\text{Cr}_2\text{O}_3}$  in that equation. Then Eq. (IV-11) has been utilized with  $\epsilon_{\text{C}} = \epsilon_{\text{Cr}}$ , and  $f = f_{\text{Cr}}$ . Since plated films used in our studies typically had average thicknesses in the range  $\sim 0.2\text{-}0.5 \mu\text{m}$ , they appear to be composed of several layers of particles of the type shown in Fig. V-3. For the purpose of making reflectance calculations, we assume that the highly heterogeneous film can be replaced by a film which is made up of a number of slices, as shown in Fig. IV-14(a). In a thin slice at depth  $x$  it is assumed that the volume fractions of Cr,  $\text{Cr}_2\text{O}_3$ , and void are constant. This amounts to a "smearing" of the film in sections parallel to the surface plane such that the constituent concentrations in any section

have their average values for the depth of that section. If the average volume fractions of Cr, Cr<sub>2</sub>O<sub>3</sub>, and void at depth x are f<sub>Cr</sub>(x), f<sub>Cr<sub>2</sub>O<sub>3</sub></sub>(x) and f<sub>v</sub>(x) respectively, then, at any x,

$$f_{\text{Cr}}(x) + f_{\text{Cr}_2\text{O}_3}(x) + f_v(x) = 1 \quad (\text{V-1})$$

The coordinate x is measured from the front surface of the film with the substrate located at x = L. In the future, we shall refer to the average constituent volume fractions at depth x as just volume fractions to avoid confusion with averages taken over the whole film depth. In order to make connection with experimental Auger sputter profile results, we replace the fundamental volume fractions f<sub>Cr</sub>(x) and f<sub>Cr<sub>2</sub>O<sub>3</sub></sub>(x) with the total volume fraction f(x) and the relative volume fraction of Cr to Cr + Cr<sub>2</sub>O<sub>3</sub>, Ω(x). These new quantities are defined in terms of the original volume fractions by,

$$f(x) = f_{\text{Cr}}(x) + f_{\text{Cr}_2\text{O}_3}(x) \quad , \quad (\text{V-2})$$

and,

$$\Omega(x) = f_{\text{Cr}}(x) / [f_{\text{Cr}}(x) + f_{\text{Cr}_2\text{O}_3}(x)] \quad (\text{V-3})$$

The inverse relations are,

$$f_{\text{Cr}}(x) = \Omega(x)f(x) \quad , \quad (\text{V-4})$$

and,

$$f_{\text{Cr}_2\text{O}_3}(x) = [1 - \Omega(x)]f(x) \quad (\text{V-5})$$

Frequently, the average value of these various quantities is desired. The average of a quantity, f<sub>i</sub>(x) is defined via the relation,

$$\bar{f}_i = \frac{1}{L} \int_0^L f_i(x) dx \quad , \quad (V-6)$$

where L = film thickness.

Within this model, the average film density,  $\bar{\rho}$ , is given by,

$$\bar{\rho} = \rho_{Cr} \bar{f}_{Cr} + \rho_{Cr_2O_3} \bar{f}_{Cr_2O_3} \quad (V-7)$$

If both sides of Eq. (V-7) are multiplied by L, the densities can be interpreted as areal mass densities,  $\rho_s$  (gm/cm<sup>2</sup>). A number of measurements of  $\rho_s$  have been reported, as discussed in Sec. III-C. These experiments were all conducted on films stripped from Fe substrates and the results are, therefore, not necessarily typical of film deposited onto Ni substrates.<sup>3,26</sup> However, they do furnish a basis for performing initial calculations. We have used a value,  $\rho_s = 7 \times 10^{-5}$  g/cm<sup>2</sup>, typical of the lower range of thermally stable coatings, as discussed by Pettit, Sweet and Sowell.<sup>3</sup>

The coating thickness which should be utilized in calculations of this type is to some extent indeterminate. Coatings typically have a surface roughness variation on the order of a particle size, or about 0.2  $\mu$ m, and the thickness, as measured from SEM micrographs of stripped films, is typically in the range L  $\approx$  0.2-0.5  $\mu$ m. If  $\rho_{Cr}$  and  $\rho_{Cr_2O_3}$  have their measured bulk values, 7.14 and 5.22 g/cm<sup>3</sup> respectively, then Eq. (V-7) yields,

$$\rho_s/L = 7.14 \bar{f}_{Cr} + 5.22 \bar{f}_{Cr_2O_3} \quad (V-8)$$

For various values of  $L$  or  $\rho_s$ , Eq. (V-8) may be used to calculate the maximum possible values of  $\bar{f}_{Cr}$  or  $\bar{f}_{Cr_2O_3}$  by assuming that one or the other of these quantities is zero. Table V-1 shows the results of this calculation for  $\rho_s = 7 \times 10^{-5}$  g/cm<sup>2</sup> and  $L = 0.4$  and  $0.5 \mu\text{m}$ .

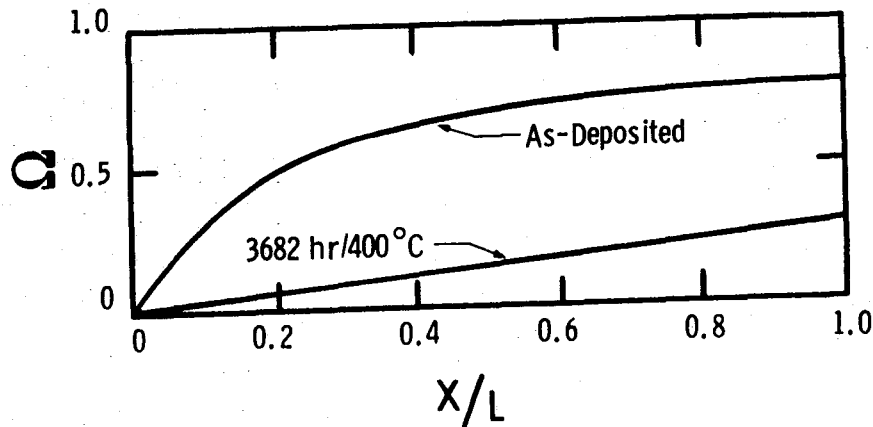
Table V-1. Maximum Possible Values of  $\bar{f}_{Cr}$  or  $\bar{f}_{Cr_2O_3}$  for  $L = 0.4 \mu\text{m}$  and  $0.5 \mu\text{m}$ , from Eq. (V-8).

$L(\mu\text{m})$	$\bar{f}_{Cr\text{-max}}$	$\bar{f}_{Cr_2O_3\text{-max}}$
0.4	0.25	0.34
0.5	0.20	0.27

The Auger data discussed in Sec. III-B indicate that as-deposited films are heavily oxidized, with  $\bar{\Omega} \lesssim 0.6$ . As the coating oxidizes, the areal density increases and possibly the film thickness increases as well. In light of these uncertainties, we have elected to assume that  $\bar{f} = \bar{f}_{Cr} + \bar{f}_{Cr_2O_3}$  is a fixed quantity and that  $L$  remains at its initial value as the coating ages. For a  $0.4 \mu\text{m}$  film, a value of  $\bar{f} = 0.30$  has been assumed and for a  $0.5 \mu\text{m}$  film, a value  $\bar{f} = 0.25$  has been used.

There is no direct experimental evidence which yields the functional form of  $f(x)$  directly. Films stripped from Fe substrates appear gray or metallic on the "substrate" side, indicating a large value of  $f_{Cr}(L)$ . The rough nature of a black Cr film suggests that  $f(0) \cong 0$ . We have used the power law form, Eq. (IV-43) for  $f$ . The requirement,  $f_{\text{max}} = f(L) < 1$ , can be used with Eq. (IV-43) to set the limit,  $n + 1 \leq 1/\bar{f}$ , where  $n =$  exponent in the power law relation. For  $\bar{f} = 0.30$ ,  $n_{\text{max}} = 2.3$  and for  $\bar{f} = 0.25$ ,  $n_{\text{max}} = 3.0$ . For baseline calculations, we have used  $n = 2$  when  $\bar{f} = 0.30$  and  $n = 3$  for  $\bar{f} = 0.25$ . Effects of varying  $n$  from these nominal values will be discussed in the next section.

The relative volume fraction of Cr,  $\Omega(x)$ , as given by Eq. (V-3) can be determined experimentally from Auger sputter profile data. This experimental determination has been discussed by Holloway, Shanker, Pettit and Sowell.<sup>28</sup> Some results derived from this work are shown in Fig. V-4. A number of assumptions



V-4 Relative volume fraction of Cr to  $(Cr + Cr_2O_3)$ ,  $Q(x)$  as obtained from Auger sputter profile data for an as-deposited film and for the same film aged for 3682 h at 400 C.

have to be made to derive the  $\Omega(x)$  relation from Auger Cr and O signal level vs sputter time data,<sup>69,70</sup> so these derived relations must be considered, at best, semiquantitative in nature. As-deposited films are typically characterized by a nonlinear  $\Omega(x)$  characteristic which can be described reasonably well by a function of the form,

$$\Omega(x) = \Omega_{\max} \left( 1 - e^{-x/x_0} \right) \quad , \quad (V-9)$$

where  $\Omega_{\max}$  and  $x_0$  are parameters.  $\bar{\Omega}$  is related to  $\Omega_{\max}$  and  $x_0$  by,

$$\bar{\Omega} = \Omega_{\max} \left[ 1 - (x_0/L) \left( 1 - e^{-L/x_0} \right) \right] \quad (V-10)$$

The parameters,  $\Omega_{\max}$  and  $x_0$  are chosen in an iterative fashion or by nonlinear least squares techniques to yield a good fit between Eq. (V-9) and a measured  $\Omega(x)$  characteristic, such as the one shown in Fig. V-4 for an as-deposited film.

After thermal aging, the  $\Omega(x)$  characteristic becomes linear and can be described by a function of the form,

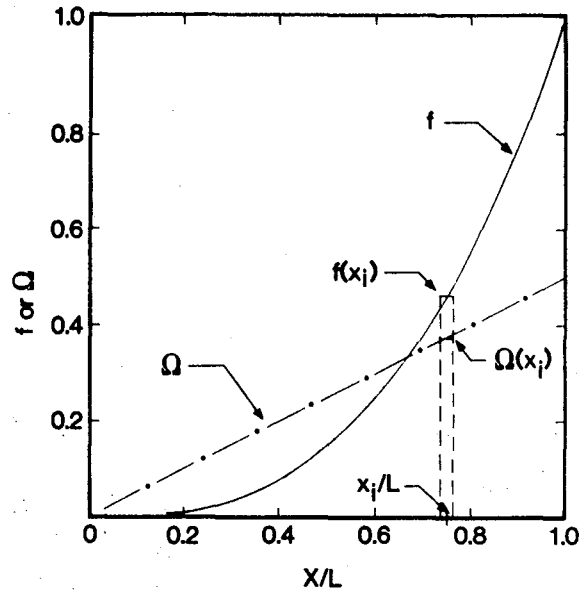
$$\Omega(x) = 2\bar{\Omega}x/L \quad . \quad (V-11)$$

As will be seen in the next section, for  $\bar{\Omega} = 0.5$ , use of either Eq. (V-11) or Eq. (V-9) in a reflectance calculation yields essentially the same result, showing that Eq. (V-11) is adequate for calculating  $R(\lambda)$  at all times.

The multilayer reflectance calculation procedure described in Sec. IV-F is used to calculate  $R(\lambda)$ . In this model, we typically have used 95 layers, although the results are not significantly altered by using only 50 layers. A model of a with  $f \sim x^3$ ,  $\bar{f} = 0.25$  and  $\bar{\Omega} = 0.25$  is shown in Fig. V-5. In the  $i^{\text{th}}$  film slice,  $f(x)$  and  $\Omega(x)$  are constant with the values  $f(x_i)$  and  $\Omega(x_i)$  respectively as shown in Fig. IV-5. The coordinate  $x_i$  is given by,  $x_i = (i - 1/2)(L/N)$ , where  $N =$  number of layers. After the spectral reflectance is calculated, the solar averaged absorptance,  $\alpha_s$ , is found by averaging the spectral absorptance  $A(\lambda) = 1 - R(\lambda)$  over an airmass 1.5 solar spectrum  $\Phi(\lambda)$ ,

$$\alpha_s = \frac{\int_0^{\infty} \Phi(\lambda) [1 - R(\lambda)] d\lambda}{\int_0^{\infty} \Phi(\lambda) d\lambda} \quad (V-12)$$

The temperature dependent normal emittance  $\epsilon_N(T)$  is found by averaging  $A(\lambda)$  over the Planck blackbody distribution function,



V-5 Model film structure used for reflectance calculations with  $f(x) \propto x^3$  and  $\Omega(x)$  linear. The film is broken up into discrete layers as discussed in Sec. IV-E. The  $i^{\text{th}}$  film slice is assumed to have uniform properties  $f(x_i)$  and  $\Omega(x_i)$ .

$$\epsilon_N(T) = \frac{\int_0^{\infty} g(T, \lambda) [1 - R(\lambda)] d\lambda}{\int_0^{\infty} g(T, \lambda) d\lambda} \quad (\text{V-13})$$

where  $g(T, \lambda)$  is defined by,

$$g(T, \lambda) = (2\pi c^2 h / \lambda^5) \left[ \exp\left(\frac{hc}{\lambda k_B T}\right) - 1 \right]^{-1}, \quad (\text{V-14})$$

where  $c$  = speed of light,  $h$  = Planck's constant, and  $k_B$  = Boltzman's constant.

These calculations were done in practice by performing 20 point weighted averages of  $[1 - R(\lambda)]$  as described by Lind, Pettit and Masterson.<sup>71</sup>

The relationship between the hemispherical emittance  $\epsilon_H(T)$  and the normal emittance depends on the nature of the emitting surface. Sievers gives the relation,  $\epsilon_H(T) = (4/3)\epsilon_N(T)$  for good conductors ( $\epsilon_N \rightarrow 0$ ).<sup>6</sup> Through use of the simple "Drude" theory of metals, the ratio  $\epsilon_H/\epsilon_N$  can be calculated as a function of  $\epsilon_N$ .<sup>72</sup> For  $\epsilon_N \approx 0.1$ , this ratio has the value,  $\epsilon_H/\epsilon_N \approx 1.2$ . For the purpose of making approximate calculations for black Cr-metal substrate systems, we have used a factor of 1.2 to convert  $\epsilon_N$  to  $\epsilon_H$ .

### C. Calculated Results

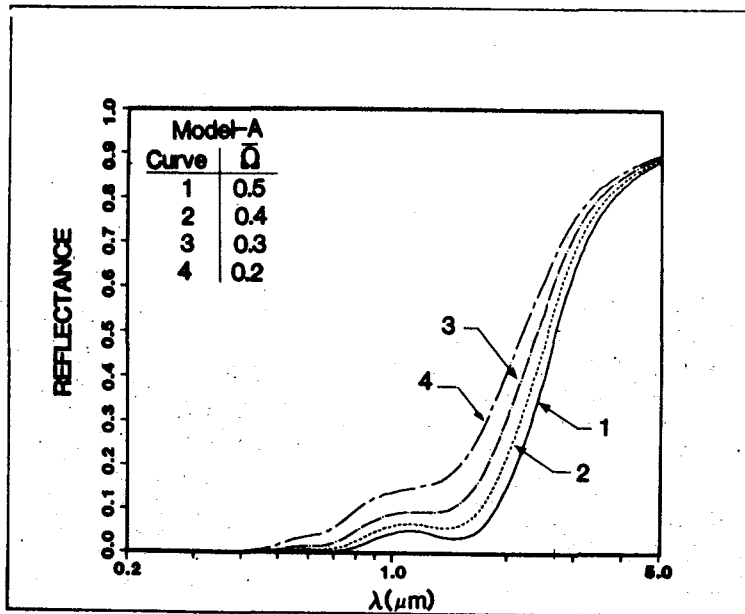
1. Verification of Computer Code: The computer code written for calculating the normal reflectance of a multilayer stack was checked by solving a number of test problems for which analytical solutions exist. As a further check, some of the results reported by Granqvist and Hunderi<sup>38</sup> were duplicated. In Fig. 3 of Ref. 38, results are presented for the reflectance of a uniform 1  $\mu\text{m}$  thick Maxwell-Garnett layer of spherical chrome particles in an air matrix on both Cu and Ni substrates. The dielectric function used was Eq. (IV-16) with  $L = 1/3$  and the Cr, Ni and Cu optical data were taken from the same sources. Our results agreed quite well with those in Ref. 38 for both types of substrates and over the wavelength interval,  $0.3 \mu\text{m} < \lambda < 5 \mu\text{m}$ . The maximum deviations between the two calculations occurred at the longer wavelengths and were  $< 10\%$ . The RMS deviation was  $\sim 2\%$ . These deviations are probably a result of variations in derived values of the real and imaginary parts of the index of refraction,  $n(\lambda)$  and  $k(\lambda)$ , for the various materials, as found from the primary reference sources. For Cu,  $n(\lambda)$  and  $k(\lambda)$  were obtained from the AIP Handbook.<sup>73</sup> A calculation of  $R(\lambda)$  for bare Cu reproduced the Granqvist and Hunderi result to within  $\sim 5\%$  at wavelengths in the 0.3-5  $\mu\text{m}$  range. The calculated reflectance of bare Ni also agreed well with the calculated results in Ref. 38 and agreed very closely with our measurements of the reflectance of bright Ni in the wavelength range 0.35-2.5  $\mu\text{m}$ .

2. Reflectance of Black Cr Films on Ni-MG Model: In this section, calculated  $R(\lambda)$  results are presented for two model black Cr films on Ni substrates. The Maxwell-Garnett dielectric function for spherical inclusions, Eq. (IV-11) with  $L = 1/3$ , has been used together with the coated sphere dielectric constant from Eq. (IV-32). The particle cores are assumed to be metallic Cr and the coatings  $\text{Cr}_2\text{O}_3$ . Table V-2 shows the parameters used in the two calculations.

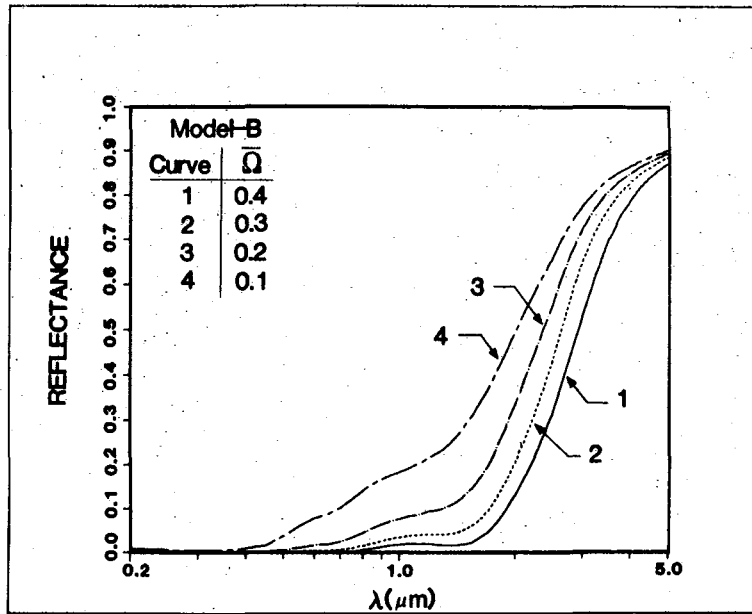
Table V-2. Parameters for Model Reflectance Calculations

Parameter	Model-A	Model-B
Film thickness- $L(\mu\text{m})$	0.40	0.50
Avg fill factor- $\bar{f}$	0.30	0.25
$f(x)$ power law- $n$	2	3
$f(L)$	0.90	1.00
$\Omega$ function	linear	linear

Fig. V-6 shows results for Model-A and Fig. V-7 for Model B.  $\Omega(x)$  has been chosen as a linear function and the average value  $\bar{\Omega}$  is shown as a parameter. As  $\bar{\Omega}$  increases, the "edge" or position of steep rise in the reflectance curve moves toward shorter wavelengths and, at small values of  $\bar{\Omega}$ , the short wavelength reflectance increases appreciably. It is only when the reflectance for  $\lambda < 1 \mu\text{m}$  assumes an appreciable magnitude that the solar averaged absorptance,  $\alpha_s$ , deviates appreciably from its value at large values of  $\bar{\Omega}$ . Fig. V-8 shows the predicted variation of  $\alpha_s$  with the quantity  $(1 - \bar{\Omega})$  for the two models (curves A and B), together with some experimental data for thermally stable (curve S) and unstable (curve U) black Cr.<sup>28</sup> The quantity  $(1 - \bar{\Omega})$  represents the relative volume fraction of  $\text{Cr}_2\text{O}_3$  in the coating, i.e., the fraction of material per unit volume in the coating which is  $\text{Cr}_2\text{O}_3$ . Experimentally, this quantity was derived from Auger sputter profile data.<sup>28</sup>

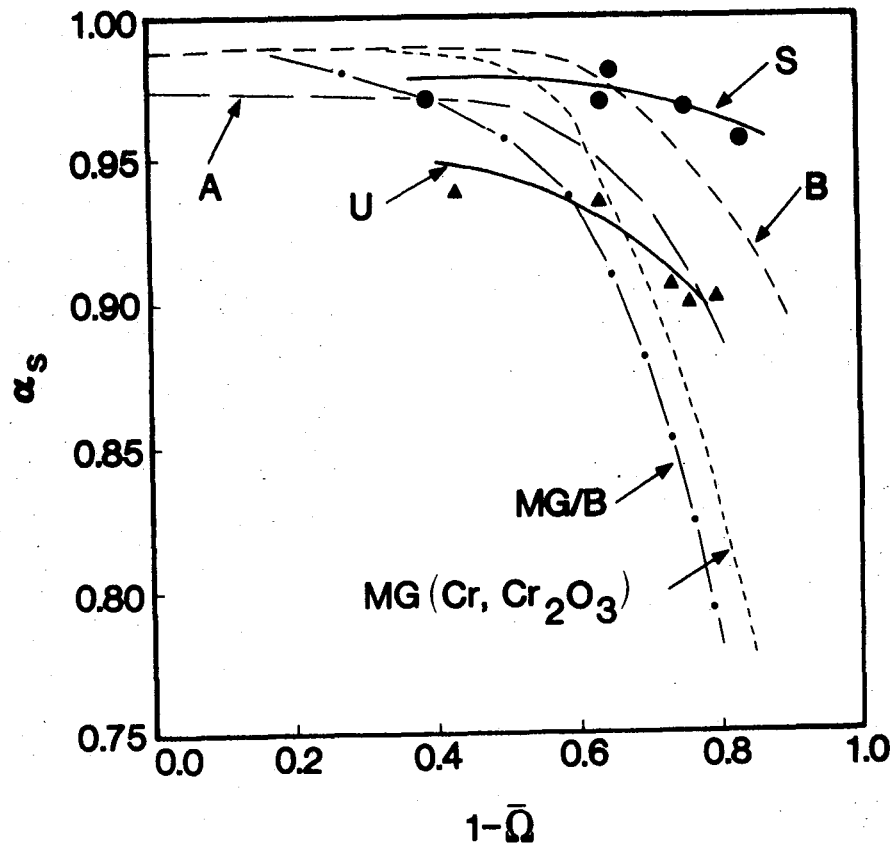


V-6 Spectral reflectance of a black Cr coating with parameters of model-A, Table V-2, for  $\bar{\Omega} = 0.5, 0.4, 0.3$  and  $0.2$ .



V-7 Calculated spectral reflectance of a black Cr coating with parameters of Model-B, Table V-2, for  $\bar{\Omega} = 0.4, 0.3, 0.2$  and  $0.1$ .

Both the experimental and the theoretical curves in Fig. V-8 show the same general kind of behavior:  $\alpha_s$  remains relatively constant until the relative volume fraction of  $\text{Cr}_2\text{O}_3$  is  $\geq 70\%$ . Then  $\alpha_s$  starts to decrease rapidly with additional oxide formation. The theoretical dependence of  $\alpha_s$  on  $(1 - \bar{\Omega})$  represents one of the most significant predictions derived from the MG theory.

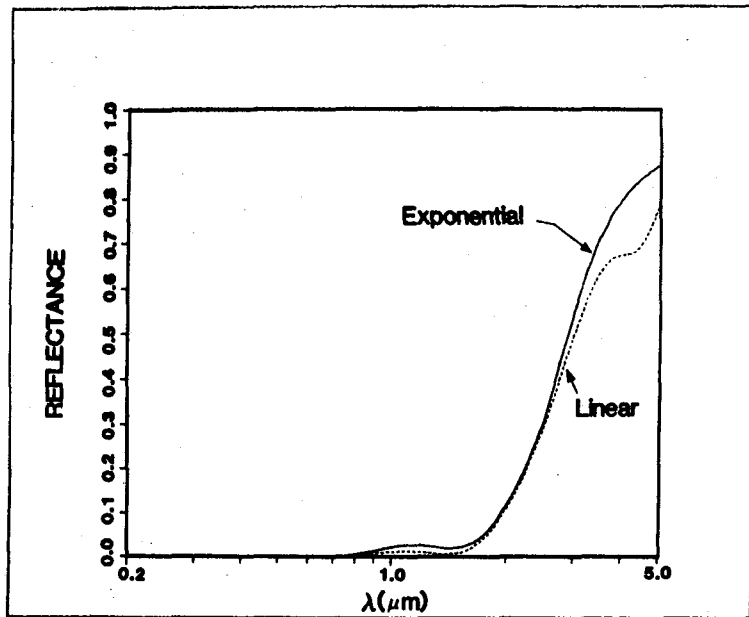


V-8 Solar absorptance vs relative volume fraction of  $\text{Cr}_2\text{O}_3$ ,  $1 - \bar{\Omega}$ . Curves S (solid circles) and U (solid triangles) represent experimental data for stable and unstable films respectively. Curves A and B are results calculated from Models A and B. Curve MG/B is a result calculated from the MG model with a Bruggeman  $\text{Cr}_2\text{O}_3$ /void matrix. Curve MG(Cr,  $\text{Cr}_2\text{O}_3$ ) is a result calculated assuming an MG mixture of Cr and  $\text{Cr}_2\text{O}_3$  in an air matrix.

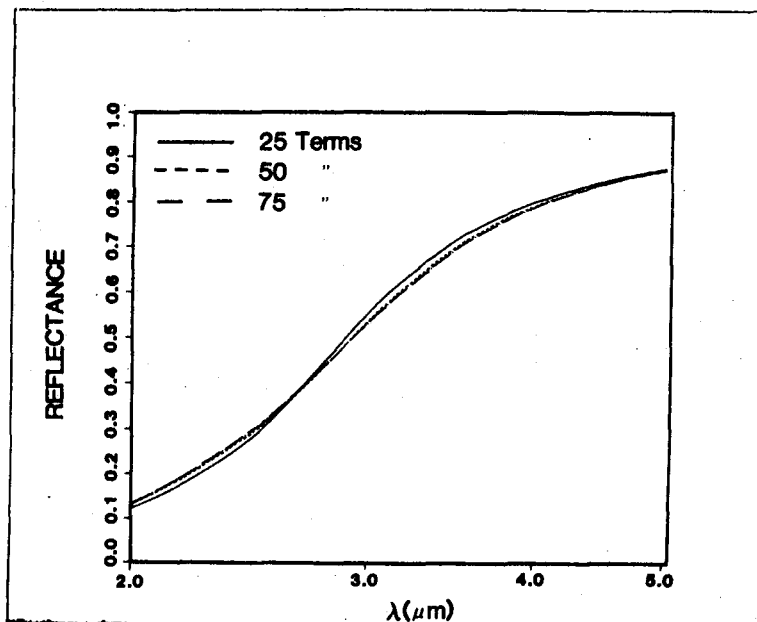
For values of  $\bar{\Omega} \gtrsim 0.5$ , the  $R(\lambda)$  curve is not too sensitive to the exact form of  $\Omega(x)$ . A comparison of  $R(\lambda)$  behavior for a linear  $\Omega(x)$  function and a saturating exponential  $\Omega(x)$  function, Eq. (V-9), is shown in Fig. V-9 for the Model B case. In the exponential case,  $\Omega_{\max} = 0.76$ ,  $\bar{\Omega} = 0.57$ , and  $x_0/L = 0.26$  while for the linear case,  $\bar{\Omega} = 0.5$ . The bump in the  $R(\lambda)$  curve at  $\lambda \approx 4 \mu\text{m}$  for the linear  $\Omega(x)$  case is a consequence of  $f_{\text{Cr}}(x) \rightarrow 1$  as  $x \rightarrow L$  in the Model B case, with  $\bar{\Omega} = 0.5$ . This is probably not physically meaningful because a 100% Cr volume fraction could probably not be achieved in practice. If the  $f(x) \sim x^3$  distribution is truncated at  $f_{\max} = 0.8$ , the bump is removed but  $R(\lambda)$  for  $\lambda \lesssim 3 \mu\text{m}$  is unchanged. The solar averaged absorptances,  $\alpha_s = 0.981$  for the exponential  $\Omega$  function and  $\alpha_s = 0.986$  for the linear  $\Omega$  function, are essentially identical.

The effect on  $R(\lambda)$  of using a variable number of layers in the multilayer reflectance calculation is shown in the Model B calculation of Fig. V-10 for the case in which  $\bar{\Omega} = 0.4$ . In this figure, results are shown for 25, 50 and 75 layers. The 50 and 75 layer cases produce essentially identical results while the 25 layer case indicates a small deviation. In all of the calculated results reported here, 95 layers have been used; adding more layers does not improve the accuracy of the calculation.

3. Effect of Variation of Model Parameters: Within the framework of the Maxwell-Garnett dielectric function-continuously graded power law Cr concentration model, there are three fundamental parameters which determine the nature of the spectral reflectance. These parameters are: the coating thickness,  $L$ ; the power law exponent,  $n$  from Eq. (IV-42); and the average material volume fraction,  $\bar{f}$  from Eq. (V-6). A region in  $\{n - L - \bar{f}\}$  parameter space can be found such that the calculated  $R(\lambda)$  characteristics are in good agreement with experiment but the parameters cannot be uniquely determined. Various experimental results do, however, impose some limits on the magnitudes of these parameters, as discussed

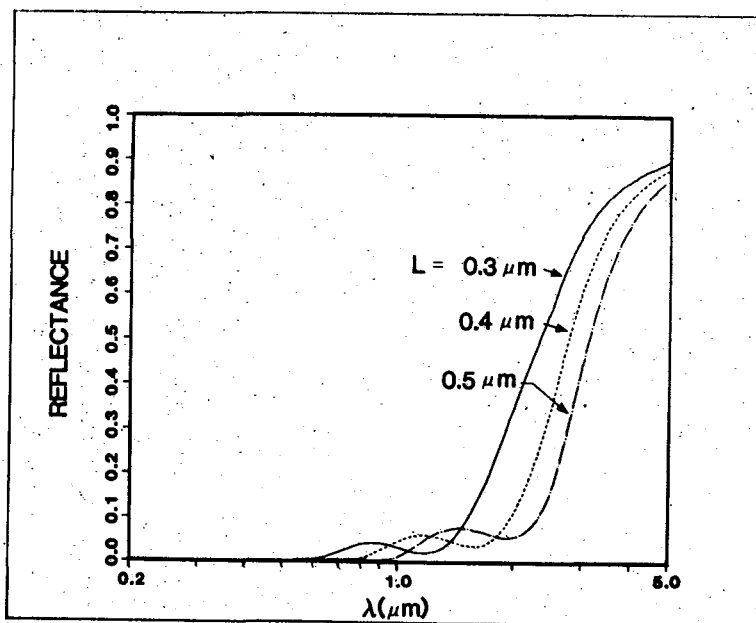


V-9 Dependence of the calculated spectral reflectance on the assumed initial form of  $\Omega(x)$ . Curve labeled exponential (solid line) was calculated using Eq. (V-9) for  $\Omega(x) = 0.76$  with  $\Omega_{\text{max}}$  and  $x_0/L = 0.26$ . Curve labeled linear (dashed line) was calculated using Eq. (V-11) with  $\Omega = 0.5$ .



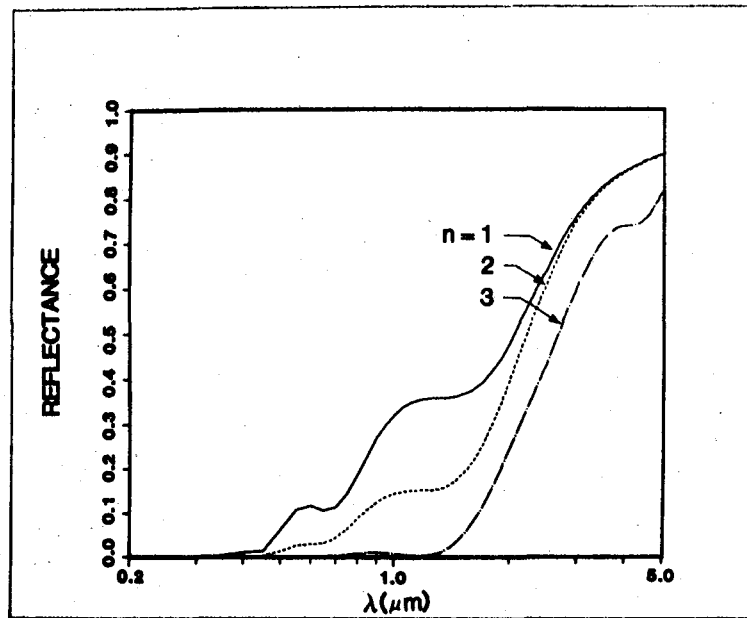
V-10. Effect on calculated  $R(\lambda)$  of a variable number of layers for a Model-A film. Results are shown for calculations with 25, 50 and 75 terms.

in the preceding section. We shall now examine the effect of individual variations of these parameters on  $R(\lambda)$  and then consider the effects of joint variations. As an aid in making this examination, we define (following Granqvist and Hunderi<sup>38</sup>) the cutoff wavelength,  $\lambda_c$  as the wavelength at which the reflectance is equal to 50%, i.e.,  $R(\lambda_c) = 0.5$ . In all of the following calculations, the  $\Omega$  function was defined as,  $\Omega(x) = 1$ , although the results are not changed much if Eq. (V-11) with  $\bar{\Omega} = 0.5$  is used for  $\Omega(x)$ . Fig. V-11 shows the effect of varying coating thickness with  $n$  and  $\bar{f}$  held constant. In this calculation,  $n = 2$ ,  $\bar{f} = 3$  and  $L = 0.3, 0.4,$  and  $0.5 \mu\text{m}$ . As  $L$  increases it can be seen that  $\lambda_c$  increases. This effect was previously demonstrated by Granqvist and Hunderi for uniform coatings ( $n = 0$ ) on Cu substrates with  $\bar{f} = 0.1$ .<sup>39</sup>

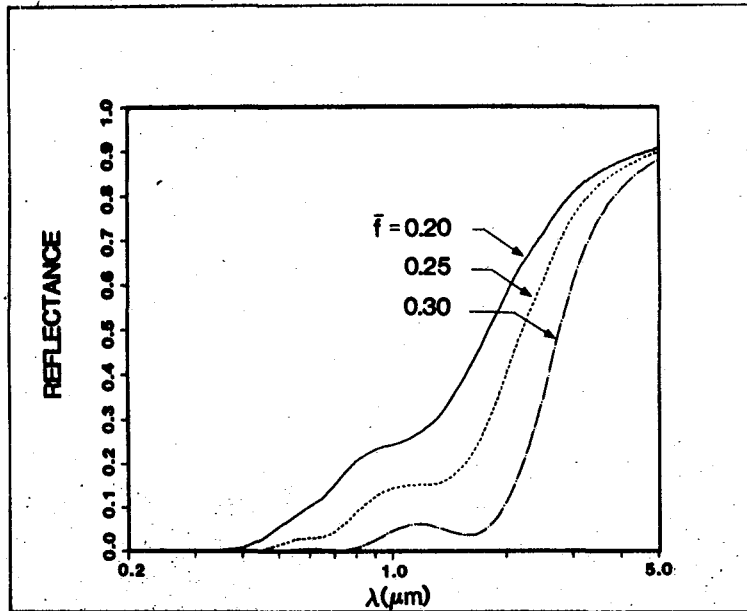


V-11 Effect of variable coating thickness on film reflectance. As  $L$  increases,  $\lambda_c$  increases. Parameters in the calculation are  $n = 2$ ,  $f = 0.3$ ,  $\bar{\Omega} = 1.0$ .

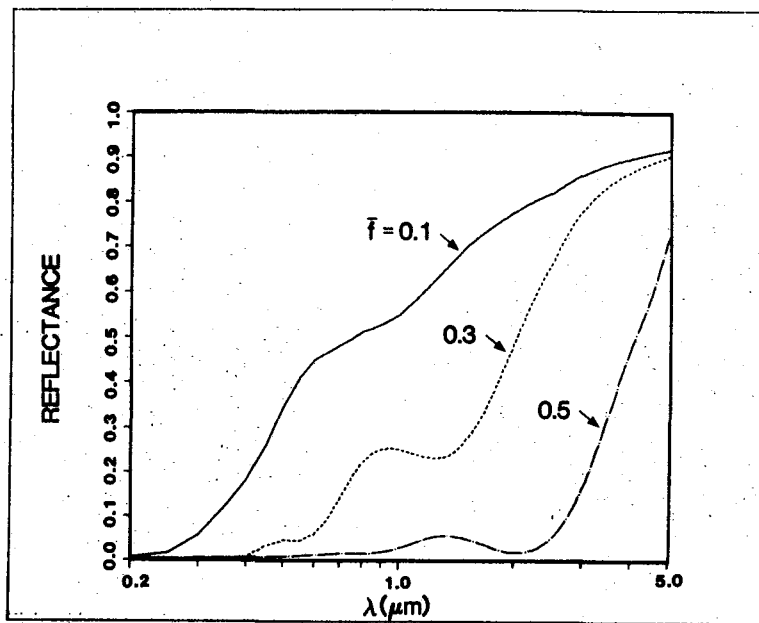
The effect of varying  $n$  with  $L$  and  $\bar{f}$  held constant is shown in Fig. V-12. In this case,  $L = 0.4 \mu\text{m}$ ,  $\bar{f} = 0.25$ , and  $n = 1, 2$  or  $3$ . As  $n$  increases,  $\lambda_c$  again increases and the reflectance for  $\lambda < \lambda_c$  decreases appreciably. The effect of varying  $\bar{f}$  with fixed  $L$  and  $n$  is shown in Fig. V-13. In this calculation,  $L = 0.4 \mu\text{m}$ ,  $n = 2$  and  $\bar{f} = 0.2, 0.25$  and  $0.3$ . As  $\bar{f}$  increases,  $\lambda_c$  moves to longer wavelengths and the short wavelength reflectance decreases. Comparing Fig. V-12 and Fig. V-13, it can be seen that the effect on  $R(\lambda)$  of increasing either  $\bar{f}$  or  $n$  is qualitatively similar. Fig. V-14 indicates the effect of increasing  $\bar{f}$  for a coating with  $L = 0.3 \mu\text{m}$  and a linear grade,  $n = 1$ . In this case, the short wavelength reflectance stays large until  $\bar{f}$  becomes quite large.



V-12 Effect of variable grading power law on film reflectance. As  $n$  increases,  $\lambda_c$  increases. Parameters used in the calculation are  $L = 0.4 \mu\text{m}$ ,  $f = 0.25$ ,  $\frac{\lambda_c}{\Omega} = 1.0$ .



V-13 Effect of variable average fill factor on film reflectance. As  $\bar{f}$  increases,  $\lambda_C$  increases. Parameters used in the calculation are  $L = 0.4 \mu\text{m}$ ,  $n = 2$ , and  $\frac{\lambda_C}{\lambda_0} = 1.0$ .



V-14 Effect of increasing  $\bar{f}$  for a coating with a linear grade,  $n = 1$  and  $L = 0.3 \mu\text{m}$ .



From the above discussion, it is evident that  $\lambda_c$  can be increased by increasing either  $L$ ,  $n$  or  $\bar{f}$ . However, an examination of Figs. V-11 through V-14 indicates that only in certain cases does the reflectance remain small for  $\lambda < \lambda_c$ , then increase abruptly near  $\lambda_c$ , and approach  $\approx 0.9$  for  $\lambda > \lambda_c$ . These cases correspond to situations in which  $f_{\max} = (n + 1)\bar{f}$  is large,  $f_{\max} \gtrsim 0.9$ .

A diagram of  $n, L, \bar{f}$  parameter space is shown in Fig. V-15. The surface with  $\bar{f} = 1/(n + 1)$  is that for which  $f(L) = 1$  while that for  $\bar{f} = 0.9/(n + 1)$  corresponds to  $f(L) = 0.9$ . If  $f(L)$  falls within these limits, the reflectance for  $\lambda < \lambda_c$  is generally small. If the wavelength and parameter dependence of the reflectance is represented by the notation  $R(\lambda|n, L, \bar{f})$ , then the equation,

$$R(\lambda_c|n, L, \bar{f}) = 0.5 \quad (V-15)$$

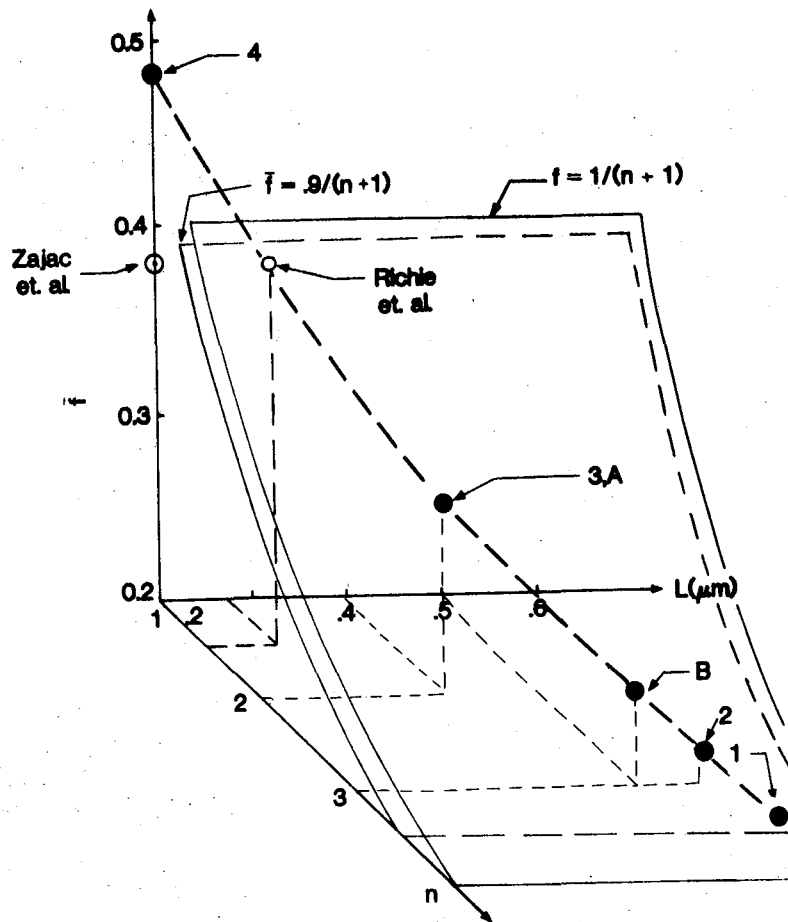
defines a surface in  $n, L, \bar{f}$  parameter space, for a given value of  $\lambda_c$ . The portion of this surface contained between the surfaces  $\bar{f} = 1/(n + 1)$  and  $\bar{f} = 0.9/(n + 1)$  in Fig. V-15 represents the region in parameter space in which the cutoff wavelength =  $\lambda_c$  and  $R(\lambda < \lambda_c)$  is small. The dashed line in Fig. V-15 represents, approximately, a line on the surface defined by Eq. (V-15) for  $\lambda_c \approx 3 \mu\text{m}$ . The locations of the models designated A and B are shown on this line. The line can be described, in an approximate way, by the parametric equations,

$$\bar{f} = 0.95/(n + 1) \quad (V-16)$$

$$n/L \approx 5$$

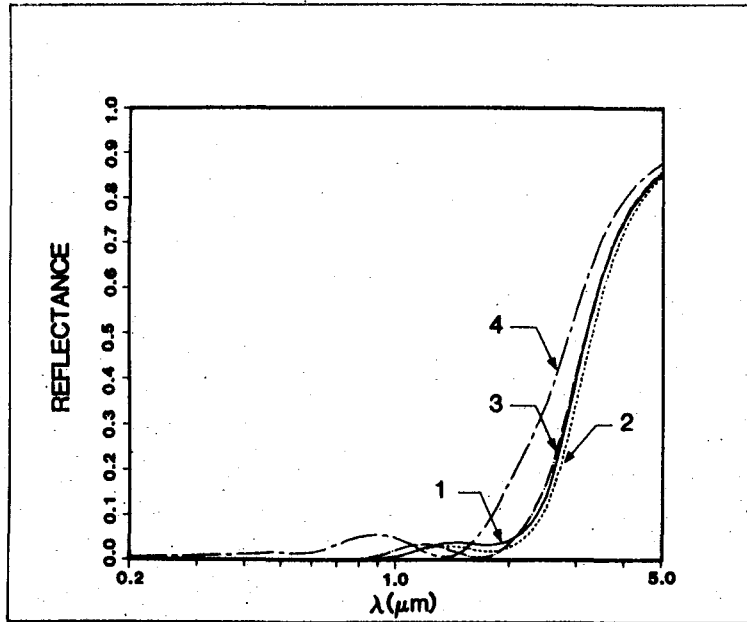
A set of  $R(\lambda|n, L, \bar{f})$  calculations using parameters determined from Eq. (V-16) is shown in Fig. V-16. The four sets of parameters used are designated 1-4 and the coordinates of these points are indicated in Fig. V-15. The wavelength variation in  $R$  is virtually identical for cases 1-3, while case 4 shows a small deviation, with  $\lambda_c < 3 \mu\text{m}$ .

The functions  $R(\lambda|n,L,\bar{f})$  can also be characterized in an approximate way by the two usual parameters,  $\alpha_S$  and  $\epsilon_N(300^\circ\text{C})$ . For cases 1-3 in Fig. V-16,  $\alpha_S = 0.99$  and  $\epsilon_N(300\text{ C}) = 0.11-0.14$ . For case 4,  $\alpha_S = 0.96$  and  $\epsilon_N(300^\circ\text{C}) = 0.11$ . For sets of parameters with  $n$  and  $\bar{f}$  specified by the first of Eqs. (V-16) but with  $L > n/5$ ,  $\lambda_c$  will shift to longer wavelengths, with a consequent increase in



V-15 Surfaces in  $n$ - $L$ - $\bar{f}$  parameter space which bound a volume in the space for which  $R(\lambda)$  is small for  $\lambda < \lambda_c$ . The upper sheet is defined by  $f = 1/(n + 1)$  and the lower sheet by  $f = 0.9/(n + 1)$ . The dashed line corresponds to  $\lambda_c \approx 3.0 \mu\text{m}$ . The parametric locations of models A and B are indicated. The numbers 1-4 represent sets of parameters for the  $R(\lambda)$  calculations shown in Fig. V-16. The approximate  $(n, L, f)$  coordinates for calculations by Zajac, et al.<sup>26</sup> and Richie, et al.<sup>25</sup> are also shown.

$\epsilon_N(300^\circ\text{C})$ . For  $L < n/5$ ,  $\lambda_c$  shifts to shorter wavelengths and both  $\alpha_s$  and  $\epsilon_N(300\text{ C})$  decrease.

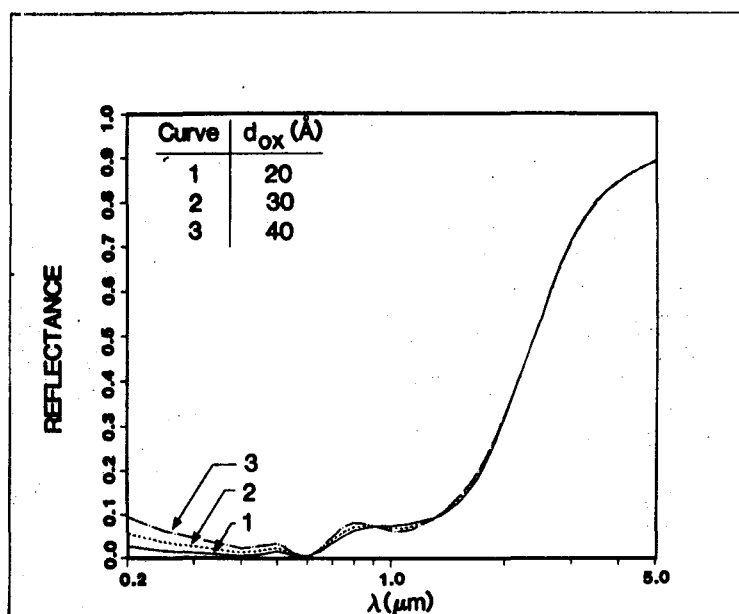


V-16 Spectral reflectance of black Cr films with  $(n, L, \bar{f})$  coordinates as indicated in Fig. V-15.

Coordinates of sets of parameters used in two reflectance calculations reported in the literature are also shown in Fig. V-15.<sup>25,26</sup> The calculation of Zajac, et al. was performed for three discrete layers of elliptical particles with  $\bar{f} = 0.38$ ,  $L = 0.2\ \mu\text{m}$ , and an approximate linear grade ( $n = 1$ ).  $\Omega(x)$  was also approximately linear with  $\bar{\Omega} \approx 0.7$ . Although the conditions for this calculation are not the same as for our calculations, the point in parameter space lies close to that predicted by Eqs. (V-16). The presence of highly eccentric particles results in shifting  $\lambda_c$  to longer wavelengths in their calculation. The calculation of Richie, et al. also involves elliptical particles and utilizes the McPhedran and McKenzie SC dielectric function. Their approximate parameters are  $\bar{f} = 0.4$ ,

$L = 0.28 \mu\text{m}$ ,  $n \approx 1.5$ . Again, this set of parameters is approximately that given by Eqs. (V-16). Thus there seems to be a tendency for different investigators to use parameter sets located close to the dashed line in Fig. V-15 when calculating spectral reflectance curves of unaged black Cr.

One additional feature which can be added to the basic Maxwell-Garnett graded layer model is the presence of a front surface oxide layer. Fig. V-17 shows the result of a calculation using model-A with  $\bar{\Omega} = 0.3$  and front surface  $\text{Cr}_2\text{O}_3$  layers of 20, 30 and 40Å. The main effect of the front surface oxide is to increase the short wavelength reflectance. This is similar to the increase in the short wavelength reflectance shown in the experimental  $R(\lambda)$  curve in Fig. V-2. Thus it is possible to explain this type of data by postulating the growth of a relatively thin uniform oxide layer on the film.

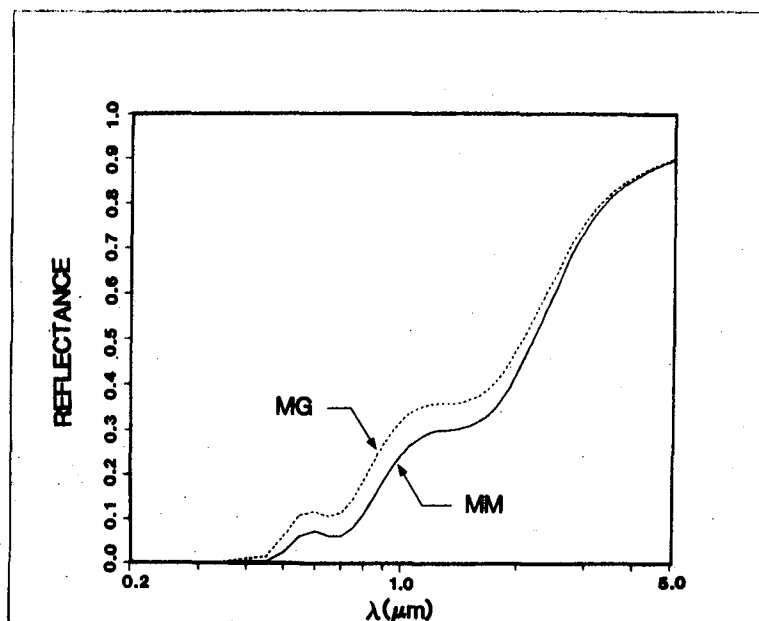


V-17 Effect of including a uniform front surface in the model film structure with a thickness  $d_{\text{ox}}$  as indicated on the figure. Other parameters are  $n = 2$ ,  $L = 0.4 \mu\text{m}$ ,  $f = 0.3$ ,  $\bar{\Omega} = 0.3$ .

4. Effect of Using Alternate Dielectric Functions: All of the calculations reported above were made using the basic Maxwell-Garnett (MG) dielectric function with spherical particles, Eq. (IV-11) with  $L = 1/3$ . In this section we examine the effect of employing alternate model dielectric functions in these calculations.

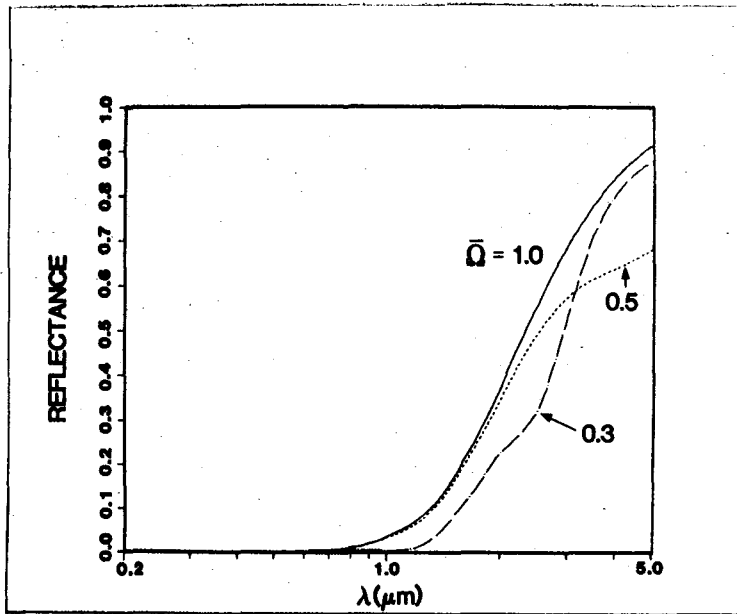
The McPhedran and McKenzie (MM) theory described briefly in Sec. IV-A gives the static ( $\lambda = \infty$ ) dielectric constant for a simple cubic (SC) array of spheres. Since it includes multipole effects, as compared to the MG theory which only includes dipole effects, presumably it will be more accurate at high volume fractions. The  $M = 4$  version of the MM SC theory dielectric function, Eqs. (IV-19) and (IV-20), is valid for  $0 < f < 0.524$ , where the upper limit is the volume fraction at which the spheres in a simple cubic lattice start to touch each other. It is not clear how the MM dielectric function should be extended to higher volume fractions. The results of a reflectance calculation using both the MM SC and MG theories for a linearly graded film with  $\bar{f} = 0.25$  and  $f_{\max} = 0.5$  is shown in Fig. V-18. The MG theory predicts a higher reflectance at all wavelengths, with the maximum percentage deviation,  $\sim 25\%$ , occurring at  $\lambda \approx 1.2 \mu\text{m}$ . Both curves do, however, have the same general shape. For the MG case,  $\alpha_s = 0.80$  and for the MM case,  $\alpha_s = 0.85$ . From this, and other calculations, it can be concluded the MM and MG dielectric functions produce observable but not marked differences in  $R(\lambda)$ .

The Bruggeman dielectric function, Eq. (IV-31), is symmetrical with respect to the dielectric constants of host and inclusion, and it applies at all volume fractions. However, the studies of coating microstructure discussed in Sec. III-B tend to indicate that black Cr films are not a Bruggeman type mixture of Cr/Cr<sub>2</sub>O<sub>3</sub> particles and air. Several calculations were performed using the spherical particle Bruggeman dielectric function Eq. (IV-31) with  $\epsilon_m = 1$  and  $\epsilon_c = \epsilon_{\text{CS}}$ , as

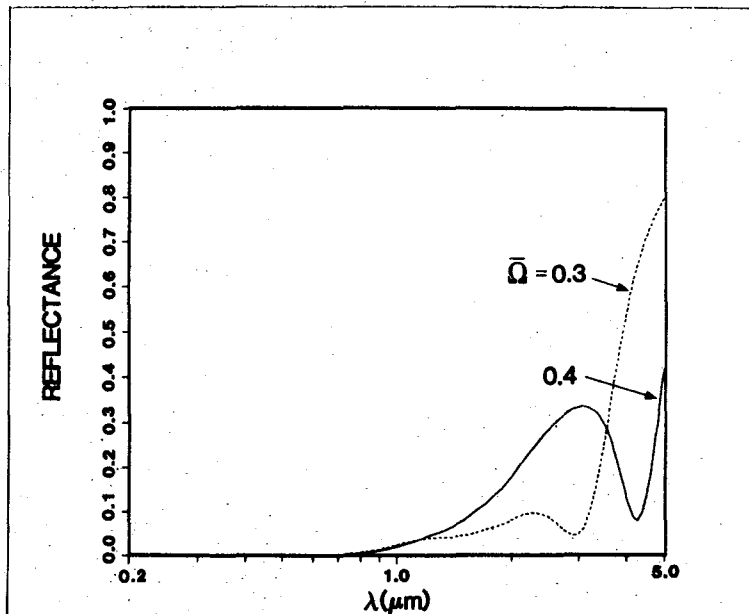


V-18 Comparison of the reflectance of a model black Cr film as calculated with the Maxwell-Garnett (MG) theory and the McPhedran, McKinzie (MM) simple cubic array theory. The calculation was performed for a linearly graded film ( $n = 1$ ) with  $f = 0.25$  and  $f_{\max} = 0.5$ .

given by Eq. (IV-32). Fig. V-19 shows the result of a calculation with  $n = 3$ ,  $\bar{f} = 0.2$ , and  $L = 0.4 \mu\text{m}$  for three values of  $\bar{\Omega}$ . The  $\bar{\Omega} = 1$  result (no oxide coating) shows that the Bruggeman dielectric function can yield results which are in good agreement with experimental  $R(\lambda)$  results for as-deposited films. However, as  $\bar{\Omega}$  decreases, the cutoff wavelength increases, as does  $\alpha_g$ . Fig. V-20 shows the results of a calculation in which  $n = 3$ ,  $\bar{f} = 0.25$ , and  $L = 0.5 \mu\text{m}$ , with  $\Omega(x)$  linear and  $\bar{\Omega} = 0.3$  and  $0.4$ . In this case  $\lambda_c$  shifts to shorter wavelengths as  $\bar{\Omega}$  increases, but the large bump in the  $\bar{\Omega} = 0.4$  curve at  $\lambda \approx 3 \mu\text{m}$  disappears when  $\bar{\Omega} \rightarrow 0.3$ . As a result  $\alpha_g$  increases from 0.97 to 0.98. In general, the Bruggeman theory predicts that  $\alpha_g$  will increase as  $\bar{\Omega}$  decreases when the coated sphere dielectric constant is used for  $\epsilon_c$ .



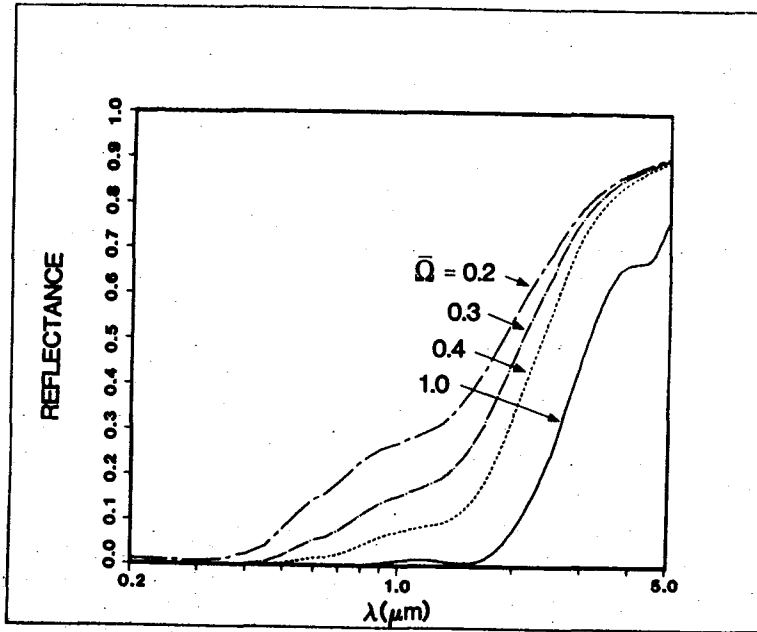
V-19 Spectral reflectance of a Bruggeman black Cr film with  $n = 3$ ,  $L = 0.4 \mu\text{m}$  and  $f = 0.2$ . As  $\bar{\Omega}$  decreases,  $\lambda_c$  moves to longer wavelengths and the solar absorptance increases.



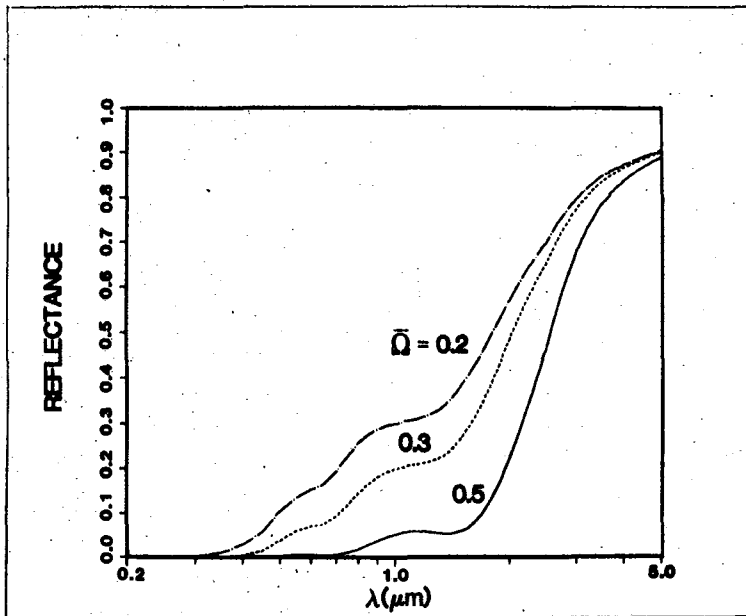
V-20 Spectral reflectance of a Bruggeman modeled black Cr film with  $n = 3$ ,  $f = 0.25$  and  $L = 0.5 \mu\text{m}$ . In this case,  $\lambda_c$  decreases as  $\bar{\Omega}$  decreases but the disappearance of the peak in  $R(\lambda)$  at  $\lambda \approx 3 \mu\text{m}$  as  $\bar{\Omega}$  decreases from 0.4 to 0.3 actually leads to an increase in  $\alpha_s$ .

Another model which was examined was that of a Maxwell-Garnett mixture of Cr particles in a Bruggeman matrix of air and Cr<sub>2</sub>O<sub>3</sub> particles, Fig. V-3(c). Eq. (IV-11) with  $L = 1/3$  was used to find the dielectric constant for the film, with the polarizability function  $\alpha$ , as given by Eq. (IV-10) determined using  $\epsilon_c = \epsilon_{Cr}$ , while  $\epsilon_m$  was calculated from  $\epsilon_B$  in Eq. (IV-31), with  $\epsilon_m = 1$  and  $\epsilon_c = \epsilon_{Cr_2O_3}$  in that equation. In calculating  $\epsilon_B$ ,  $f$  in Eq. (IV-31) was set at  $f_{Cr_2O_3}$  and in calculating  $\epsilon_{MG}$  in Eq. (IV-11),  $f$  was set at  $f_{Cr}$ . Some typical results of using this dielectric function model are shown in Fig. V-21. For this calculation the parameters used were  $L = 0.5 \mu m$ ,  $\bar{f} = 0.25$ , and  $n = 3$ ; thus this calculation can be compared with the Model B results shown in Fig. V-7. This comparison shows that the hybrid MG-Bruggeman model (Fig. V-21) predicts much larger changes in  $R(\lambda)$  with decreasing  $\bar{\Omega}$  than does the basic MG model (Fig. V-7). This effect causes  $\alpha_s$  to decrease more rapidly with an increasing volume fraction of Cr<sub>2</sub>O<sub>3</sub> for this hybrid model. Fig. V-8 compares the variation of  $\alpha_s$  with the relative volume fraction of Cr<sub>2</sub>O<sub>3</sub> [ $= (1 - \bar{\Omega})$ ] for the various models as well as some experimental data. For the regular MG model (Model B),  $\alpha_s$  remains constant until  $(1 - \bar{\Omega}) \gtrsim 0.5$ , while for the hybrid curve (MG/B) model,  $\alpha_s$  starts decreasing at small values of  $(1 - \bar{\Omega})$ .

Another possible black Cr microstructure is a Maxwell-Garnett assembly of Cr particles and Cr<sub>2</sub>O<sub>3</sub> particles in an air matrix, Fig. V-3(b). A calculation of  $R(\lambda)$  was performed using Eq. (IV-9) for the dielectric function with  $f_1 = f_{Cr}$  and  $f_2 = f_{Cr_2O_3}$ . The particles were assumed to be spherical with  $L_1 = L_2 = 1/3$ . A result of this calculation is shown in Fig. V-22. Model A conditions were assumed and  $\bar{\Omega}$  varied over the range 0.2-0.5. Again,  $\lambda_c$  shifts to shorter wavelengths with decreasing  $\bar{\Omega}$  but the shift is larger than that found with the coated sphere MG model. The variation of  $\alpha_s$  with  $(1 - \bar{\Omega})$  is shown in Fig. V-8,



V-21 Spectral reflectance of an MG array of Cr particles in a Bruggeman air/ $\text{Cr}_2\text{O}_3$  matrix. Parameters used in the calculation are  $n = 3$ ,  $L = 0.5 \mu\text{m}$ ,  $f = 0.25$ . The variation of  $\alpha_s$  with  $\bar{Q}$  for this model is shown in Fig. V-8.



V-22 Spectral reflectance of model MG black Cr film with Cr and  $\text{Cr}_2\text{O}_3$  particles dispersed in an air matrix. Parameters were those of Model-A, Table V-2. The variation of  $\alpha_2$  with  $\bar{Q}$  for this model is shown in Fig. V-8.

curve MG(Cr, Cr<sub>2</sub>O<sub>3</sub>). This dependence of  $\alpha_s$  on  $(1 - \bar{\Omega})$  is similar to that found for the hybrid model.

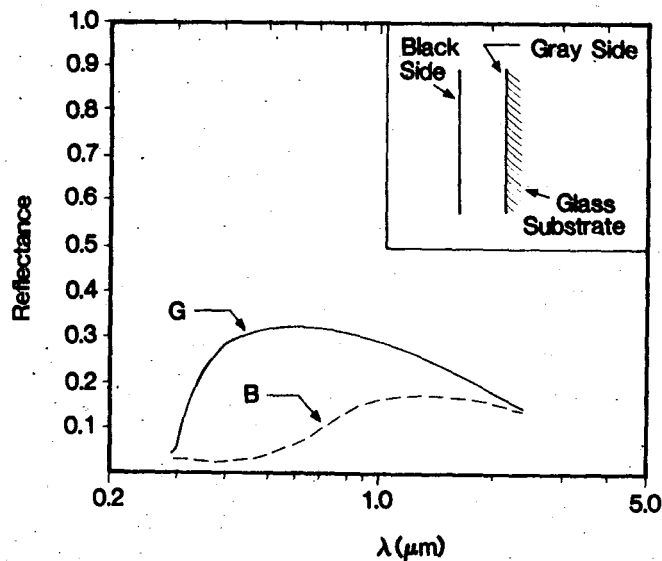
From the calculations in this section, it can be seen that all of the Maxwell-Garnett based models predict the same qualitative features: a shift of  $\lambda_c$  to shorter wavelengths as  $(1 - \bar{\Omega})$  increases, with consequent decreases in both  $\alpha_s$  and  $\epsilon(T)$ . The experimentally observed variation in  $\alpha_s$  with  $(1 - \bar{\Omega})$  is predicted most accurately by the coated sphere MG model, but even with this model, the calculated  $\alpha_s$  decreases somewhat more rapidly at large values of  $(1 - \bar{\Omega})$  than does the observed  $\alpha_s$ .

#### D. Results of Experiments and Calculations with Stripped Films

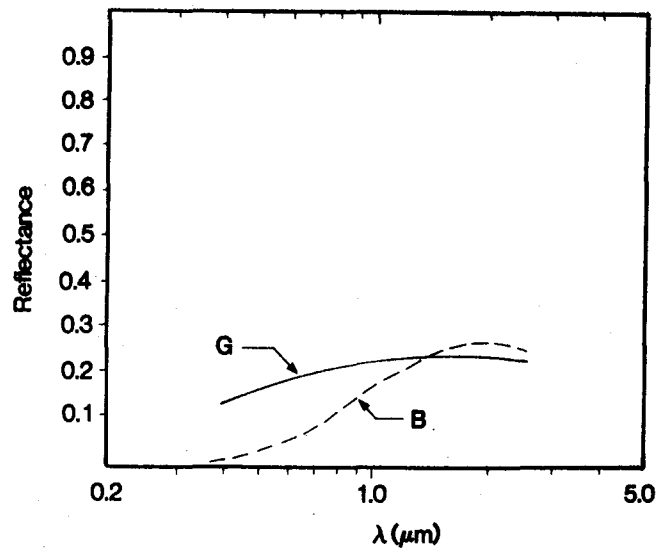
The reflectance measurements described above were all made on black Cr films plated onto thick Ni substrates. Although these measurements yield valuable information about the nature of the film structure, they do not uniquely specify this structure. In an attempt to better define the structure and optical properties of black Cr, several experiments were performed on films removed from their substrates. For these experiments, black Cr films were plated onto thin (~.025 cm) iron substrates and then the iron was slowly removed by etching the plated structure in a dilute nitric acid/methanol mixture.<sup>23</sup> If the substrates and films were unsupported in the etchant bath, the black Cr films broke up. When the substrate was placed on a glass slide during etching, the black Cr films adhered to the glass after the substrate had been completely removed.

Examination of the stripped films on glass showed that the back or substrate side ( $x = L$ ) was gray in color, indicating the presence of a high metal volume fraction at that surface. The front side remained black in appearance after the stripping operation. Although the side next to the glass was gray, it is definitely possible that this side of the black Cr film could have been altered by the etching process.

Experimental results of spectral hemispherical reflectance measurements for two different stripped films are shown in Figs. V-23 and V-24. The film geometry is shown on the inset in Fig. V-23. In both cases, the black side reflectance is small at short wavelengths and then increases to a maximum at a wavelength in the range 1-3  $\mu\text{m}$ . The "gray" side reflectance is appreciable at short wavelengths and has a broad maximum. For the gray side reflectance in Fig. V-23, the rapid decrease near  $\lambda = 0.3 \mu\text{m}$  is probably a result of absorption in the glass substrate. The gray side reflectance is also affected to some extent by the reflections produced by the glass substrate. Typically, these substrates produce a reflectance of about 4% for each surface at wavelengths  $\lambda \gtrsim 0.4 \mu\text{m}$ .

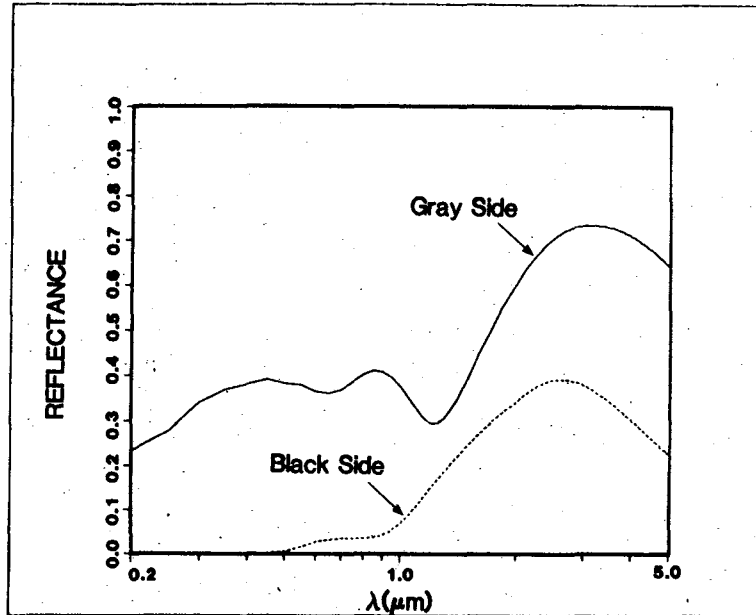


V-23 Experimental spectral reflectance for a stripped black Cr film as measured with light incident on the front or black (B) side and on the back or gray (G) side. The rapid drop in the gray side  $R(\lambda)$  at  $\lambda < 0.3 \mu\text{m}$  is probably a result of absorptance in the glass substrate at short wavelengths.

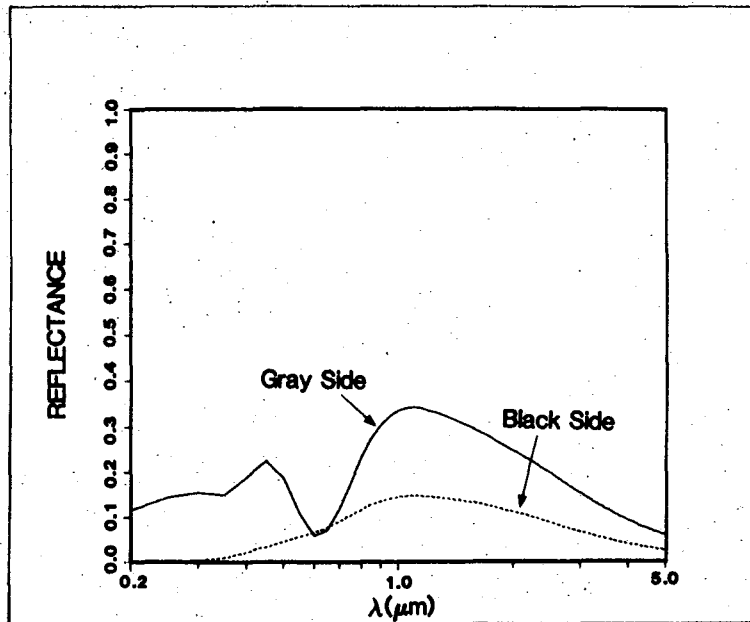


V-24 Experimental reflectance of another film stripped from a steel substrate. Curve G is the reflectance for light incident on the back or gray side and curve B is for light incident on the front or black side.

The stripping operation probably produced some damage to or alteration of the black Cr films. SEM examination of the black side of one film indicated that the surface morphology was similar to that of a regular black Cr film plated on a smooth Ni substrate. A calculation of stripped or bare film reflectances using model-A parameters and  $\bar{\Omega} = 0.4$  is shown in Fig. V-25. Both the gray and black side reflectances are significantly higher in magnitude than the experimental reflectance shown in Figs. V-23 and V-24. If the assumption is made that the stripping operation removes some of the black Cr film at the substrate side, then agreement between theory and experiment might be significantly improved. Fig. V-26 shows the result of a calculation in which L was reduced from 0.4  $\mu\text{m}$  to 0.3  $\mu\text{m}$  and  $\bar{f}$  reduced from 0.3 to 0.2. The reflectance magnitudes are now in reasonably good agreement with the experimental results and both exhibit maxima near  $\lambda = 1 \mu\text{m}$ . The oscillation in the gray side reflectance at  $\lambda < 1 \mu\text{m}$  is

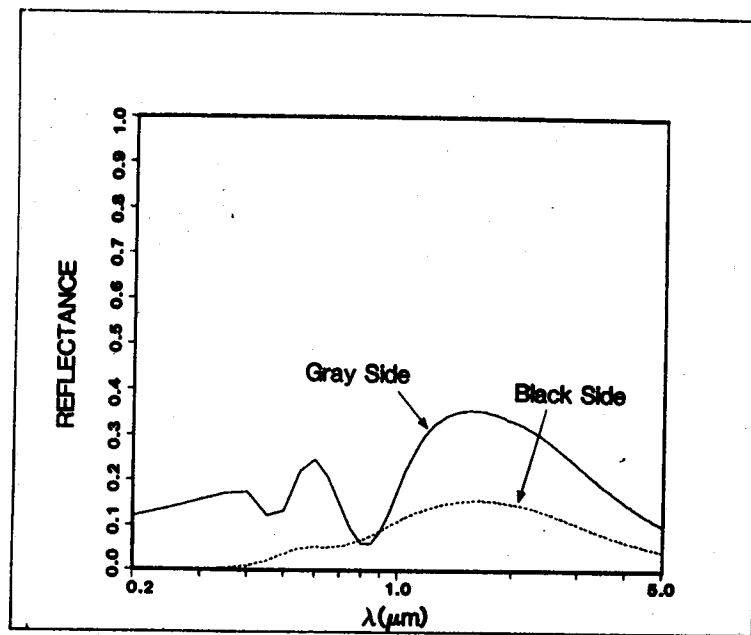


V-25 Calculated spectral reflectance for a stripped film with  $n = 3$ ,  $L = 0.4$ , and  $f = 0.3$ .



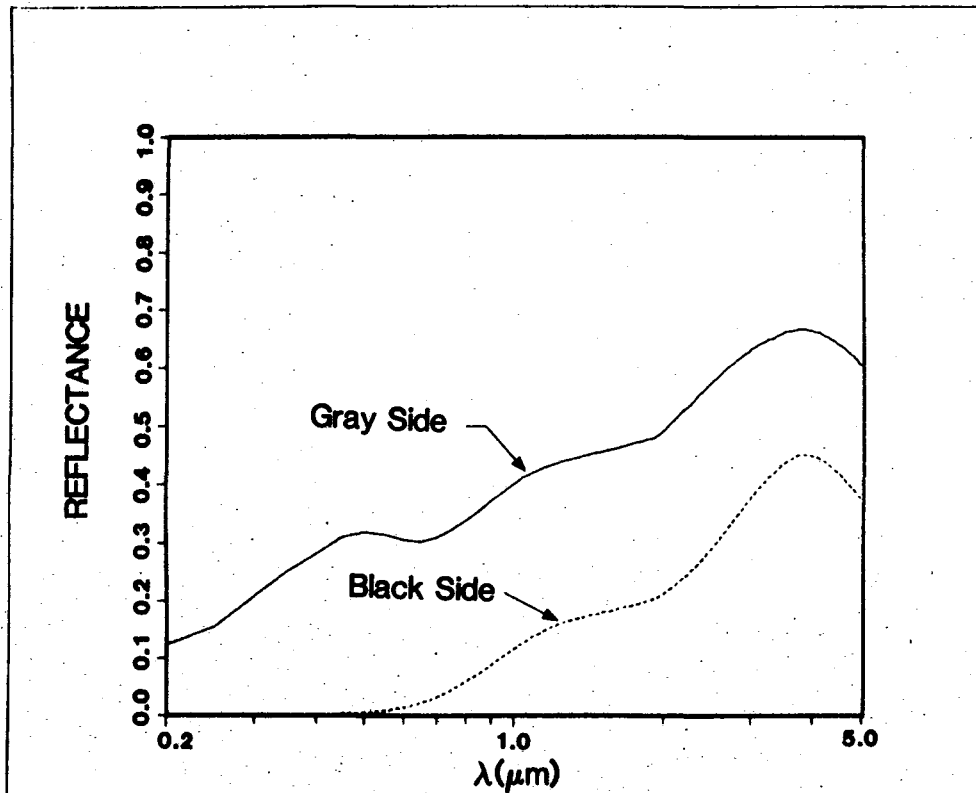
V-26 Calculated spectral reflectance for the stripped film in Fig. V-25 with  $L$  decreased from  $0.4$  to  $0.3 \mu\text{m}$  and  $f$  reduced from  $0.3$  to  $0.2$ .

a result of "interference" effects produced by the planar uniform film. Changing the film thickness from  $0.3 \mu\text{m}$  to  $0.4 \mu\text{m}$  while leaving all other parameters at their original values changes the shape and position of these oscillations but does not produce any other significant effect. Results of this alternate calculation are shown in Fig. V-27. From this result, we conclude that these oscillations are artifacts produced by the uniform thickness film used in the model.



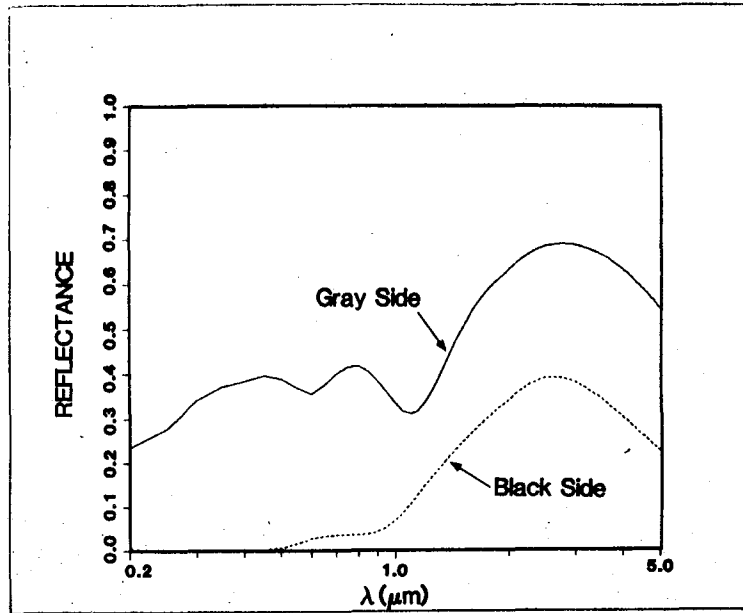
V-27 Calculated spectral reflectance for the same stripped film as in Fig. V-26 but with  $L$  increased to  $0.4 \mu\text{m}$ .

It is interesting to compare the results in Fig. V-26, calculated using the Maxwell-Garnett dielectric function, with results from a similar calculation in which the Bruggeman dielectric function is employed. Fig. V-28 shows the results of the Bruggeman calculation. The peaks in both the gray and black side reflectances are displaced to a longer wavelength and both reflectances have larger

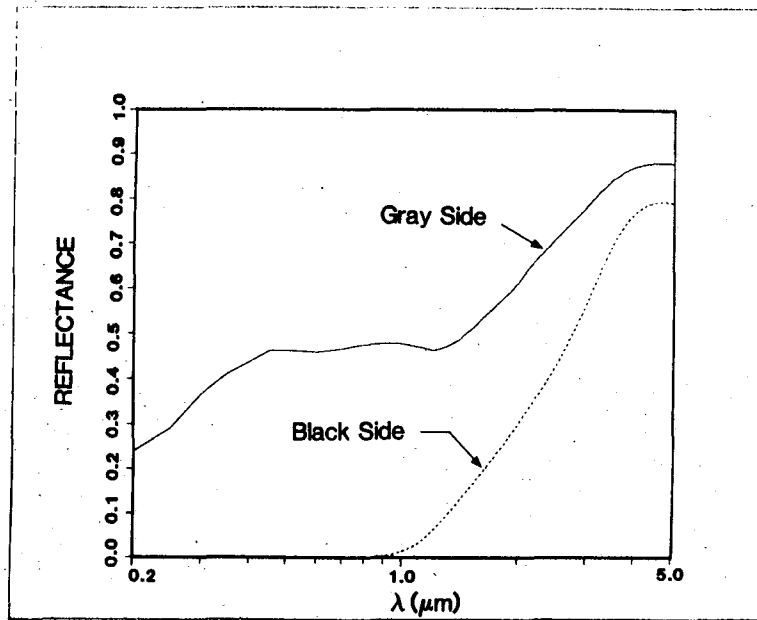


V-28 Spectral reflectance of a model Bruggeman black Cr stripped film using the same parameters as in Fig. V-26.

peak magnitudes. This behavior is a direct consequence of the more "metallic" nature of the Bruggeman dielectric function at high volume fractions relative to the MG function. As a result, a Bruggeman film tends to act as an intrinsic selective absorber, i.e., an absorber whose selective properties do not depend on the presence of a metallic substrate. This effect can be more graphically illustrated by comparing MG and Bruggeman calculations for a situation in which the maximum volume fraction,  $f(L)$ , is large. Fig. V-29 shows the result of an MG calculation for a Model-A film with  $f(L) = 0.9$  and  $\bar{f} = 0.3$ . This result can be compared to the MG result shown in Fig. V-27 in which the only change is a reduction of  $\bar{f}$  from 0.3 to 0.2. As  $\bar{f}$  increases, the magnitudes of both the gray and black side reflectances increase and the peaks in both curves move to the longer wavelengths. The Bruggeman results for a Model-A film are shown in Fig. V-30 and are quite markedly different from the MG results of Fig. V-29. In particular,



V-29 Spectral reflectance for a model-A MG black Cr stripped film.



V-30 Spectral reflectance for a model-A Bruggeman stripped film. The calculated black side reflectance shows the intrinsic selective absorbing nature of a Bruggeman film with a high metal volume fraction at the gray surface.

the black side reflectance (dashed line) for  $\lambda \lesssim 4 \mu\text{m}$  is essentially unchanged from the case in which a substrate is present. This intrinsic selective nature of Bruggeman absorbers has previously been discussed by Berthier and Lafait<sup>74</sup> and is a consequence of the "percolation" effect discussed in Sec. IV-D.

## VI. Discussion and Conclusions

From the experimental results and the various calculations described in the preceding section, we have concluded that the MG model provides a reasonable basis for explaining the optical behavior of black Cr coatings and that thermal aging of black Cr is primarily caused by oxidation of Cr crystallites in the coating. This aging is accompanied by a shift of  $\lambda_c$  to shorter wavelengths with a consequent decrease in both  $\alpha_s$  and  $\epsilon_H$ . A major prediction of the theory, as shown in Fig. V-8, is that  $\alpha_s$  will decrease slowly with increasing  $\text{Cr}_2\text{O}_3$  content until substantial oxidation has occurred (small  $\bar{\Omega}$ ). Then, further decreases in  $\bar{\Omega}$  lead to large decreases in  $\alpha_s$ . The microstructure investigations described by Pettit, Sweet and Sowell show that the clustering of the large particles which make up the coating (see Fig. V-3) can be correlated with the coating thermal stability.<sup>3</sup> In more stable coatings, the particles tend to cluster together and this clustering is presumed to inhibit oxidation of Cr crystallites in the particles.

There have been two major previous efforts to compare experimental black Cr spectral reflectance data with the predictions of various theories.<sup>74,75</sup> Berthier and Lafait<sup>74</sup> utilized a model black Cr film with three layers. The top layer was 0.1  $\mu\text{m}$  in thickness and consisted of  $\text{Cr}_2\text{O}_3$  cones or cylinders with air in the void space. The next layer was 0.3  $\mu\text{m}$  of Cr in a  $\text{Cr}_2\text{O}_3$  matrix, with the dependence of the volume fraction of Cr on depth in the layer determined from ESCA data in a manner analogous to that which we used to determine our  $\Omega(x)$  function. The functional form given by Berthier and Lafait (Fig. 4 of Ref. 74) is very similar to the experimental  $\Omega$  vs  $x/L$  curve shown in Fig. V-4 for an as-deposited specimen. Our value of  $\Omega_{\text{max}} \approx 0.8$  is also in reasonably good agreement with their indicated value of  $\Omega_{\text{max}} \approx 0.6 \pm 0.1$ . The next layer was a 0.04  $\mu\text{m}$  thick layer of Ni/Cr cermet to simulate surface roughness and the film was assumed to

be on a semiinfinite Ni substrate. No information was presented on the sensitivity of the resulting calculations to the model parameters discussed above.

Berthier and Lafait concluded that their spectral reflectance data for unaged samples was best fit by the Bruggeman theory. However, in their derivation of the Cr volume fraction from ESCA data, they assumed that the 0.3  $\mu\text{m}$  Cr/Cr<sub>2</sub>O<sub>3</sub> portion of the film was 100% dense, with no accompanying void volume. This in turn results in a maximum volume fraction,  $f_{\text{Cr-max}} = 0.6$  in their theory. Thus, their model did not satisfy our requirement, Eq. (V-16), which leads to  $f_{\text{max}} \gtrsim 0.9$ . As we have demonstrated, the Bruggeman theory can also yield good results with our model for as-deposited films (see Fig. V-19 with  $\bar{\Omega} = 1.0$ ). Thus, the type of comparison presented by Berthier and Lafait does not provide a definitive test of the theory.

Another comparison of the predictions of various effective medium theories has been made by Zajac.<sup>75</sup> The experimental data used was the specular reflectance of a black Cr film both unaged and aged at 350°C for 12 h and 450°C for 12 h. In the Zajac structural model, there are three layers of particles, with the top layer being 0.04  $\mu\text{m}$  thick and the two bottom layers 0.08  $\mu\text{m}$  thick. The layers were each composed of oxide coated Cr particles and, in fitting theory to experiment, several parameters were adjusted. These included the layer fill factor  $f_i$ , the layer  $\Omega$  value  $\Omega_i$ , and the index of refraction of the oxide coatings. In addition, a lognormal distribution of prolate spheroids was assumed, with an average eccentricity parameter,  $\bar{r} = 2$  and standard deviation parameter  $\sigma_r = 3$ . The parameters used in the lognormal distribution are  $\bar{x} = \bar{r} - 1$  and  $\sigma_r$ ,<sup>49</sup> with the probability density function being defined by

$$g(x) = [1/(2\pi x \ln \sigma_r)] \exp[-\ln^2(x/\bar{x})/2 \ln^2 \sigma_r] \quad , \quad (\text{VI-1})$$

with  $x = r - 1$ . Using Eq. (VI-1) with  $\bar{x} = 1$  and  $\sigma_r = 3$  it is easy to show that 10% of the particles have  $r > 5$ . These particles are much more strongly absorbing

than the spherical particles, as indicated by the rapid increase of the imaginary part of the index of refraction with increasing eccentricity as shown in Fig. IV-12 for  $\lambda = 1 \mu\text{m}$ . The net effect of postulating the existence of highly eccentric particles in a film is to make that film more strongly absorbing at short wavelengths and at lower metallic volume fractions. With reasonable values for the parameters discussed above, Zajac, et al. find good agreement between calculated and experimental reflectance spectra.<sup>26,75</sup>

Zajac has also reported some results on the reflectance  $R$  and transmittance  $T$  of a stripped film.<sup>75</sup> In this case, the data reported are the  $n$  and  $k$  values associated with the complex index of refraction, as derived from a model of a uniform film with  $n(\lambda)$  and  $k(\lambda)$  characterizing the whole film at wavelength  $\lambda$ . The film thickness was assumed to be  $0.2 \mu\text{m}$  and the experimental measurements were made on a film mounted on an AgCl substrate.  $R(\lambda)$  and  $T(\lambda)$  data were not presented directly, but using the formalism discussed in Sec IV-E,  $R(\lambda)$  and  $T(\lambda)$  could be calculated from the single layer version of that theory. The calculated reflectance for Zajac's film is qualitatively similar to that shown for the black side of one of our films, Fig. V-23. It is small at short wavelengths and has a peak value,  $R_{\text{max}} \approx 0.2$  near  $\lambda = 2 \mu\text{m}$ . In calculations using model dielectric constants, Zajac found the best agreement between theory and experiment for  $n(\lambda)$  and  $k(\lambda)$  when either the Bruggeman or the MG theory with a log-normal particle eccentricity distribution were employed. When a single MG layer with a low  $f$  value was used, agreement was poor. From this comparison between theory and experiment, Zajac concluded that the Bruggeman theory was probably the best effective medium theory for describing black Cr since it was valid at all volume fractions and it led to qualitatively correct predictions for  $n(\lambda)$  and  $k(\lambda)$  for a stripped film.

As discussed in Sec. V-D, the results of our stripped film reflectance measurements indicate that the reflectance in the wavelength region  $0.2 \mu\text{m} < \lambda \lesssim 1.0 \mu\text{m}$  is

substantially different for the two sides of the film. Thus it would appear that the film cannot be treated as a uniform composite medium characterized by a single complex index of refraction or dielectric constant. The MG graded layer model leads to calculated reflectances for the two sides which are in reasonably good agreement with experiment although the calculated gray side reflectance is somewhat higher than the measured reflectance. The Bruggeman theory, for the same grading profiles, does not predict the correct reflectance spectra. On the basis of these results, we have concluded that the MG theory provides a better overall description of reflectance phenomena for black Cr than does the Bruggeman theory.

It appears that optical measurements alone cannot be used to uniquely specify the microstructure of a composite MG type of coating. This occurs because several different effects can lead to the same type of optical behavior. In particular, the absorption in an MG layer can be increased either by increasing the metallic volume fraction or by increasing the particle eccentricity (see Fig. IV-13). The basic MG theory seems to remain valid at high metal volume fractions, at least in the case of cubic inclusions. In the case of spherical inclusions, the MG theory remains valid until the spheres are almost touching. The exact trajectory followed by  $\epsilon_{MG}$  in the complex plane as  $f$  increases depends on the average particle shape and on the details of the particle shape distribution function.

Within the framework of our spherical inclusion, graded fill factor MG model, we have seen that the spectral reflectance depends on three basic parameters; the coating thickness  $L$ , the average fill factor  $\bar{f}$ , and the exponent describing the grading profile  $n$ . Both  $\bar{f}$  and  $L$  can be estimated from experimental measurements and these parameters in turn determine  $n$  through Eqs. (V-16). There is no direct independent evidence for the correct value of  $n$  to use. In our model, within the uncertainty in  $\bar{f}$  and  $L$ , the value of  $n$  falls in the range  $2 \lesssim n \lesssim 3$ . If  $n$  could be determined independently, the problem could be further parameterized

by introducing a distribution of particle shapes. The parameters of the distribution could then be chosen to provide agreement with experiment. Thus, our and other existing models must be viewed as somewhat phenomenological in nature in that they contain a surplus of parameters which can be arbitrarily adjusted to match theory to experiment. More details of the coating microstructure are needed to further define the existing models. As discussed in Sec. V-A, the exact details of the microstructure of the  $\sim 0.2 \mu\text{m}$  particles which make up a typical black Cr film are unknown. Additional TEM and Auger studies are planned in an attempt to further define the structure and morphology of the materials in these particles.

In summary, we have presented the results of reflectance calculations for a model black Cr system which are in good agreement with experimental data. The results of these calculations indicate that the changes in  $R(\lambda)$  which occur during thermal aging are a result of oxidation of Cr crystallites in the coating. As the crystallites oxidize, the reflectance edge shifts toward short wavelengths, with a consequent decrease in both  $\alpha_s$  and  $\epsilon_H$ . When the relative volume fraction of Cr to  $(\text{Cr} + \text{Cr}_2\text{O}_3)$  drops to 0.30, the solar absorptance starts to drop rapidly with further oxidation.

If this picture of a black Cr coating is correct, then improvements in the coating thermal stability can only be made by reducing the oxidation rate of the Cr crystallites in the coating. The oxidation at a given temperature is controlled by the film structure, which determines how easily oxygen molecules can get to the surface of a Cr crystallite in one of the particles which make up the coating. Structures in which these particles tend to cluster together appear more resistant to oxidation than do more open structures. Careful control of plating process variables is required in order to reliably produce black Cr films with these oxidation resistant structures.



Appendix A

Dielectric Constant of an MG Medium with Randomly Oriented Ellipsoidal Inclusions

The general equation for  $\epsilon_{MG}$ , Eq. (IV-8), contains terms of the form,  $\sum_i f_i E_{in(i)}$ , where  $f_i$  = volume fraction of the  $i$ th species of inclusion and  $E_{in(i)}$  is the internal field in this species in the direction of the applied field,  $\vec{E}_0$ . In this Appendix, we derive the result, Eq. (IV-18) for the MG dielectric constant of a random spatial distribution of ellipsoidal inclusions.

We shall assume that the inclusions in the medium are all prolate or oblate spheroids which can be specified by their eccentricity  $r$  and by a set of Euler angles  $\vec{\Omega} = (\phi, \psi, \theta)$ , as shown in Fig. A-1.  $\phi$  is the usual Azimuthal angle, and  $\theta$  the usual polar angle, while the angle  $\psi$  represents a rotation of an ellipsoidal inclusion about its own internal long ( $z'$ ) axis. We also assume that the distribution function,  $f(r, \vec{\Omega})$  defining the random distribution of inclusions is separable into an eccentricity component and an angular component,

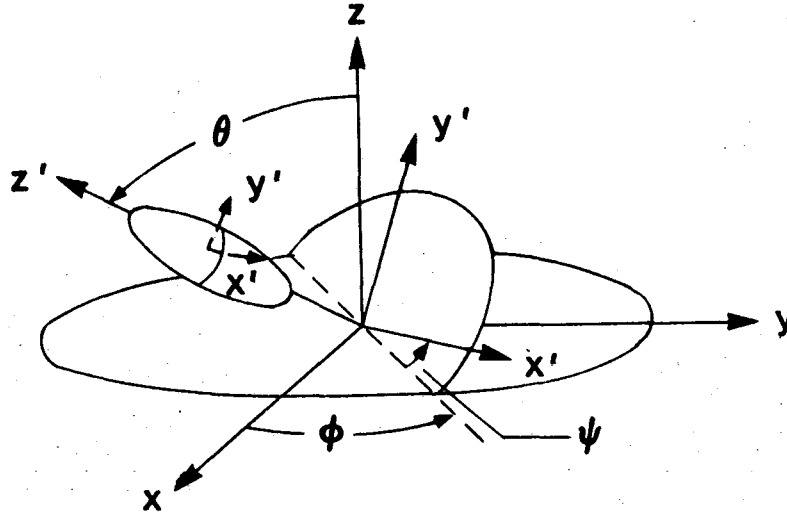
$$f(r, \vec{\Omega}) = \rho(r)g(\vec{\Omega}) \quad (A-1)$$

In Eq. (A-1),  $\rho(r)$  is the volume fraction of ellipsoids with eccentricities in the range  $r$  to  $r + dr$  and  $g(\vec{\Omega})d\vec{\Omega}$  is the probability that a given ellipsoid will have Euler angles within the differential volume  $d\vec{\Omega}$  in  $(\phi, \psi, \theta)$  space. Using Eq. (A-1), the sum,  $\sum_i f_i E_{in(i)}$  can be written,

$$\sum_i f_i E_{in(i)} = \int_1^\infty \rho(r)dr \int_{\Delta\vec{\Omega}} g(\vec{\Omega})E_{in}(r, \vec{\Omega})d\vec{\Omega} \quad (A-2)$$

In Eq. (A-2), the range  $\Delta\vec{\Omega}$  is specified by,  $0 < \phi < \pi$ ,  $0 < \theta < \pi/2$ ,  $0 < \psi < \pi$ .

To find an expression for  $E_{in}(r, \vec{\Omega})$ , we consider a situation in which  $\vec{E}_0 = E_0 \hat{x}$ , as shown in Fig. A-1. The problem is to find the components of  $\vec{E}_0$  in the rotated



A-1 Euler angles  $(\phi, \psi, \theta)$  describing the orientation of an ellipsoid. The  $x', y', z'$  axis system is fixed in the ellipsoid while the  $x, y, z$  axis system is fixed in space. In describing a rotation, the ellipsoid is first tipped by an angle  $\theta$ , then rotated in the  $x$ - $y$  plane by an angle  $\phi$  and finally rotated by an angle  $\psi$  about the  $z'$  axis.

or principal axis coordinate system and then use Eq. (IV-6) for the internal field produced by an external field along a principal axis. Goldstein<sup>76</sup> shows that the coordinates of a vector  $\vec{r}$  in the primed system are related to those in the unprimed system by the matrix equation,

$$(\vec{r})' = A\vec{r} \quad , \quad (A-3)$$

where the transpose of  $\vec{r}$ , as designated by  $\vec{r}^T$ , is given by  $\vec{r}^T = (x, y, z)$ . The matrix  $A$  is specified by,

$$A = \begin{bmatrix} \cos\psi\cos\phi - \cos\theta\sin\phi\sin\psi & \cos\psi\sin\phi + \cos\theta\cos\phi\sin\psi & \sin\psi\sin\theta \\ -\sin\psi\cos\phi - \cos\theta\sin\phi\cos\psi & -\sin\psi\sin\phi + \cos\theta\cos\phi\cos\psi & \cos\psi\sin\theta \\ \sin\theta\sin\phi & -\sin\theta\cos\phi & \cos\theta \end{bmatrix} \quad (A-4)$$

The inverse of A is given by

$$A^{-1} = \begin{bmatrix} \cos\psi\cos\phi - \cos\theta\sin\phi\sin\psi & -\sin\psi\cos\phi - \cos\theta\sin\phi\cos\psi & \sin\theta\sin\phi \\ \cos\psi\sin\phi + \cos\theta\cos\phi\sin\psi & -\sin\psi\sin\phi + \cos\theta\cos\phi\cos\psi & -\sin\theta\cos\phi \\ \sin\theta\sin\psi & \sin\theta\cos\psi & \cos\theta \end{bmatrix} \quad (A-5)$$

Using Eq. (A-3) with  $\vec{r} = \hat{x}$  yields,

$$\begin{aligned} \vec{(r)'} &= A \begin{bmatrix} 1 \\ 0 \\ 0 \end{bmatrix} \\ &= \begin{bmatrix} \cos\psi\cos\phi - \cos\theta\sin\phi\sin\psi \\ -\sin\psi\cos\phi - \cos\theta\sin\phi\cos\psi \\ \sin\theta\sin\psi \end{bmatrix} \end{aligned} \quad (A-6)$$

The applied field in the primed frame is now given by  $(\vec{E}_0)' = E_0(\vec{r})'$ . From Eq. (IV-6), the internal field along jth primed axis is given by,

$$E'_{in(j)} = \frac{\epsilon_m E'_0(j)}{\epsilon_c L_j + (1 - L_j)\epsilon_m} \quad (A-7)$$

where the index j specifies x', y', or z' and  $L_j$  is the associated depolarizing factor, as given by Eq. (IV-12) or (IV-14) for prolate or oblate spheroids respectively.

In order to find the x component of  $\vec{E}_{in}$  so that the integration in Eq. (A-2) can be performed,  $\vec{E}_{in}$  is transformed back to the original coordinate system via the prescription,  $\vec{E}_{in} = A^{-1}(\vec{E}_{in})'$ . This yields the relation,

$$E_{in(x)} = (A^{-1})_{11}E_{in(x')}^1 + (A^{-1})_{12}E_{in(y')}^1 + (A^{-1})_{13}E_{in(z')}^1 \quad (A-8)$$

$$\begin{aligned} \text{or } E_{in(x)} = \epsilon_m E_o \left\{ \frac{(\cos\psi\cos\theta - \cos\theta\sin\phi\sin\psi)^2}{\epsilon_c L_x + (1 - L_x)\epsilon_m} \right. \\ \left. + \frac{(\sin\psi\cos\phi + \cos\theta\sin\phi\cos\psi)^2}{\epsilon_c L_y + (1 - L_y)\epsilon_m} + \frac{(\sin\theta\sin\phi)^2}{\epsilon_m L_z + (1 - L_z)\epsilon_m} \right\} \quad (A-9) \end{aligned}$$

If  $g(\vec{\Omega})$  is known, the  $\vec{\Omega}$  integral in Eq. (A-2) can be performed, using Eq. (A-9) for  $E_{in}(r, \vec{\Omega})$  and Eqs. (IV-12) or (IV-14) for the  $L_j$  as functions of  $r$ .

A case of special interest is one in which the ellipsoidal inclusions have the internal rotation angle,  $\psi$ , uniformly distributed in the range  $0 \leq \psi \leq \pi$  and have their major axes distributed uniformly with respect to solid angle  $\vec{\chi}$ , when  $\vec{\chi}$  is specified by  $\theta$  and  $\phi$ . Then,  $g(\vec{\Omega}) \rightarrow (1/\pi^2)\sin\theta$  and

$$\begin{aligned} \int_{\Delta\Omega} g(\vec{\Omega}) E_{in}(r, \vec{\Omega}) d\vec{\Omega} \\ = \frac{1}{\pi^2} \int_0^\pi d\phi \int_0^\pi d\psi \int_0^{\pi/2} d\theta \left\{ \sin\theta E_{in(x)}(\phi, \psi, \theta, r) \right\} \quad (A-10) \end{aligned}$$

Using Eq. (A-9) in Eq. (A-10), it is easily shown that the integral of each angular term in Eq. (A-9) produces a factor of 1/3. The final result is,

$$\bar{E}_{in(x)} = \frac{E_o \epsilon_m}{3} \sum_{j=1}^3 \frac{1}{\epsilon_c L_j + (1 - L_j)\epsilon_m} \quad (A-11)$$

Eq. (A-11) for  $\bar{E}_{in(x)}$  is the basis for the factors of  $f/3$ , which appear in Eq. (IV-18). For uniform distributions it can be easily shown that  $\bar{E}_{in(y)} = \bar{E}_{in(z)} = 0$  and hence  $\vec{E}_0$  and  $\vec{E}_{in}$  are in the same direction. In cases where the ellipsoid major axes have a preferred spatial orientation, the applied and average internal field may not be pointed in the same direction.



## Appendix B

### Cube Polarization Calculations

The purpose of this appendix is to discuss calculations of the polarization of a dielectric cube subjected to a uniform external field. It is well known that the polarization in a solid body will not be uniform if the polarizable object in a uniform external field is nonellipsoidal in shape. Since the polarization in the body is caused by the total internal electric field, and this field in turn is produced by both the external sources and by the induced polarization, it is reasonable to conclude that this type of problem will have to be solved self-consistently for the polarization "charges." This is in fact the case, and several different formulations of the problem are possible.

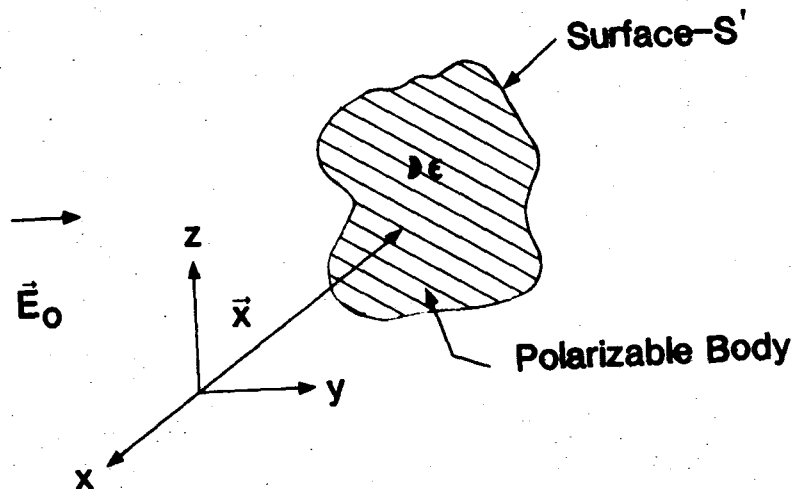
Various integral equation formulations for solving problems of this type have been discussed by Jaswon and Symm<sup>77</sup> and in a compact way by Lindholm.<sup>78</sup> We shall examine two different surface integral equations which can be used to calculate the polarization and then apply both methods to the specific case of a cube in a uniform field.

Fig. B-1 shows an arbitrarily shaped homogeneous body in a uniform external field  $\vec{E}_0$ . The polarization in the body  $\vec{P}(\vec{x})$  produces a potential of the form,

$$\phi_p(\vec{x}) = - \int \frac{\nabla \cdot \vec{P}(\vec{x}') d^3x'}{|\vec{x} - \vec{x}'|} + \int \frac{\vec{P}(\vec{x}') \cdot d\vec{S}'}{|\vec{x} - \vec{x}'|} \quad (\text{B-1})$$

In Eq. (B-1), the first integral is a volume integral over all internal regions of the body and the second integral is over the body surface. The displacement  $\vec{D}$ , electric field  $\vec{E}$ , and polarization  $\vec{P}$  in the body are related by the equation,

$$\vec{D} = \vec{E} + 4\pi\vec{P} \quad (\text{B-2})$$



B-1. Polarizable body with a dielectric constant  $\epsilon$  subjected to a uniform external field. The surface of the body is designated by  $S'$  and the vector  $\vec{x}$  is a position vector. Points on the surface of the body are designated by vectors  $\vec{x}'$ .

The fields  $\vec{D}$  and  $\vec{E}$  are, by assumption, related to each other through the dielectric constant,

$$\vec{D} = \epsilon \vec{E} \quad (\text{B-3})$$

Using the Maxwell equation,  $\nabla \cdot \vec{D} = 0$  yields,  $\nabla \cdot \vec{D} = \nabla \cdot \epsilon \vec{E} = \epsilon \nabla \cdot \vec{E} + \vec{E} \cdot \nabla \epsilon$ .

Since the body is assumed to be homogeneous,  $\nabla \epsilon = 0$  and hence  $\nabla \cdot \vec{E} = 0$  inside the body. Thus Eq. (B-2) plus the conditions  $\nabla \cdot \vec{E} = \nabla \cdot \vec{D} = 0$  yields  $\nabla \cdot \vec{P} = 0$  inside the body. As a result, only the second term of Eq. (B-1) contributes to  $\phi_p$ .

The total field  $\vec{E}(\vec{x})$  inside the body is given by  $\vec{E}(\vec{x}) = \vec{E}_0 + \vec{E}_p(\vec{x})$ , where  $\vec{E}_p = -\nabla \phi_p$ . Since  $\nabla(1/|\vec{x} - \vec{x}'|) = -(\vec{x} - \vec{x}')/|\vec{x} - \vec{x}'|^3$ , we can write,

$$\vec{E}(\vec{x}) = \vec{E}_0 + \int \frac{(\vec{x} - \vec{x}') \vec{P}(\vec{x}') \cdot d\vec{S}'}{|\vec{x} - \vec{x}'|^3} \quad (\text{B-4})$$

Eq. (B-4) is the starting point for Fuch's calculation.<sup>54</sup> Inside the body, the fields  $\vec{E}(\vec{x})$  and  $\vec{P}(\vec{x})$  are related through the material susceptibility,  $\chi = (\epsilon - 1)/4\pi$ , by  $\vec{P}(\vec{x}) = \chi\vec{E}(\vec{x})$ . If we let  $\vec{x}$  be a point infinitesimally inside the body, and  $\hat{n}(\vec{x})$  be the outward directed normal at that point, then the normal component of the polarization at  $\vec{x}$  is  $P_n(\vec{x}) = \hat{n}(\vec{x}) \cdot \vec{P}(\vec{x})$ . Taking the dot product of Eq. (B-4) with  $\hat{n}(\vec{x})$  and using the relation  $dS' = \hat{n}(\vec{x}')dS'$ , and substituting  $\vec{P}(\vec{x})/\chi$  for  $\vec{E}(\vec{x})$  in Eq. (B-4) yields the integral equation for  $P_n(\vec{x})$ ,

$$P_n(\vec{x})/\chi = \vec{E}_0 \cdot \hat{n}(\vec{x}) + \int \frac{\hat{n}(\vec{x}') \cdot (\vec{x} - \vec{x}')}{|\vec{x} - \vec{x}'|^3} P_n(\vec{x}') dS' \quad (\text{B-5})$$

In Eq. (B-5), the points  $\vec{x}$  and  $\vec{x}'$  are both on the surface of the body and hence there is a singularity at  $\vec{x} = \vec{x}'$ . This singularity is removable<sup>77</sup> and the equation can easily be cast in the form,

$$P_n(\vec{x})(1/\chi + 2\pi) = \vec{E}_0 \cdot \hat{n}(\vec{x}) + \int' \frac{\hat{n}(\vec{x}') \cdot (\vec{x} - \vec{x}')}{|\vec{x} - \vec{x}'|^3} P_n(\vec{x}') dS' \quad (\text{B-6})$$

where the prime on the integral indicates that an infinitesimal region near  $\vec{x} = \vec{x}'$  is to be omitted.

To demonstrate this singularity removal in an elementary way, we consider the integral over a small portion  $\Delta S'$  of the surface  $S'$  near  $\vec{x}$ , as shown in Fig. B-2(a). As  $\vec{x} \rightarrow \vec{x}'$ ,  $P_n(\vec{x}') \rightarrow P_n(\vec{x})$  and can be taken outside the integral, resulting in,

$$\int_{\Delta S'} P_n(\vec{x}') \frac{\hat{n}(\vec{x}') \cdot (\vec{x} - \vec{x}')}{|\vec{x} - \vec{x}'|^3} dS' \approx P_n(\vec{x}) \int_{\Delta S'} \frac{\hat{n}(\vec{x}') \cdot (\vec{x} - \vec{x}')}{|\vec{x} - \vec{x}'|^3} dS' \quad (\text{B-7})$$

To evaluate Eq. (B-7), we use the geometry shown in Fig. B-2(b), with  $\rho = |\vec{x} - \vec{x}'| = (r^2 + \Delta z^2)^{1/2}$ . The integral becomes

$$\begin{aligned}
& \int_{\Delta S'} \rightarrow P_n(\vec{x}) \int_{\Delta S'} \frac{\rho \cos \theta ds'}{\rho^3} \\
& \approx P_n(\vec{x}) \lim_{\Delta z \rightarrow 0} \int_0^{2\pi} d\theta \int_0^{r_{\max}} r dr \left\{ \frac{\Delta z}{(r^2 + \Delta z^2)^{3/2}} \right\} \\
& = -2\pi P_n(\vec{x}) \lim_{\Delta z \rightarrow 0} \Delta z \int_0^{r_{\max}} \frac{r dr}{(r^2 + \Delta z^2)^{3/2}}
\end{aligned}$$

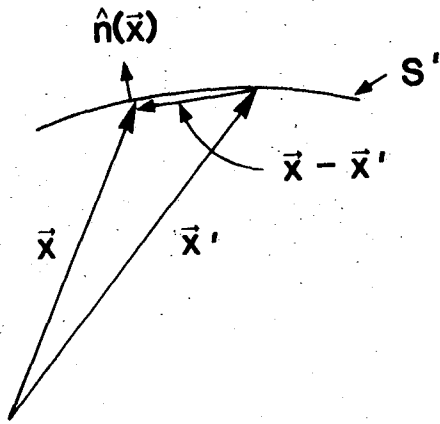
Evaluating the integral results in,

$$\begin{aligned}
& \int_{\Delta S'} \rightarrow 2\pi P_n(\vec{x}) \lim_{\Delta z \rightarrow 0} \left\{ \Delta z \left[ (r_{\max}^2 + \Delta z^2)^{-1/2} - 1/\Delta z \right] \right\} \quad (B-8) \\
& = -2\pi P_n(\vec{x})
\end{aligned}$$

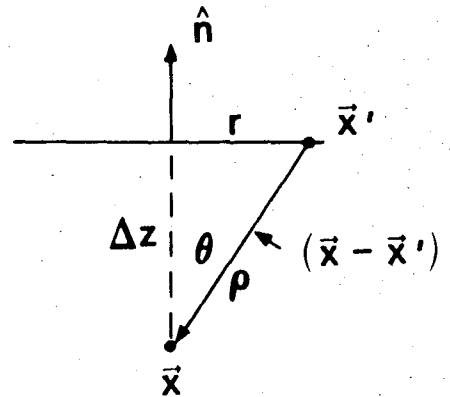
Eq. (B-8) shows that the removal of the singularity is essentially independent of the radius  $r_{\max}$  of the circular region centered about  $\vec{x}$ .

An alternate formulation yields an equation for the potential  $\phi(\vec{x})$  on the surface. Van Bladel presents a clear derivation of this equation through use of Green's theorem.<sup>54</sup> The result is,

$$\phi(\vec{x})/2 = \phi_a(\vec{x})/(\epsilon + 1) - (1/4\pi) \left( \frac{\epsilon - 1}{\epsilon + 1} \right) \int_{S'} \phi(\vec{x}') \frac{\partial}{\partial n'} \left\{ \frac{1}{|\vec{x} - \vec{x}'|} \right\} dS' \quad (B-9)$$



B-2. (a) A small portion of the body surface showing the vectors  $\vec{x}'$  on the surface and  $\vec{x}$  infinitesimally displaced inward from the surface  $n(\vec{x})$  is the outward normal at  $\vec{x}$ .



(b) Geometry used to evaluate the integral in Eq. (B-7)  $\Delta S'$  is a circular region on the surface with radius  $r$ .  $\Delta z$  = infinitesimal displacement distance of vector  $\vec{x}$  from the body surface.

In Eq. (B-9), the derivative  $\partial/\partial n'$  is the directional derivation in the direction of the unit vector  $\hat{n}'$  and the singularity at  $\vec{x} = \vec{x}'$  has been removed. Using the relation,  $\partial/\partial n'(1/|\vec{x} - \vec{x}'|) = \nabla'(1/|\vec{x} - \vec{x}'|) \cdot \hat{n}' = (\vec{x} - \vec{x}') \cdot \hat{n}'/|\vec{x} - \vec{x}'|^3$ ,

Eq. (B-9) can be rewritten in the form,

$$\phi_a(\vec{x}) = \frac{\epsilon + 1}{2} \phi(\vec{x}) + \frac{\epsilon - 1}{4\pi} \int_{S'} \frac{\phi(\vec{x}')(\vec{x} - \vec{x}') \cdot \hat{n}' dS'}{|\vec{x} - \vec{x}'|^3} \quad (\text{B-10})$$

Comparison of Eq. (B-6) and Eq. (B-10) shows that both equations are similar in structure.

The quantity of most interest is the net dipole moment of the polarized body,

$$\vec{p} = \int \vec{P}(\vec{x}) d^3x \quad (\text{B-11})$$

Fuchs<sup>53</sup> shows that this integral can be converted to the surface integral,

$$\vec{p} = \int P_n(\vec{x}') \vec{x}' dS' \quad , \quad (B-12)$$

so  $\vec{p}$  can be found directly from the solution of Eq. (B-6). Van Bladel shows that  $\vec{p}$  can also be found from the relation,<sup>55</sup>

$$\vec{p} = - (\epsilon - 1) \int_{S'} \phi(\vec{x}') \hat{n}(\vec{x}') dS' \quad , \quad (B-13)$$

so  $\vec{p}$  can also be derived directly from the solution of Eq. (B-10).

The integral equations, (B-6) or (B-10) are solved by breaking the object surface up into a number of discrete regions and then converting the equations into a number of inhomogeneous linear equations for the quantities  $P_n(\vec{x}_i)$  or  $\phi(\vec{x}_i)$ , where  $\vec{x}_i$  is the position vector of the "center" of subregion  $i$ . For bodies which have a degree of symmetry with respect to the applied field, it is necessary to find  $P_n$  or  $\phi$  over only a portion of the object surface. For a cube in a uniform field, only one quarter of the "top" surface and one eighth of the "front" surface need to be considered (the fundamental region), as shown in Fig. B-3. The normal polarization or potential at all other points on the cube surface can be found from the associated quantities in the fundamental region, shown cross-hatched in Fig. B-3. In our calculations, each cube face was broken up into an  $n \times n$  grid of square subareas, where  $n =$  odd integer. The special case,  $n = 5$  is shown in Fig. B-3.

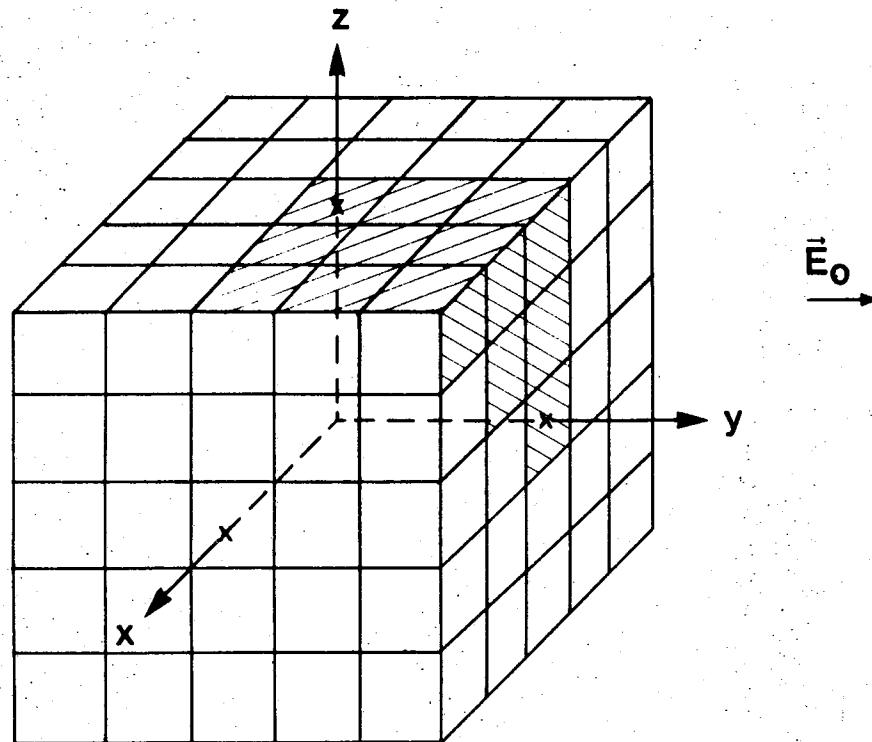
For the normal polarization formulation, Eq. (B-6), the integral equation is converted to a matrix equation,

$$AX = Y \quad (B-14)$$

where  $X$  and  $Y$  are  $N$  component column vectors and  $A$  is an  $N \times N$  matrix. The quantity  $N =$  number of values of  $P_n$  in the fundamental region and is related to  $n$  by  $N = (n + 1)(3n + 5)/8$ . There are  $L = [(n + 1)/2]^2$  values of  $P_n$  associated with the top surface and  $N - L$  values of  $P_n$  associated with the front surface. The transposes of  $X$  and  $Y$  are given by,

$$X^T = (P_{n(1)}, \dots, P_{n(L)}, P_{n(L+1)}, \dots, P_{n(N)}) \quad (B-15)$$

$$Y^T = E_0(0, \dots, 0, 1, \dots, 1)$$



B-3 Cube used in the polarization or potential calculations with  $n = 5$ . The shaded area is the fundamental region over which the calculation is performed.

The matrix  $A$  has diagonal elements,  $A_{11} = \gamma = 2\pi(\epsilon + 1)/(\epsilon - 1)$ , and off diagonal elements  $A_{ij}$  derived from the quantities  $R_{ij}$ , given by,

$$R_{ij} = \frac{\hat{n}_i \cdot (\vec{x}_i - \vec{x}_j) \Delta S_j}{|\vec{x}_i - \vec{x}_j|^3} \quad (\text{B-16})$$

In Eq. (B-16),  $\hat{n}_i$  is the outward directed unit normal for subregion  $i$  on the cube surface and  $\Delta S_j$  is the area of subregion  $j$ . The  $A_{ij}$  are found by summing Eq. (B-16) over all points equivalent to point  $j$  by symmetry outside the fundamental region, taking into account sign reversals produced by the symmetry condition,  $P_n(x,y,z) = -P_n(x,-y,z)$ . The cube was assumed to have unit dimension and hence  $\Delta S_j = \Delta S = 1/n^2$ .

For the potential formulation, Eq. (B-10), the applied potential was defined by  $\phi_a(\vec{x}) = -E_0 y$ . Eq. (B-10) was then cast in the form, (B-14) with Eq. (B-15) replaced by,

$$X^T = (\phi_1, \dots, \phi_L, \phi_{L+1}, \dots, \phi_N) \quad (\text{B-17})$$

$$Y^T = [-2/(\epsilon + 1)](y_1, \dots, y_L, 0.5, \dots, 0.5)$$

In Eq. (B-16) the quantities  $y_i$ ;  $i = 1, L$  are the  $y$  coordinates of the top face points in the fundamental region. The  $A$  matrix is defined by,

$$A_{ij} = 1; i = j$$

and  $A_{ij} = \gamma^{-1} \sum_{j'} Q_{ij'}$ , where the sum is over points  $j'$  on the cube surface equivalent to  $j$  in the fundamental region and  $Q_{ij}$  is defined by,

$$Q_{ij} = \frac{\hat{n}_j \cdot (\vec{x}_i - \vec{x}_j) \Delta S_j}{|\vec{x}_i - \vec{x}_j|^3} \quad (\text{B-18})$$

The solution of Eq. (B-14) was done through use of the Sandia Laboratories Mathematical Library Subroutine (CAXBI), a routine for solving nonsingular systems

of complex linear algebraic equations.<sup>79</sup> Typically, the solution for an 11 x 11 subregion array (n = 11) takes about five seconds on a CDC 6600 computer.

The results of a calculation using a real dielectric constant  $\epsilon$  are shown in Fig. B-4. The particle susceptibility  $\chi_p$  is defined by the relation,

$$\chi_p = \bar{P}_y / E_0 \quad , \quad (B-19)$$

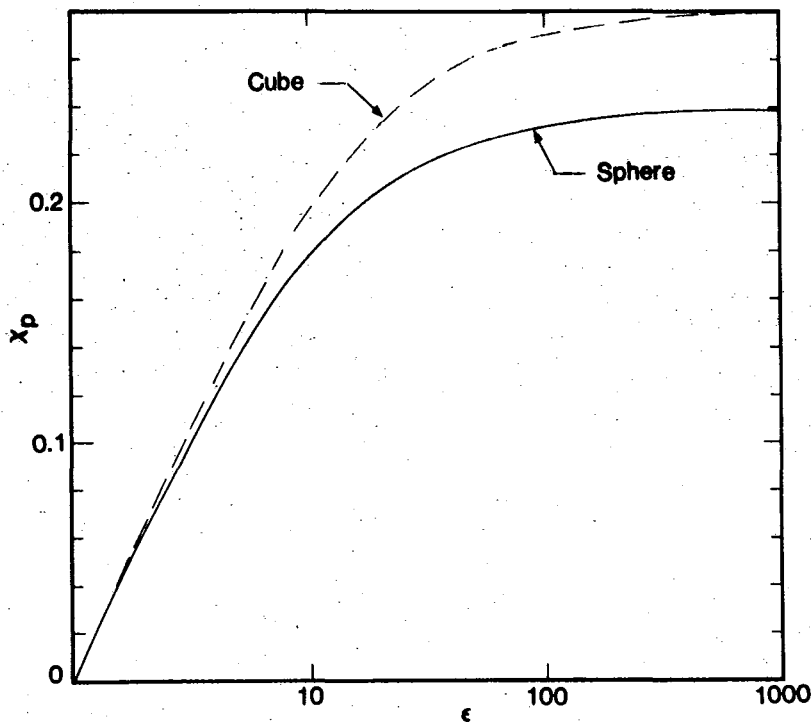
where  $\bar{P}_y$  = average y component polarization in the particle. The dipole moment is related to  $\chi_p$  via the relation,  $p = V\chi_p E_0$ , where  $V$  = particle volume. For ellipsoidal particles,  $\bar{P}_y = P_y = \text{constant}$  and  $\chi_p$  can be calculated explicitly. Using Eq. (IV-6) for the internal electric field plus the relation  $\bar{P} = \chi E_{in}$ , it is easy to show that the ellipsoidal particle susceptibility is given by,

$$\chi_p = \frac{1}{4\pi} \frac{\epsilon - 1}{\epsilon L + 1 - L} \quad (B-20)$$

where  $L$  = depolarizing factor in the field direction. Fig. B-4 shows the result using Eq. (B-20) for a sphere, with  $L = 1/3$ , as compared to the numerical calculation for a cube found using the "polarization" formulation, Eqs. (B-6) and (B-12). It can be seen that the particle susceptibilities for a cube and a sphere are reasonably close to each other for small  $\epsilon$ , with a maximum variation ~16% as  $\epsilon \rightarrow \infty$ . This result is in agreement with the well known engineering practice of approximating  $\chi_p$  of rectangular parallelepipeds from the corresponding  $\chi_p$  of an inscribed ellipsoid.

The calculation is slightly sensitive to the number of subregions/face,  $n^2$ . We have used  $n = 11$  because of computer memory limitations. However, trial calculations with values of  $n$  up to 19 indicate that  $\chi_p$  for  $n = 11$  is probably

within ~3% of the limiting case,  $n = \infty$ , value. Table B-I shows an example of this for  $\epsilon = 20$ . The extrapolation to  $n = \infty$  was performed by fitting  $\chi_p$  to an expression of the form  $\chi_p(n) = \alpha + \beta n^{-1}$ , where  $\alpha$  and  $\beta$  are constants. In the limit,  $n \rightarrow \infty$ ,  $\chi_p \rightarrow \alpha$ . The value of  $\alpha$  obtained from a least squares fit to the  $\chi_p$  results in Table B-I was 0.2401 and the 95% confidence region for  $\alpha$  was  $\pm 1.8 \times 10^{-4}$ . There is no theoretical reason that  $\chi_p$  should depend on  $n$  in this fashion, but over the region of  $n$  investigated, the fit is quite good, with an estimated standard error  $s = 6.2 \times 10^{-5}$ .



B-4 Particle susceptibility  $\chi_p$  as defined by Eq. (B-18).

Table B-I. Dependence of  $\chi_p$  on number of subregions/side, n

	<u>n</u>	<u><math>\chi_p</math></u>
	3	0.2146
	5	0.2259
	7	0.2300
	9	0.2321
	11	0.2336
	13	0.2346
	15	0.2354
Extrapolated	17	0.2360
	19	0.2365
	$\infty$	0.2401 $\pm$ .0002

The results of a calculation using the "potential" formulation, Eqs. (B-10) and (B-13) were very close to those shown in Fig. B-4. The maximum deviation was ~2% at high dielectric constants,  $\epsilon \gtrsim 1000$ . The potential formulation is more difficult computationally at high dielectric constants because the dipole moment, as calculated from Eq. (B-13), involves multiplication of a very large factor,  $(\epsilon - 1)$ , times a small factor, the potential surface integral. Hence, small errors in calculating the cube front surface potential can produce large errors in calculating the dipole moment. Using the potential formulation, Van Bladel found a limiting value,  $\chi_p \approx 0.135$  as  $\epsilon \rightarrow \infty$ . We feel that this result is in error.

For a Cr particle at  $\lambda = 1 \mu\text{m}$ ,  $\epsilon = -1.049 + 24.4 j$ . In this case the sphere particle susceptibility is, from Eq. (B-20),  $\chi_p^{(\text{sphere})} = 0.237 + 0.030j$  while the cube susceptibility is  $\chi_p^{(\text{cube})} = 0.277 + 0.043j$ . Thus the

two susceptibilities remain close, even for complex  $\epsilon$ . As stated in Sec. IV-A, Fuchs has derived an analytical expression, Eq. (IV-21), which can be used to calculate  $\chi_p^{(\text{cube})}$  to sufficient accuracy for the types of calculations discussed in this paper.

#### Acknowledgements

The authors gratefully acknowledge the assistance of A. R. Mahoney in performing optical measurements and thermal aging tests and C. R. Hills for developing the film stripping technique.

## References

1. R. B. Pettit and R. R. Sowell, "Black Cr Solar Selective Coatings," Proc. of The Line-Focus Solar Thermal Energy Technology Development - A Seminar for Industry, Albuquerque, NM, Sept. 9-11, 1980, DOE and Sandia National Laboratories, 1980, pp. 389-397.\*
2. R. B. Pettit, R. R. Sowell and I. J. Hall, "Black Chrome Solar Selective Coatings Optimized for High Temperature Applications," (submitted to Solar Energy Materials).
3. R. B. Pettit, J. N. Sweet and R. R. Sowell, "Variation in the Microstructure of Electrodeposited Black Chrome Solar Coatings," 1982 MiCon Symposium, Jan. 18-19, 1982, Houston, TX (to be published in conference proceedings).
4. B. O. Seraphin, "Spectrally Selective Surfaces and Their Impact on Photothermal Energy Conversion," in Solar Energy Conversion, Topics in Applied Physics, Vol. 31, Ed. by B. O. Seraphin, Springer-Verlag, NY, 1979, pp. 5-55.
5. G. W. Treadwell, "Design Considerations for Parabolic-Cylindrical Solar Collectors," SAND 76-0082, July, 1976.\*
6. A. J. Sievers, "Spectral Selectivity of Composite Materials," ref. 4, pp. 57-114.
7. G. B. Smith and A. Ignatiev, Solar Energy Mat. 2, 461 (1980).
8. R. B. Pettit and C. J. Brinker, "Sol-Gel Protective Coatings for Black Chrome Solar Selective Films," Proceedings SPIE Conference on Optical Coatings for Energy Efficiency and Solar Applications, Jan. 28-29, 1981 (Los Angeles, CA), to be published.
9. H. Tabor, "Research on Optics of Selective Surfaces," Final Report AF61 (052)-279, Cambridge Research Laboratories, May 1959.
10. G. E. McDonald, Solar Energy 17, 119 (1975).
11. Harshaw ChromOnyx Black Chrome Plating Process, CRX-0270, Harshaw Chemical Co.
12. R. B. Pettit and R. R. Sowell, J. Vac. Sci. Technol 13, 596 (1976).

13. K. D. Masterson and B. O. Seraphin, "Inter-Laboratory Comparison of the Optical Characteristics of Selective Surfaces for Photo-Thermal Conversion of Solar Energy," Report NSF/RANN/SE/GI-36731X/TR/75/1, May 1975.
14. J. A. Leonard, "Dispersed Power Systems - Projects and Requirements," presented at DOE/DST Thermal Power Systems Workshop on Selective Absorber Coatings, Solar Energy Res. Inst., Golden, CO, 6-8 Dec., 1977.
15. R. R. Sowell and R. B. Pettit, "Thermal Aging of Electrodeposited Black Cr," SAND 78-0554, April, 1978.\* Also presented at the DOE/DST Thermal Power Systems Workshop on Selective Absorber Coatings (see Ref. 14).
16. R. B. Pettit and R. R. Sowell, "Recent Developments Regarding Electrodeposited Black Chrome Solar Coatings," Proc. Second Annual Conference on Absorber Surfaces for Solar Receivers, Solar Energy Res. Inst. Report, SERI/TP-49-182, Jan. 1979, pp. 33-40.\*
17. R. J. H. Lin and S. E. Heckler, "Black Chrome Coatings Development," Honeywell Systems and Research Center, Aug. 1979, Prepared for the DOE under contract, DE-AC04-78CS14287.
18. M. Valayapetre, O. T. Inal, L. E. Murr, A. E. Torma and A. Rosenthal, Solar Energy Mat. 2, 177 (1979).
19. L. Sivaswamy, S. Gowri and B. A. Shenoi, Metal Finishing 72, 48 (March 1974).
20. K. J. Cathro, Metal Finishing 76, 57 (Oct. 1978).
21. P. M. Driver, R. W. Jones, C. L. Riddiford and R. J. Simpson, Solar Energy 19, 301 (1977).
22. J. Spitz, T. Van Dahn and A. Aubert, Solar Energy Mat. 1, 189 (1979).
23. R. B. Pettit and R. R. Sowell, "Thermal Aging Characteristics of Electrodeposited Black Chrome Solar Coatings," in Proc. of the 1979 International Solar Energy Society Congress, May 28-June 1, 1979 (Atlanta, GA), pp. 1897-1901.

24. C. M. Lampert and J. Washburn, *Solar Energy Mat.* 1, 81 (1979).
25. I. T. Richie, S. K. Sharma, J. Villignaf and J. Spitz, *Solar Energy Mat.* 2, 167 (1980).
26. G. Zajac, G. B. Smith and A. Ignatiev, *J. Appl. Phys.* 51, 5544 (1980).
27. A. Ignatiev, P. O'Neill and G. Zajac, *Solar Energy Materials* 1, 69 (1979).
28. P. H. Holloway, K. Shanker, R. B. Pettit and R. R. Sowell, *Thin Solid Films* 72, 121 (1980).
29. D. M. Fell, L. L. Tongson, S. V. Krishnaswamy, R. Messier and I. S. T. Tsong, *J. Vac. Sci. Technol.* 17, 358 (1980).
30. G. Zajac and A. Ignatiev, *Solar Energy Materials* 2, 239 (1980).
31. D. J. Young and M. Cohen, *J. Electrochem. Soc.* 124, 769 (1977).
32. R. B. Pettit and B. L. Butler, "Mirror Materials and Selective Coatings," Sandia Laboratories Report SAND 77-0111 (Feb, 1977).\*
33. C. M. Lampert, *Thin Solid Films* 72, 73 (1980).
34. R. Landaur, "Electrical Conductivity in Inhomogeneous Media," in J. C. Garland, D. B. Tanner, Electrical Transport and Optical Properties of Inhomogeneous Media, AIP Conf. Proc. No. 40, Am. Inst. of Phys., NY, 1978, pp. 2-45.
35. R. Chang and W. F. Hall, "On the Correlation Between Optical Properties and Chemical/Metallurgical Constitution of Cr<sub>2</sub>O<sub>3</sub>/Cr Thin Films," in J. C. Garland and D. B. Tanner, Op. Cit. pp. 305-310.
36. A. Ignatiev, P. O'Neill, C. Doland and G. Zajac, *Appl. Phys. Lett.* 34, 42 (1979).
37. A. Ignatiev, P. O'Neill, G. Zajac and C. Doland, "The Surface Microstructure - Optical Properties Relationship in Solar Absorbers," in "Proc. Second Annual Conference on Absorber Surfaces for Solar Receivers," Jan. 24-25, 1979, SERI Report SERI/TP-49-182, pp. 9-16.\*
38. C. G. Granqvist and O. Hunderi, *J. Appl. Phys.* 50, 1058 (1979).
39. O. Hunderi and C. G. Granqvist, *Thin Solid Films* 57, 303 (1979).

40. B. Window, I. T. Richie and K. Cathro, *Thin Solid Films* 57, 309 (1979).
41. J. C. M. Garnett, *Philos. Trans. R. Soc. London* 203, 385 (1904); 205, 237 (1906).
42. D. A. G. Bruggeman, *Ann. Phys. (Leipzig)* 24, 636 (1935).
43. D. M. Wood and N. W. Ashcroft, *Philos. Mag.* 35, 269 (1977).
44. W. L. Bragg and A. B. Pippard, *Acta. Cryst.* 6, 865 (1953).
45. L. Genzel and T. P. Martin, *Surf. Sci.* 34, 33 (1973).
46. B. D. Cullity, *Introduction to Magnetic Materials*, Addison-Wesley, Mass, 1972, pp. 56-59.
47. R. W. Cohen, G. D. Cody, M. D. Coultts and B. Abeles, *Phys. Rev.* B8, 3689, (1973).
48. P. O'Neill and A. Ignatiev, *Phys. Rev.* B18, 6540 (1978).
49. G. B. Smith, *Appl. Phys. Lett.* 35, 668 (1979).
50. G. A. Niklasson, C. G. Granqvist and O. Hunderi, *Applied Optics* 20, 26 (1981).
51. R. C. McPhedran and D. R. McKenzie, *Proc. R. Soc.* A359, 45 (1978).
52. D. R. McKenzie, R. C. McPhedran and G. H. Derrick, *Proc. R. Soc.* A362, (1978).
53. R. Fuchs, *Phys. Rev.* B11, 1732 (1975).
54. J. Van Bladel, *Electromagnetic Fields*, McGraw-Hill, NY, 1964, pp. 73-77 (Eq. (3.74)).
55. E. R. G. Eckert and R. M. Drake, Jr., *Analysis of Heat and Mass Transfer*, McGraw-Hill Book Co., NY, 1972, pp. 128-137.
56. G. S. son Frey, *Z. Electrochem* 38, 260 (1932).
57. W. Lamb, D. M. Wood and N. W. Ashcroft, "Optical Properties of Small Particle Composites: Theories and Applications," in J. C. Garland, D. B. Tanner, Ref. 34, pp. 240-255.
58. P. B. Johnson and R. W. Christy, *Phys. Rev.* B9, 5056 (1974).
59. A. S. Barker, Jr. and J. A. Ditzenberger, *Phys. Rev.* B1, 4378 (1970).

60. A. S. Siddiqui and D. M. Treherne, *Infrared Physics* 17, 33 (1977).
61. D. R. Renneke and D. W. Lynch, *Phys. Rev.* 138, A530 (1965).
62. G. Lucovsky, R. J. Sladek and J. W. Allen, *Phys. Rev.* B16, 4716 (1977).
63. R. I. Frank and W. L. Moberg, *J. Vac. Sci. Tech.* 4, 133 (1967).
64. G. A. Niklasson and C. G. Granqvist, *Solar Energy Mat.* 5, 173 (1981).
65. G. B. Smith, *J. Phys. D*, 10, L39 (1977).
66. A. J. Sievers, *Ref. 4*, pp. 88-89.
67. H. C. Van de Hulst, *Light Scattering by Small Particles*, John Wiley, 1957, p. 66 (also published by Dover Inc., 1979).
68. O. S. Heavens, *Optical Properties of Thin Solid Films*, Dover Publications Inc., NY, 1965, pp. 63-79.
69. P. H. Holloway in *Scanning Electron Microscopy Vol. I*, SEM Inc., 1978, pp. 361-374.
70. P. H. Holloway, *Surf. Sci.* 66, 479 (1977).
71. M. A. Lind, R. B. Pettit and K. D. Masterson, *J. Solar Energy Eng., Trans. ASME* 102, 34 (1980).
72. Y. S. Touloukian and D. P. Dewitt, *Thermal Radiative Properties - Metallic Elements and Alloys*, Thermophysical Properties of Matter, TPRC Data Series, Vol. 7, IFI Plenum, NY, 1970, pp. 22a-26a.
73. D. E. Gray (Ed.), *American Inst. of Physics Handbook*, 3rd Ed. McGraw Hill, NY, 1972, pp. 6-124 to 6-155.
74. S. Berthier and J. Lafait, *J. De Physique (France)* 40, 1093 (1979).
75. G. W. Zajac, "The Relationship of Microstructure and Degradation Effects on the Optical Properties of the Selective Solar Absorber Black Chrome," Ph.D. Thesis, Univ. of Houston, Houston, TX, 1980.
76. H. Goldstein, *Classical Mechanics*, Addison-Wesley Inc., Reading, Mass., 1959, pp. 107-109.

77. M. A. Jaswon and G. T. Symm, Integral Equation Methods in Potential Theory and Elastostatics, Academic Press, NY, 1977, pp. 9-13.
78. D. A. Lindholm, IEEE Trans. Magn. MAG-16, 1409 (1980).
79. K. H. Haskall and W. H. Vandevender, "Brief Instructions for Using the Sandia Mathematical Subroutine Library," (Version 8.0), Sandia Laboratories Report SAND 79-2382, 1980, pp. 1-8 to 1-10.\*

\*Available from: National Technical Information Service (NTIS)

U. S. Dept. of Commerce

5285 Port Royal Road

Springfield, VA 22161

Distribution:

Dr. Barry Butler  
Materials Branch  
Solar Energy Research Institute  
1617 Cole Blvd.  
Golden, CO 80401

K. J. Cathro  
CSIRO  
Division of Mineral Chemistry  
Port Melbourne  
Vicivictoria, 3207  
AUSTRALIA

C. G. Granqvist  
Physics Dept.  
Chalmers Univ. of Technology  
S-412 96 Gotherburg  
SWEDEN

Lou Gianelos  
Harshaw Chemical Co.  
1945 East 97th Street  
Cleveland, OH 44106

Paul H. Holloway  
Dept. of Material Science & Eng.  
University of Florida  
Gainesville, FL 32611

O. Hunderi  
Dept. of Physical Metallurgy  
Norwegian Inst. of Technology  
7034 Trondheim NTH  
NORWAY

Jacques L. Hull  
Acurex Corp.  
485 Clyde Ave.  
MS 8-8800  
Mountain View, CA 94042

Alex Ignatiev  
Dept. of Physics  
University of Houston  
Houston, TX 77004

Osman T. Inal  
New Mexico Tech.  
Dept. of Metall. & Materials Eng.  
Socorro, NM 87801

Carl M. Lampert  
Lawrence Berkeley Lab  
University of California  
Berkeley, CA 94720

D. R. McKinzie  
School of Physics  
University of Sydney  
New South Wales 2006  
AUSTRALIA

Keith Masterson  
Solar Energy Research Institute  
1617 Cole Blvd.  
Golden, CO 80401

Dr. B. O. Seraphin  
Optical Sciences Center  
University of Arizona  
Tucson, AZ 85721

A. J. Sievers  
Physics Dept.  
Clark Hall  
Cornell University  
Ithaca, NY 14850

Marten Sikkens  
Dept. of Applied Physics  
University of Groningen  
Nijenborgh 18  
9747 AG Groningen  
THE NETHERLANDS

J. Spitz  
Laboratoire d'Etudes des Materiaux  
Centre d'Etudes Nucleaires de Grenoble  
85 X-38041 Grenoble-Cedex  
FRANCE

G. Zajac  
Department of Physics  
University of Houston  
Houston, TX 77004

2552 P. D. Thacher  
4720 D. G. Schueler  
4728 J. F. Banas  
4728 G. W. Treadwell  
5800 R. S. Claassen  
Attn: 5810 R. G. Kepler  
5830 M. J. Davis  
5840 N. J. Magnani  
5815 G. E. Pike  
5820 R. E. Whan  
Attn: 5821 N. E. Brown  
5822 K. H. Eckelmeyer  
5823 J. A. Borders  
5823 M. B. Chamberlain  
5824 J. N. Sweet (4)  
5824 R. B. Pettit (4)  
5824 W. D. Drotning  
5824 E. P. Roth  
5824 A. R. Mahoney  
5833 R. R. Sowell  
8214 M. A. Pound  
8310 D. M. Schuster  
3141 Tech Library (5)  
3151 W. L. Garner (3)  
for DOE/TIC  
DOE/TIC (25)  
(C. Dalin, 3154-3)